UCLA
UCLA Electronic Theses and Dissertations

Title
Plasma Structure and Behavior of Miniature Ring-Cusp Discharges

Permalink
https://escholarship.org/uc/item/26n6g056

Author
Mao, Hann-Shin

Publication Date
2013

Peer reviewed|Thesis/dissertation

eScholarship.org Powered by the California Digital Library
University of California

University of California

Los Angeles

Plasma Structure and Behavior of Miniature Ring-Cusp Discharges

A dissertation submitted in partial satisfaction

of the requirements for the degree

Doctor of Philosophy in Aerospace Engineering

by

Hann-Shin Mao

2013

© Copyright by
Hann-Shin Mao
2013

Abstract of the Dissertation

Plasma Structure and Behavior of Miniature Ring-Cusp Discharges

by

Hann-Shin Mao

Doctor of Philosophy in Aerospace Engineering

University of California, Los Angeles, 2013

Professor Richard E. Wirz, Chair

Miniature ring-cusp ion thrusters provide a unique blend of high efficiencies and millinewton level thrust for future spacecraft. These thrusters are attractive as a primary propulsion for small satellites that require a high ΔV, and as a secondary propulsion for larger spacecraft that require precision formation flying, disturbance rejection, or attitude control. To ensure desirable performance throughout the life of such missions, an advancement in the understanding of the plasma structure and behavior of miniature ring-cusp discharges is required.

A research model was fabricated to provide a simplified experimental test bed for the analysis of the plasma discharge chamber of a miniature ion thruster. The plasma source allowed for spatially resolved measurements with a Langmuir probe along a meridian plane. Probe measurements yielded plasma density, electron temperature, and plasma potential data. The magnetic field strength was varied along with the discharge current to determine the plasma behavior under various conditions. The structure of the plasma properties were found to be independent of the discharge power under the proper scaling. It was concluded that weaker magnetic fields can improve the overall performance for ion thruster operation.

To further analyze the experimental measurements, a framework was developed based on the magnetic field. A flux aligned coordinate system was developed to decouple the perpendicular and parallel plasma motion with respect to the magnetic field. This was done using the stream function and magnetic scalar potential. Magnetic formulae provided intuition on the field profiles dependence on magnet dimensions. The flux aligned coordinate system showed that the plasma was isopycnic along constant stream function values. This was used to develop an empirical relation suitable for estimating the spatial behavior and to determine the plasma volume and loss areas.

The plasma geometry estimates were applied to a control volume analysis on the plasma electrons. Balancing the plasma electron generation and loss yielded nominal values used in miniature ion thrusters. This result was ultimately used to develop a design tool for miniature discharges. This tool was used to perform a parametric evaluation on the magnet field configuration of the research mode. By understanding the plasma behavior, significant improvements over the baseline configuration were obtained with relatively minor changes, thus revealing the importance of plasma structure on the performance of miniature ring-cusp discharges.

The dissertation of Hann-Shin Mao is approved.

Troy A. Carter

Jeff D. Eldredge

Dan M. Goebel

Ann R. Karagozian

Richard E. Wirz, Committee Chair

University of California, Los Angeles
2013

To my mother and father, for the opportunity and the inspiration

Table of Contents

List of Figures

List of Tables

NOMENCLATURE

$\dot{m}_p$	Mass flow rate of propellant
$\dot{m}_d$	Mass flow rate
$\dot{v}_{\parallel}$	Parallel acceleration
η_m	Mass utilization efficiency
η_{trans}	Ion transparency
$\langle \sigma_* v_p \rangle$	Excitation reaction rate coefficient for primaries
$\langle \sigma_i v_p \rangle$	Ionization reaction rate coefficient for primaries
$\mathbf{\hat{e}_i}$	Generic basis
$\mathbf{B}$	Magnetic field
$\mathbf{E}$	Electric field
$\mathbf{F}_L$	Lorentz force
$\mathbf{T}$	Thrust
$\mathbf{v_e}$	Exhaust velocity
$\mathbf{v}$	Velocity
$\mathbf{v}_s$	Species velocity
$\mathrm{d}\mathbf{A}$	Differential area
μ	Magnetic moment
Φ	Scalar potential basis
ϕ	Plasma potential
Φ_m	Magnetic scalar potential
Π	Complete elliptical integral of the third kind
Ψ	Stream function values
τ	Spitzer slowing time for primary in background plasma
θ	Azimuthal basis
ε_B	Discharge loss
ε_{Bk}	Discharge loss with keeper power
$\widetilde{n}$	(Re)Normalized density
A_a	Anode loss area
$A_a(\Psi)$	Anode loss area based on the stream function technique
A_{cat}	Cathode area
A_{probe}	Probe area

A_{slot}	Access slot area
B	Magnetic flux density
B_r	Radial magnetic field component
B_z	Axial magnetic field component
B_{r*}	Residual induction
B_r^+	Radial magnetic field from inner radius
B_r^-	Radial magnetic field from outer radius
B_z^+	Axial magnetic field from inner radius
B_z^-	Axial magnetic field from outer radius
d	Block magnet half-depth
D^*	Depth scale factor
$f\left(\phi\right)$	Sheath modifier
F_B	Beam flatness parameter
g	Gravitational acceleration
g_r	Stream function gradient - radial
g_z	Stream function gradient - axial
h	Block magnet height
h_i	Scale factors
I_b	Beam current
I_d	Discharge current
I_e	Plasma electron generation
I_k	Keeper current
I_{*p}	Plasma electrons generated from primary in excitation
$I_{\tau p}$	Plasma electrons generated from thermalization
I_{in}	Neutral current in
I_{ip}	Plasma electrons generated from primary in ionization
I_i	Plasma electrons or ions generated from ionization
I_{sat}	Ion saturation current
I_{sp}	Specific impulse

K	Complete elliptical integral of the first kind
k	Boltzmann's constant
L	Chamber length
L_B	Length parameter
M	Magnetization
m_e	Electron mass
m_p	Propellant mass
M_{Xe}	Xenon mass
n	Plasma density
n_e	Plasma electron density
n_eV_e	Number of plasma electrons
n_i	Ion density
n_o	Neutral density
n_pV_p	Number of primary electrons
n_{eff}	Effective density
P	Power
p	Momentum
P_k	Keeper power
Pr_s	Permutation for block magnet ($s = [x, y, z^+, z^-]$)
Q	Volumetric flow rate
q_s	Species charge
R	Chamber radius
r	Radial coordinate
r_i	Coordinate component
r_{in}	Inner radius
r_{out}	Outer radius
T_e	Plasma electron temperature
T_o	Neutral temperature
v_a	Ion acoustic velocity
V_d	Discharge voltage
V_k	Keeper voltage
V_p	Plasma volume
w	Block magnet half-width
$w(\Psi)$	Plasma weighting function for vessel dimensions
W^*	Width scale factor
z	Axial coordinate

ACKNOWLEDGMENTS

I consider myself fortunate when I look back on the great faculty that I've met at UCLA. It is truly an honor to have some of the most influential figures in my academic career as my committee members. I'd like to thank Professor Troy Carter for introducing me to the larger scope of plasma physics and to Professor Jeff Eldredge for inspiring me to become passionate towards my craft. To Professor Ann Karagozian, I am deeply grateful for her mentorship and giving me my first research opportunity. To Dr. Dan Goebel, it was truly an honor getting to work with you. His selfless dedication to his students will always be appreciated. I give my most sincere thanks to my advisor Professor Richie Wirz for his friendship, encouragement, and endless patience. I am proud to be his first student, and am thankful for all of his teachings both in and out of the lab. Finally, I would like to thank the faculty of the Mechanical and Aerospace Engineering Department for their continued dedication in the lecture halls. As students, it is easy to take for granted the outstanding caliber of educators that surround us.

To my lovely wife Michelle, I am eternally grateful for her patience, friendship, and her ability to put a smile on my face at will. I'd also like to thank my parents, brother, and my new parents and sisters for their continued support and encouragement. I could not have asked for a better family.

Throughout my time at UCLA, I have had the immense pleasure of getting to know my brilliant peers. I would especially like to thank my fellow lab mates in the Wirz Research Group: Jun, Ben, Perry, Phil, Marlene, Lauren, Ryan, Emily, Sebastian, Monica, and Taylor. Thank you for keeping me positive through the years and for the intellectual stimulation. I can't wait to see all of your great accomplishments.

VITA

2006	Scholarship, Sponsored by Boeing.
2007	B.S., Aerospace Engineering, UCLA
2007	Outstanding B.S. Student in Aerospace Engineering Award
2008	Teaching Assistant, Preliminary Design of Aircraft, Rocket Propulsion System, Introduction to Astronautics, Department of Mechanical and Aerospace Engineering, UCLA
2009	NASA Space Grant - Jet Propulsion Laboratory (JPL), research advisory by Dr. Richard Wirz
2009	Graduate Student Researcher, Department of Mechanical and Aerospace Engineering, UCLA.
2009	M.S., Aerospace Engineering, UCLA
2009	Outstanding M.S. Student in Aerospace Engineering Award
2009	Fellowship, NASA Graduate Student Research Program - Jet Propulsion Laboratory (JPL), research advisory by Professor Richard Wirz, JPL advisory by Dr. Dan Goebel
2010	Teaching Associate, Introduction to Astronautics, Department of Mechanical and Aerospace Engineering, UCLA
2011	Advanced to Ph.D. Candidacy, May

PUBLICATIONS

H-S. Mao, R. Wirz, “Quasi-equilibrium electron density along a magnetic field line,” *Applied Physics Letters*, Volume 101, Issue 22, 2012.

H-S. Mao, D. Goebel, R. Wirz, “Plasma Structure of Miniature Ring-Cusp Ion Thruster Discharges,” *48th AIAA Joint Propulsion Conference*, AIAA 2012-4021, Atlanta, GA, 2012.

R. Wirz, L. Chu, M. Patino, H-S. Mao, S.J. Araki, “Well-Characterized Plasma Experiments for Validation of Computational Models,” *32nd International Electric Propulsion Conference*, IEPC 2011-122 Kurhaus, Wiesbaden, Germany, 2011.

H-S. Mao,R. Wirz, “Comparison of Charged Particle Tracking Methods for Non-Uniform Magnetic Fields,” *42nd AIAA Plasmadynamics and Lasers Conference*, AIAA 2011-3739, Honolulu, HI, 2011.

CHAPTER 1

Introduction

Miniature ion thrusters are an attractive and enabling technology for a variety of space missions. Conventionally sized ion thrusters, typically 25-30 cm in diameter are highly efficient. Miniaturization to the 3 cm scale requires careful consideration of the plasma structure and behavior of the ring-cusp discharge to maintain desirable performance. To motivate this work, this chapter briefly introduces electric propulsion an then provides a discussion of miniature ion thrusters and relevant applications. The chapter is concluded with an overview of the dissertation.

1.1 Electric Propulsion

Electric propulsion, or EP, is an attractive option for many space missions due to its ability to provide high specific impulse and low disturbance, precision thrust. Thrust is given by the product of the mass flow rate and the exhaust velocity of the propellant as seen in Equation (1.1). Most electric propulsion schemes achieve efficient thrust through high exit velocities, $\mathbf{v_e}$, and relatively low propellant mass flow rates, $\dot{m}_p$, which yields a higher momentum change per unit of propellant over chemical propulsion.

$$\mathbf{T} = \dot{m}_p \mathbf{v_e} \tag{1.1}$$

Unlike chemical propulsion systems which are limited by the energy density of the propellant, electric propulsion systems can create the kinetic energy of the propellant through external power sources such as solar arrays or nuclear reactors. High powered EP devices, such as ion thrusters, date back to the 1960's, however, they were not widely used until the past couple of decades due to the lack of technology in power storage and processing[4]. Among the many electric propulsion concepts, ion thrusters have distinguished themselves by achieving the highest efficiencies and specific impulses, I_{sp}, of all the mainstream EP devices (See Table 1.1). Specific impulse measures the change in momentum per unit of propellant weight as shown in Equation (1.2).

$$I_{sp} = \frac{T = \frac{dp}{dt}}{g\frac{dm_p}{dt}} \approx \frac{\Delta p}{g \Delta m_p} = \frac{|\mathbf{v_e}|}{g} \tag{1.2}$$

The high I_{sp} produced by ion thrusters make them ideal for long duration missions and deep space travel to the outer regions of the solar system. The high specific impulse, however, comes at the cost of lowered thrust. This can be shown by combining Equations (1.1) & (1.2) to form Equation (1.3). As specific impulse is increased, thrust must decrease for a given available power; therefore, ion thrusters are most attractive for long duration missions.

$$P = g\frac{TI_{sp}}{2} \tag{1.3}$$

1.2 Miniature Electron Bombardment Ion Thrusters

Ion thrusters bring a number of benefits to spacecraft over other propulsion systems. The use of the noble gas xenon as a propellant in modern ion thrusters

Table 1.1: Typical operating parameters for thrusters with flight heritage[1].

Thruster	Thrust (N)	Specific Impulse (s)	Input Power (kW)	Efficiency Range (%)	Propellant
Cold gas	0.05-200	50-75	–	–	Various
Chemical (monoprop)	0.05-0.5	150-250	–	–	N_2H_4 H_2O_2
Chemical (biprop)	5-5×10^6	300-450	–	–	Various
Resistojet	0.005-0.5	300	0.5-1	65-90	N_2H_4 monoprop
Arcjet	0.05-5	500-600	0.9-2.2	25-45	N_2H_4 monoprop
Ion thruster	< 0.5	2500-3600	0.4-4.3	40-80	Xenon
Hall thruster	< 3	1500-2000	1.5-4.5	35-60	Xenon
PPT	< 0.005	850-1200	< 0.2	7-30	Teflon

make them favorable alternatives to propulsion technologies with toxic propellants, such as hydrazine, which can be harmful to handle and degrade sensitive satellite equipment such as telescope lenses. The high propellant efficiencies and specific impulses reduce the wet mass of the spacecraft and extend the mission capabilities. Finally, ion thrusters provide smooth amplitude modulated thrust that can be precisely controlled by changing the electrostatic potential of the thruster bias. This unique blend of capabilities make miniature ion thrusters attractive to a wide range of missions. Miniaturization of ion thrusters to sizes below 5 cm brings these benefits to spacecraft requiring mN level thrust and a propulsion system with a smaller footprint. In 2001, Wirz demonstrated successful miniaturization of a noble gas DC ion thruster at the 3 cm scale[5]. The Miniature Xenon Ion thruster, or MiXI thruster, has demonstrated a thrust range from $0.03 - 1.54$ mN[6], and has a projected maximum thrust of 3 mN[7]. The compact size makes MiXI a versatile propulsion device for a variety of applications. A single thruster could be used for a smaller spacecraft, or several thrusters could be used for larger thruster applications or precision orbit and attitude control[6]. This unique blend of properties represent a mission enabling technology, a few of which are highlighted in the following sections. Ion thruster operation and challenges associated with down-scaling are covered in Chapter 2.

Several other miniature propulsion technologies are under development[8]. Among the top prospects are miniature microwave ion thrusters and field emission electric propulsion (FEEP). The miniature microwave ion thrusters have a higher energy cost per thrust producing ion, but remove the hollow cathode. FEEP thrusters use strong electromagnetic fields to emit ions directly from liquid propellant, typically indium or cesium. With an I_{sp} that can be in the tens of thousands of seconds, these thrusters are promising; however, the propellant distribution for an array of emitters is currently under development[8].

1.2.1 History of Miniature Electron Bombardment Ion Thrusters

In 1962, Reader performed experiments to determine the effects of scaling on electron bombardment ion thrusters[10]. Mercury propellant was used in an divergent axial magnetic field, similar to what is now known as a Kaufman thruster. Three sizes were tested: 5 cm, 10 cm, and 20 cm. The magnetic field strength was scaled such that the product of the field strength and the diameter were held constant at roughly 200 G · cm. The study showed a disproportionate drop in propellant utilization efficiency, η_{ud}[1], and a large increase in discharge loss, ε_B[2], the two main parameters used to quantify ion thruster performance are given in Equation (1.4) & (1.5). Reader ultimately concluded that operating at higher densities would improve the performance of smaller thrusters.

$$\eta_m \equiv \frac{I_B m_i}{e\dot{m}_d} \tag{1.4}$$

$$\varepsilon_B \equiv \frac{I_D V_D}{I_B} \tag{1.5}$$

Development continued with cesium thrusters in the late 1960's. Many, including Sohl et. al, achieved successful operation of 2.5 cm thrusters[11]. Considerable effort was made by Lewis Research Center in the early 1970's to develop and test a 5 cm mercury thruster[12, 13, 14]. Eventually, mercury and cesium fell out of popularity for ion thrusters since the fuel poses hazards to both technicians handling the substance as well as the satellites that were to use the thrusters[15]. Xenon is used as an alternative due to its mass and benign nature. Unfortunately,

---

[1] Propellant utilization efficiency given in Equation (1.4), is a measure of the percentage of neutral gas that is ionized and turned into thrust, or beam current,I_B.

[2] Discharge loss given by Equation (1.5),is interpreted as the power consumed in the discharge chamber, $I_D V_D$, to generate a single beam ion.

Table 1.2: First ionization energies of propellants.

Propellant	First Ionization Energy ($\frac{\text{eV}}{\text{ion}}$)
Mercury	10.44
Cesium	3.89
Argon	15.77
Xenon	12.13

xenon ionization energy is much higher than cesium, as seen in Table 1.2, making it more difficult to create a plasma in a small discharge chamber.

Within the past two decades, a resurgence in miniature ion thruster development has occurred. The rebirth occurred to fill a need for microspacecraft propulsion as well as low disturbance missions such as interferometery[16]. Research conducted by the Massachusetts Institute of Technology had numerically determined that sub-mm diameter discharges would be highly inefficient; therefore, experimental design began with "mesoscale" discharges on the cm scale[17]. Wirz successfully operated a 3 cm xenon ion thruster, MiXI, demonstrating efficiencies on the order of conventionally-sized thruster[5]. This was accomplished using a 3 ring-cusp configuration. Along with developing functional hardware, Wirz developed a computational model that showed that ionization was predominantly achieved by primary electrons and that 50% of the primary electron energy is likely lost to the wall[18]. In contrast, he found that the larger 30 cm NSTAR thruster loses almost no primary electrons to the wall. A combination of experimental and computational results showed that the miniature thruster required that the magnetic field needed to be sufficiently low to avoid discharge impedance shift instabilities, thus resulting in relatively high primary electron losses. Since higher fields are generally needed to improve the discharge efficiency, it was concluded that miniature ring-cusp ion thruster design was a balance between plasma confinement and discharge stability.

1.2.2 MiXI Application Examples

TPF-Emma

Due to MiXI's unique blend of capabilities, it was officially identified as the baseline propulsion system for the Terrestrial Planet Finder Interferometry and Emma variants (TPF-I/TPF-Emma) shown in Figure 1.1[19]. TPF-Emma is a precision formation flying mission designed to find extrasolar planets using interferometry. The spacecraft constellation utilizes four reflector spacecraft and a combiner spacecraft separated anywhere from $20 - 1200$ m, and required a spatial accuracy of ± 2.5 cm. To achieve the interferometry, the reflector constellation rotates about the combiner axis, and the rotation precision must be within 1 arcsec $= \left(\frac{1}{360}\right)^{\circ}$. To meet the propulsion requirements, each spacecraft would be outfitted with at least 20 MiXI thrusters for a total of 100 thrusters to provide 6 degree of freedom control and sufficient ΔV for formation rotation and re-orientation throughout the 10 year life of the mission.

Such a mission is an excellent example of the mission enabling capabilities of a miniature ion thruster. Beyond providing the critical characteristics of ion thruster (benign propellant, precision control, high I_{sp}, etc.), the small footprint and low thrust levels of MiXI were critical to the mission's feasibility.

CubeSat Propulsion

Recently, the possibilities of using a miniature ion thruster as a the primary propulsion system for CubeSats has been explored. CubeSats serve a wide range

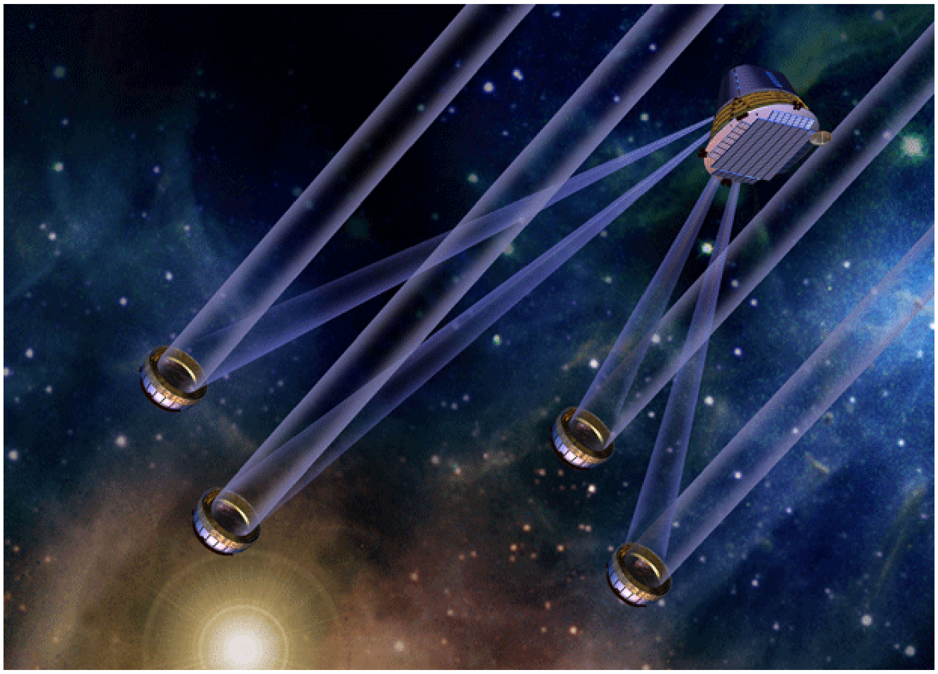

Figure 1.1: Terrestrial Planet Finder (TPF), Emma variant, consists of five spacecraft with distances up to 1.2 km between spacecraft and an accuracy requirement down to 2.5 cm. The spacecraft constellation will utilize 100 MiXI thrusters. Courtesy of NASA/JPL-Caltech.

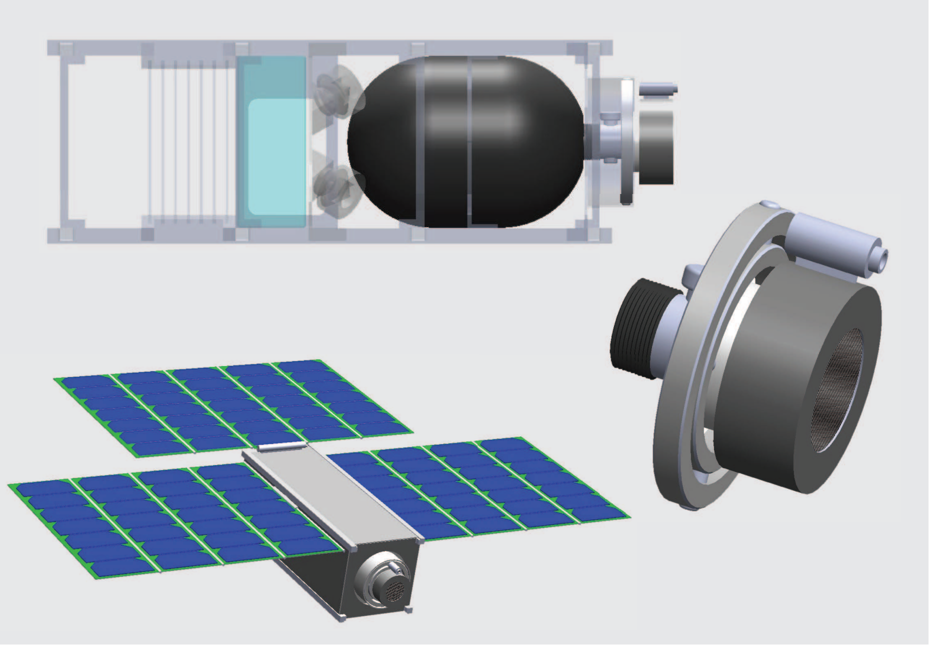

Figure 1.2: Design for a MiXI powered 3U CubeSat. Courtesy of Ryan Conversano.

of purposes from university experiments to qualification test beds for commercial products[8], but have yet to be demonstrated with a propulsion systems. Outfitting a CubeSat with a propulsion system would greatly expand the scope of missions that it could perform. A miniature ion thruster would be ideal for a CubeSat because of its efficient use of propellant compared to other micro-propulsion concepts.

A study by Conversano and Wirz recently investigated the feasibility of a Lunar mission for a CubeSat using the MiXI thruster[20]. The spacecraft, shown in Figure 1.2 would be made of a 3-Unit, or “3U”, CubeSat and be capable of achieving a ΔV of over 7000 $\frac{\mathrm{m}}{\mathrm{s}}$. The spacecraft would utilize a spiral trajectory to transfer to the lunar orbit. Additionally, such a high ΔV would be capable of a minimum of 50° of inclination change in a 600 km low Earth orbit. The power and mass requirements for such a mission prove to very challenging, but the increase in capability motivate the need for thruster development.

1.2.2.1 Other Mission Types

MiXI could prove to be beneficial for other applications such as disturbance rejection and station keeping. In high-altitude applications, for example, a single MiXI thruster could counteract the solar radiation pressure on a 666 m^2 solar array. It would only take five MiXI thrusters to counteract the radiation pressure on solar panels the size of on the International Space Station. This could be useful in future high-precision missions.

For low-altitude environmental and atmospheric missions, MiXI can also provide atmospheric drag compensation. At an altitude of 500 km, MiXI's thrust could counteract the atmospheric drag caused by a satellite with a cross section of 11 m^2. This is critical for missions that desire repeat orbit capabilities. In both high and low altitude applications, use of MiXI would benefit missions with a non-contaminating propellant; continuous, non-disturbing thrust; high efficiencies; and high I_{sp} (which translates to a longer mission duration or reduced launch vehicle cost).

1.3 Dissertation Overview

The current study simplifies the domain of the miniature ion thruster by isolating the discharge chamber. The accelerator grids and the asymmetry of the magnetic field configuration are replaced with symmetric features. By generalizing the chamber geometry and magnetic field, the results provide knowledge of similarly sized devices. Additionally, because of the smaller dimensions of the discharge, it becomes feasible to make spatially resolved measurements on the entire domain including the regions directly adjacent to the magnetic cusp.

While a 3 cm xenon ion thruster has already been demonstrated in a laboratory environment, the internal discharge operation at that scale is still relatively unknown. Improvements to the discharge operation would provide substantial benefits to the overall mission applicability of a thruster of this size. Experimental measurements made from the beam profile allowed estimates of plasma properties immediately upstream of the extraction plane[21]; however, the plasma discharge parameters have not been directly measured. Plasma property measurements in larger thruster have been made by Herman and Sengupta et al.[22, 23]. While these provided informative, spatially resolved data, they typically neglected the cusp region due to access restrictions in the ion thruster and resolved measurements were limited to a particular sub-domain or dimension.

To explore the internal structure of MiXI, Wirz developed a 2-D hybrid particle-in-cell (PIC) model, DC-ION[24]. Plasma property measurements from a miniature discharge provide an excellent resource to validate DC-ION. While DC-ION can be used to explore additional physics and detailed design, its complexity precludes it from being a first-order design tool. Thus the ultimate goal of this research effort is to analyze the internal measurements and develop a rapid design procedure for miniature discharges.

Chapter 2 provides background on electron bombardment plasmas and their operation principles. This chapter introduces some of the physical processes that make the miniaturization of DC discharges difficult including the increase in surface area to volume ratio and the discharge instability. The experimental apparatus is described in Chapter 3. The design features of the device are highlighted along with the support facilities. The current effort focuses on four data sets that explore combinations of discharge configurations and operating conditions. The two magnetic configurations explore the effects of field strength on discharge stability. Plasma measurements are presented for plasma density, electron temperature, and plasma potential.

Chapter 4 develops a framework by which to analyze magnetic fields. Here the stream function and scalar potential fields are calculated for the axisymmetric configurations described in Chapter 3. These fields create an orthogonal coordinate system that can be used for theoretical analysis in future work. Chapter 5 uses the stream function construct to analyze the plasma measurements. A transfer function is developed for the approximate density throughout the chamber for a given stream function field. This is used to calculate adjusted anode loss areas and plasma volumes for the highly non-uniform miniature discharges.

A control volume analysis is implemented in Chapter 6 using the modified plasma volumes and loss areas in the previous chapter. This analysis is implemented on the test discharge chamber from Chapter 3 to examine the design space for the magnetic field configuration. The chapter concludes with a recapitulation of the design procedure. The final chapter summarizes the major contributions and findings of the dissertation along with suggestions for future work.

CHAPTER 2

Magnetically Confined Cusp Discharges

Miniature ion thrusters fall into a unique regime where efficient operation is not easily obtained. The surface area to volume ratio of the thruster increases as thruster size decreases. This creates a relatively large plasma area at the thruster walls and a relatively small plasma volume where generation can occur. It is traditionally thought that stronger magnets are necessary to mitigate this effect; however, in cases where the magnetic field is too strong, the plasma will develop a potential structure that is vulnerable to discharge instability.

2.1 Basic Ion Thruster Discharge Chamber Operation

An illustration of a MiXI like ion thruster is shown in Figure 2.1. There are four main components to all ring-cusp ion thrusters: a high energy electron source, the discharge chamber with permanent ring magnets, the extraction apparatus, and a neutralizing electron source (not shown). The electron source is a thermionic emitter. Typically this is provided by a hollow cathode with a barium oxide or lanthanum hexaboride insert, but low TRL research will often use a simple filament cathode for preliminary development. The first iterations of MiXI used a tungsten filament cathode, but has since developed and used miniature hollow cathodes. The discharge chamber usually consists of an axisymmetric geometry along with a series of ring magnets alternating in polarity. The chamber walls, commonly referred to as the anode, are biased positively with respect to the filament. Due to thermal expansion of the chamber, the ring magnets are composed of several block magnets arranged in a ring and held against the anode. The extraction apparatus consists of two biased grids which give the ions their kinetic energy. The bias also acts to keep plasma electrons and neutrals contained within the discharge volume. Finally, the neutralizer cathode emits electrons with the thrust ions to maintain a neutrally charged spacecraft. The bias on the extraction apparatus also prevents neutralizing electrons from entering the discharge chamber.

The focus of this effort is limited to the first two components with a focus on the discharge chamber responsible for generating plasma. The technique used for producing plasma is known as a DC discharge due to the electrostatic fields. The propellant gas is initially fed into the discharge chamber either directly or or through the hollow cathode. High energy electrons from the electron source travel through the chamber to the anode potential surface biased at $\sim 20 - 25$ V with respect to the cathode. The magnetic field extends the residence time of the ionizing primary electrons emitted from the cathode. The primary electrons from the cathode follow a helical path along the magnetic field lines due to the Lorentz force, $\mathbf{F}_L$ given by:

$$\mathbf{F}_L = q_s\mathbf{E} + \mathbf{v}_s \times \mathbf{B}. \tag{2.1}$$

Here q_s is the species charge, $\mathbf{E}$ is the electric field, $\mathbf{v}_s$ is the species velocity, and $\mathbf{B}$ is the magnetic field. Primary electrons that encounter a magnetic cusp can be reflected through the magnetic mirroring effect provided that its trajectory is sufficiently orthogonal to the field line[25]. While magnetic fields are used to repel electrons at anode surfaces, cathode surface have a sufficient negative bias

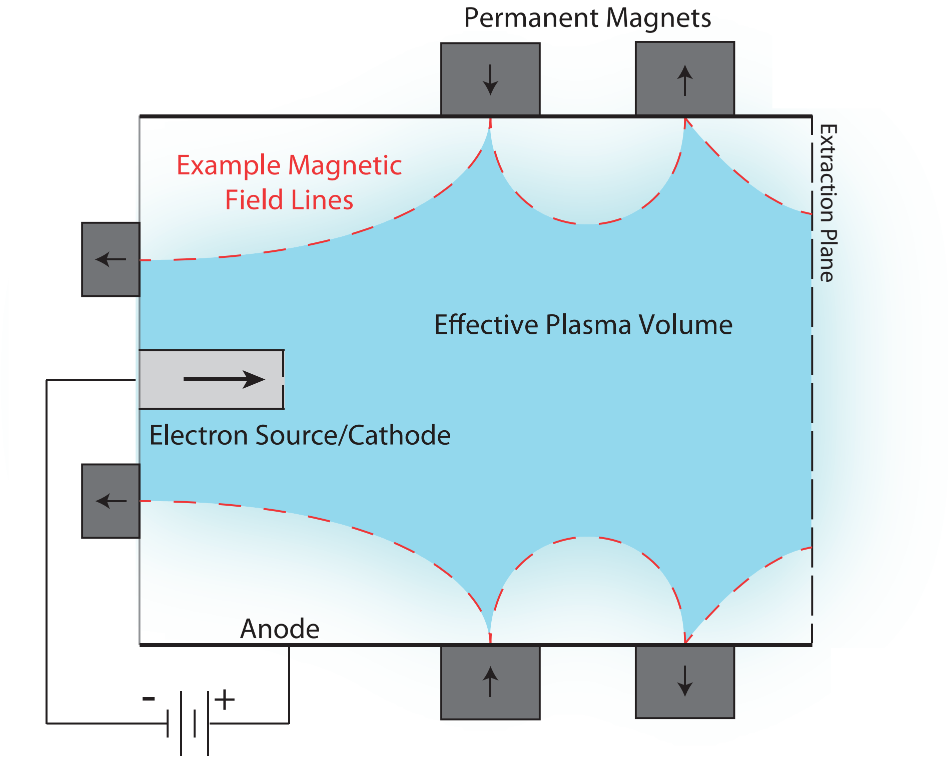

Figure 2.1: Axisymmetric cross-section of an electron bombardment ion thruster with a ring-cusp magnetic field.

that electrons are electrostatically reflected back into the bulk of the chamber. The primary electron's residence time is terminated when:

1. An ionization collision happens with a neutral. The primary electron's kinetic energy ionizes the heavy species generating an election/ion pair. The now lower energy electron is rapidly thermalized with the plasma electron population.
2. An excitation collision happens with a neutral. The primary electron's kinetic energy collides with the heavy species promoting the electrons in the atom to a higher energy state. The now lower energy primary is rapidly thermalized with the plasma electron population.
3. The primary contacts an anode boundary of the discharge chamber
4. The primary electrons accumulates several small inelastic collisions and thermalizes with the background plasma electrons.

Primaries that undergo successful ionization collisions will result in a single ion and two plasma electrons (one from the neutral atom and one from the resulting low energy primary). The bulk plasma will equilibrate such that the plasma density remains quasi-neutral ($n \equiv (n_p + n_e \approx n_i)$).

2.1.1 Ion Thruster Miniaturization

Generation of plasma, I_i, is a volumetric effect as can be seen in Equation (2.2). Here n_o is the neutral density, n_e & n_p are the plasma and primary electron densities, V_e & V_p are the associated volumes for the species, and the bracketed terms are the reaction rate coefficients. Note the use of I to indicate a generation rate and not a current.

$$I_i = n_o \left[(n_p V_p) \langle \sigma_i v_p \rangle + (n_e V_e) \langle \sigma_i v_e \rangle \right] \tag{2.2}$$

Loss of plasma occurs at the boundaries of the discharge chamber. The goal is to maximize the ions delivered to the extraction plane while balancing losses to anode surfaces in an effort to maintain the discharge plasma potential. It is beneficial to confine the electron population to increase ionization and ultimately the plasma density[26]. The inherent difficulty with miniaturization lies in the increased surface area to volume ratio, which is equivalent to saying that there is more plasma loss and less plasma generation. In order to mitigate this, strong magnets are used that reduce the anode loss area. If the magnets are too strong, this can reduce the plasma potential and lead to discharge stability issues discussed in Section 2.3.

2.2 Cusped Plasma Sources

Multipole confinement devices were first used in the 1970's by Limpaecher and MacKenzie[26]. The original intent was to develop a containment scheme that would be suitable for fusion. These multipole devices were extremely stable, but their efficiencies for fusion conditions was not comparable to other fusion confinement techniques. Further research for other devices was carried out on magnetic cusp devices due to their inherent stability and accessibility. Among the contributors were Leung and Herskowitz[3] as well as Bosch and Merlino[27]. Both groups determined that the leak width for the plasma species to the magnetic cusp were proportional to the hybrid gyroradius, r_h, given in Equation (2.4). The gyroradius for a particular species is given in Equation (2.3) and describes the radius of the orbit executed by a charge particle around a magnetic field line.

Here m_s, q_s, & v_s are the species mass, charge, and velocity perpendicular to the magnetic field, B, respectively. The hybrid gyrodiameter is simply the geometric mean of the ion gyroradius and the electron gyroradius. This length scale is motivated by electrostatic attraction as the two species enter the cusp.

$$r_s = \frac{m_s v_s}{q_s B} \tag{2.3}$$

$$r_h = \sqrt{r_e r_i} \tag{2.4}$$

While the hybrid loss width length scales may still apply in miniature ion thrusters, the sensitivity of these small discharges requires a highly resolved picture of the loss regions. Much of the previous work investigates cusp loss through vacuum gaps. The spindle cusp and the picket fence, studied by Bosch and Hershkowitz respectively, considered the entrance to the cusp to be in an arbitrary location since these experiments did not lead to conducting surfaces. Unlike in these devices, the strongest magnetic field in ion thrusters occurs at the cusp due to the use of permanent magnets. Efforts by Wirz et al. are focused on determining a more detailed loss structure for permanent magnets[28].

The hybrid width provides a useful parameter to determine the reduction of the plasma loss due to the magnetic field. This has been successfully used in control volume analysis of cusped devices to predict performance in larger devices[1, 29, 24, 18]. However, in miniature discharges, a strong magnetic field can lead to a significant contraction in the plasma volume.

MacKenzie buckets are now used to create laboratory plasmas with a large relatively unmagnetized region[2, 30, 31]. Although, the magnetic field is used to increase the plasma density, the bulk of the volume is largely unmagnetized due to the size of the vessel. The large field-free region allows researchers to ignore the complicated magnetic boundary. This configuration has a close relationship to larger ion thruster; however, with MiXI the length scales are such that the chamber is almost entirely made up of the magnetic boundary.

2.3 Plasma Potential Structure

Before MiXI's demonstration, it was commonly thought that thrusters ≤ 5 cm required magnet strengths that did not exist[17]. Wirz's research identified that extremely strong magnets decreased the loss area possibly creating a discharge instability[21]. Therefore, the lower bound for magnetic fields is set by acceptable performance while the upper bound is thought to be marked by the onset of instability.

Plasmas typically found in cusp-confined devices have plasma electron temperatures much greater than that of the ions, $T_e \gg T_i$. Therefore, in the absence of a potential gradient, the electrons are more frequently lost to the wall. This tendency creates a charge imbalance resulting in a potential structure that acts to equilibrate the loss of the two charge carriers. In a traditional ion attracting sheath, the plasma potential acts to repel electrons while attracting ions. In order for this to occur, the ions must enter the sheath at a velocity no smaller than the ion acoustic velocity given by Equation (2.5), where M_{Xe} is the xenon ion mass.

$$v_a = \sqrt{\frac{kT_e}{M_{Xe}}} \tag{2.5}$$

This is known as the Bohm criterion and is commonly used for an ion attracting sheath[25]. A typical potential structure for this scenario is given in the upper chart of Figure 2.2. Here the presheath is necessary to accelerate the ion population to the ion acoustic velocity at the sheath entrance.

There are several cases where a negative, or ion repelling sheath would occur. This scenario is possible when the charge carriers consists of a mix of positive and negative ions with the negative species being the heavier of the two[32]. This could also occur in the case of a significantly reduced anode loss area which could very likely occur in a miniature ion thrusters. The magnetic field found in ion thrusters reduces the loss area of the plasma electrons while the unmagnetized ions could flow freely to the wall. If the loss width is sufficiently small, a potential structure could develop that inhibits the ions and attracts the electrons. The potential structure for this scenario is illustrated in the bottom chart of Figure 2.2.

2.3.1 Discharge Instability

A discharge instability can develop in the case of a negative plasma potential. The anode voltage must be made up through the plasma. Unlike the positive potential case, the anode voltage is not guaranteed to occur through the cathode sheath. For a DC discharge to provide an appreciable plasma density, it is required that the plasma potential lies above the ionization energy. If instead the majority of the anode voltage is found in the anode sheath the plasma would extinguish or fall to an extremely low density value. The case marked “Unsustainable” is therefore not a desired scenario for a DC discharge.

2.3.2 Sheath Modifier

The flux of plasma electrons through a sheath can be derived from integrating over the Maxwellian electron population. This results in a piecewise continuous function of the plasma potential. The random electron flux to a surface, Equation (2.6), is modified due to the plasma sheath as seen in Equation (2.7). The sheath modifier, $f(\phi)$, is given for positive and negative potentials by Equa-

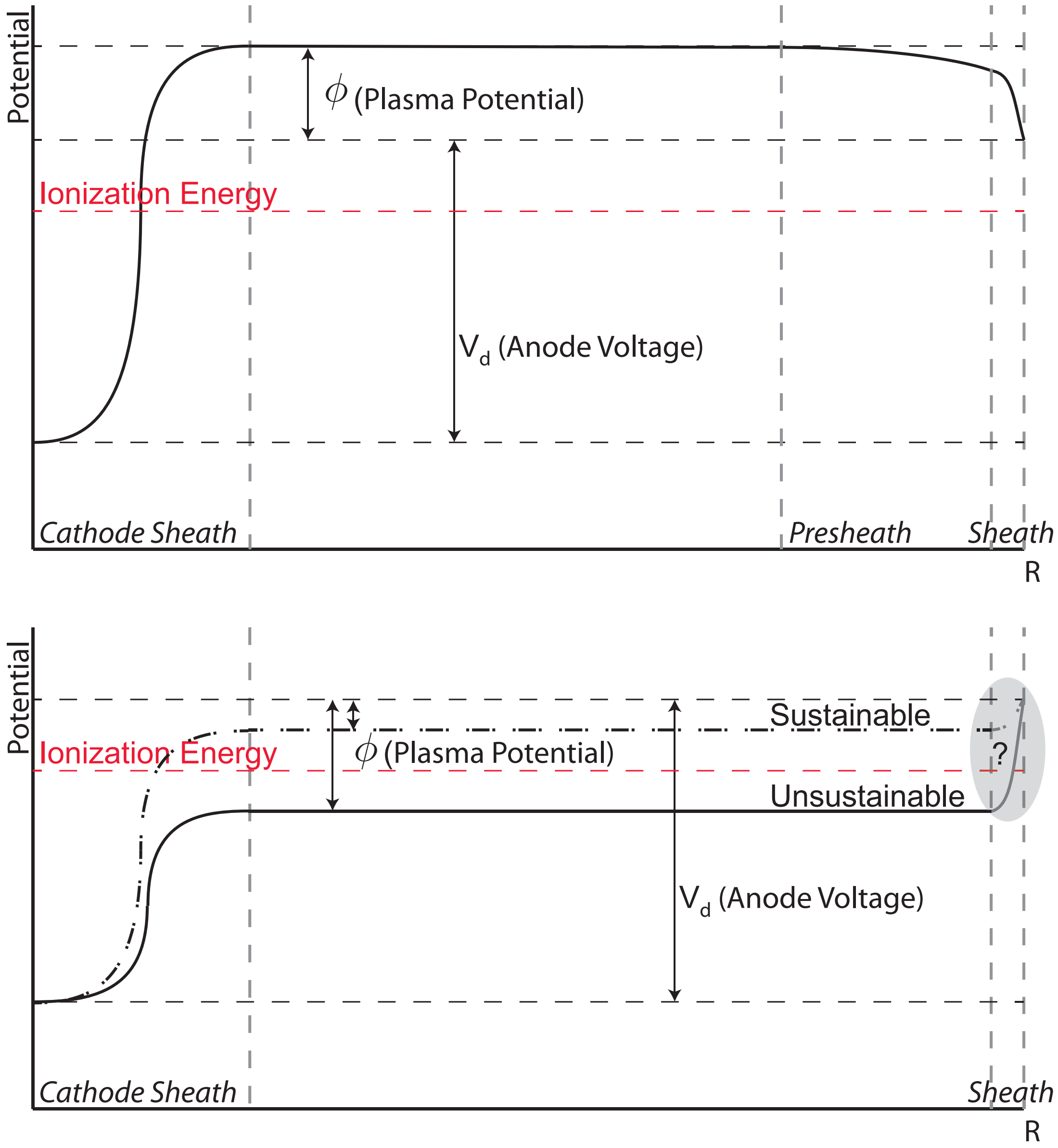

Figure 2.2: The top figure shows a typical sheath structure from the cathode to the anode[1]. This represents a positive plasma potential with respect to the anode voltage. The bottom figure shows a negative plasma potential which can develop in the case of readily lost positive particles. The sheath structure in a negative plasma is an area of recent discussion[2].

tion (2.8) and is shown in Figure 2.3[1, 33, 29]. The inverse notation is used here to be consistent with the way it is utilized in Chapter 6. The optimal value for an efficient ion source has been estimated to be at a zero plasma potential with respect to the anode[29]. A plasma potential slightly below the anode would confine the low energy ions, and allow for a high primary energy through the cathode sheath. Plasma species loss through a positive sheath takes energy out of the plasma on the order of the plasma potential. An even plasma potential eliminates this inefficiency.

$$\Gamma = \frac{1}{4} n_e \sqrt{\frac{8kT_e}{\pi m_e}} \tag{2.6}$$

$$I_a = \left[\frac{1}{4} n_e \sqrt{\frac{8kT_e}{\pi m_e}} A_a \right] f^{-1}\left(\phi\right) \tag{2.7}$$

$$f^{-1}\left(\phi\right) = \begin{cases} exp\left(\frac{-e\phi}{kT_e}\right), & \text{if } \phi > 0 \\ \frac{exp\left(\frac{e\phi}{kT_e}\right)}{1-erf\left(\frac{-e\phi}{kT_e}\right)^{\frac{1}{2}}}, & \text{if } \phi < 0 \end{cases} \tag{2.8}$$

2.3.3 Negative Plasma Sheath

The negative plasma sheath, seen in Figure 2.2 as a grayed out region, is not very well understood[2]. Previously, this region has been handled as a cathode sheath superimposed on a background plasma[33]; however, measurements by Oksuz and Hershkowitz show a double layer[31]. This double layer acts to reduce the plasma population flux derived by Medicus. Investigation of this feature is beyond the scope of this study, but must be considered for future studies of miniature discharges.

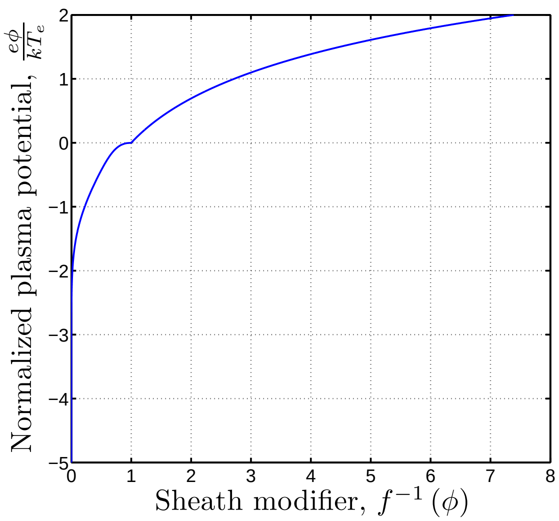

Figure 2.3: Sheath modifier function, $f(\phi)$, and its relation to the plasma potential.

CHAPTER 3

Experimental Investigation of a Miniature Discharge

Previous miniature ion thruster studies have demonstrated impressive performance using ring-cusp discharges[21]. These studies suggest that the field must be sufficiently strong to increase electron confinement times for ionization, but weak enough to allow electrons to escape and maintain the plasma potential necessary for ionization. To investigate this phenomena, this effort employs an experiment that allows detailed measurements of the internal structure and characteristics of a miniature ring-cusp discharge. These measurements provide spatially resolved values for plasma density, electron temperature, and plasma potential along a meridian plane. The magnetic field configuration is arranged as a quasi-periodic domain in order to generalize the findings to all multi-pole discharges. The results show that the magnetic field strength drives the plasma structure, and the dependence on discharge power can be removed with proper scaling of the plasma parameters. The stronger magnetic field results in a higher peak plasma density, but relatively poor discharge volume utilization. Additionally, the potential measurements indicate the likely onset of discharge instability. In contrast, the weaker magnetic field, or baseline configuration, better utilizes the volume of the chamber. This leads to a higher and more uniform density near the downstream extraction plane, implying a superior discharge for an ion source.

3.1 Experimental Approach

The miniature ring-cusp discharge experiment approximates the major features of a miniature ion thruster discharge. To make accurate measurements, there also must be access to the internal region of the discharge chamber for plasma diagnostics. As a result, a new device was designed with three equally spaced ring-cusps and an access slot for a Langmuir probe. This allows the examination of the important plasma properties of miniature discharges in a controlled environment.

3.1.1 Operating Principle and Design Features

The primary design objective for the experimental apparatus is to isolate the plasma discharge chamber of the miniature ion thruster. This is shown in Figure 3.1. Because the device does not need to produce thrust, the grids can be replaced with a cathode potential surface and run at a relatively low voltage known as discharge mode. Brophy's model for predicting discharge performance without beam extraction can be applied to approximate performance values[34]. This model has been successfully used to predict thruster performance in a variety of efforts[35, 36]. The cathode used is a neutralizer hollow cathode typically used for $\sim$ 30 cm ion thrusters. The cathode assembly is shown in Figure 3.2. The low flow rates used in neutralizer cathodes make it an appropriate electron source for examining miniature discharges. By running a keeper current, the hollow cathode is able to sustain a small plasma near the cathode orifice without running the discharge. This effectively removes uncertainty in the primary electron source. Typically, the hollow cathode placement should coincide with a diverging magnetic field to maximize the current to the discharge chamber[36]; however, in this study no hollow cathode magnet was used to maintain the symmetric domain. Additionally, the cathode was placed flush with the base in order

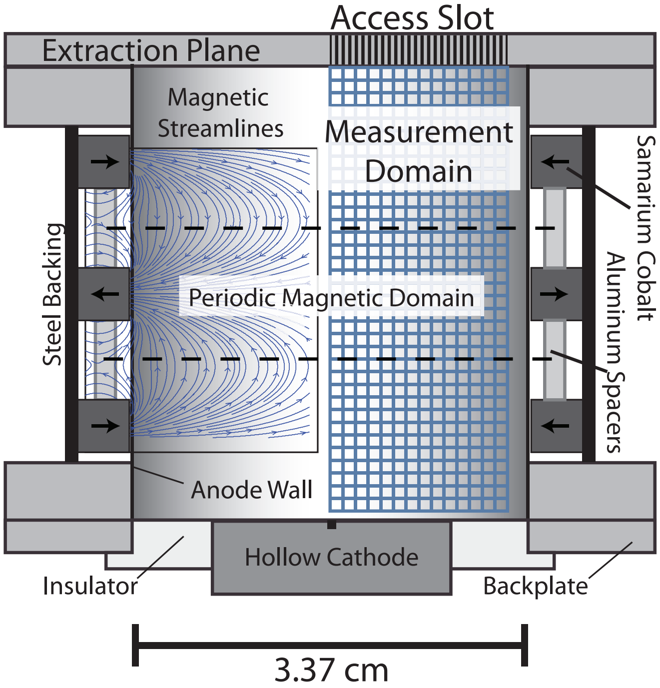

Figure 3.1: Schematic of the miniature ring-cusp discharge experiment.

to maximize the measurement domain. An early version of the experiment used a tungsten filament cathode along the centerline in an effort to maintain the axial asymmetry; however, the cathode preferentially emitted on one end due to the voltage drop across the filament. Ultimately, the filament was abandoned because it heated the device past the maximum operating temperature of the magnets. Additionally, removal of the filament allowed for a larger measurement domain.

The resulting device utilizes a cylindrical domain to hold the plasma. The discharge chamber is then surrounded with three identical rings of magnets equally spaced along the axis of the cylinder with machined spacers. For the baseline magnetic field configuration, each individual ring is made up of nineteen block magnets that outline the circumference of the exterior anode wall. The current effort is focused on determining the effects of magnetic field strength on the plasma properties. To increase the field strength for the strong magnetic field

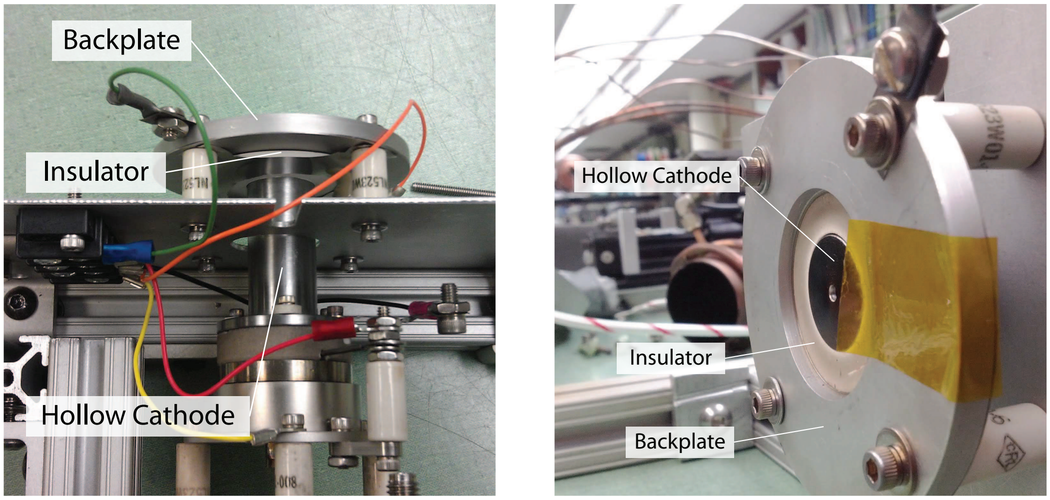

Figure 3.2: Hollow cathode installed in the miniature plasma testbed.

configuration, each block magnet in a given ring is doubled by stacking an additional magnet on the outside. This acts to bolster the magnetic field strength at the walls while leaving the far-field region relatively untouched as is discussed in Section 4.4.3. These two configuration are summarized in Table 3.1. The height dimension is parallel with magnetization vector while the depth dimension is aligned with the axial direction of the discharge domain. The individual magnets used in both cases are identical. The resulting two-dimensional magnetic fields are discussed in Section 3.2. The doubly-stacked configuration, or "strong" field case, is shown in Figure 3.3. The singly-stacked configuration is referred to as the "baseline" configuration.

The schematic shown in Figure 3.1 highlights the physical features of the device. The permanent magnet assembly is easily accessible and allows for relatively simple modification. The ring magnets are equally spaced with 6.35 mm aluminum (non-ferrous) spacer rings. This generalized configuration closely approximates a periodic magnetic domain; therefore, the results of this effort can be readily applied to miniature cusped discharges and is not confined to a specific

Table 3.1: Permanent magnet specifications.

Magnet ID	Material	Residual Induction (G), B_{r*}	Height (mm)	Width (mm)	Depth (mm)
Baseline (x1)	Sm_2Co_{17}	10,500	2.032	5.08	5.08
Strong (x2)	Sm_2Co_{17}	10,500	2 x 2.032	5.08	5.08

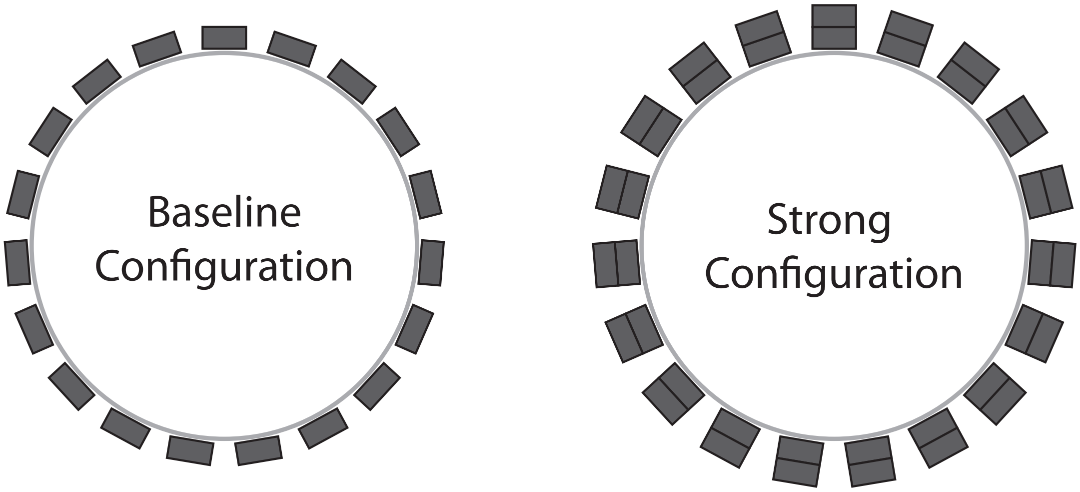

Figure 3.3: Schematic of magnetic field configurations.

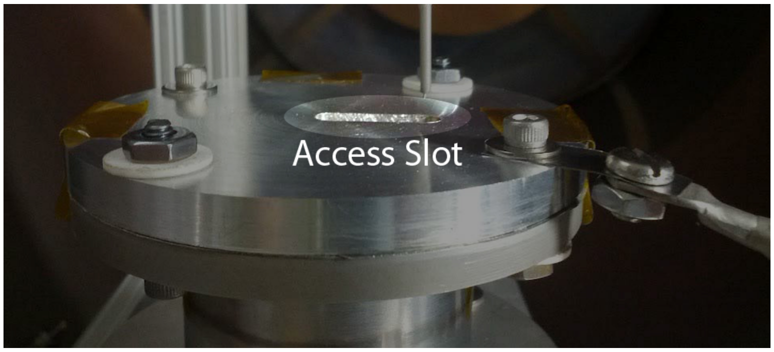

Figure 3.4: Slot cut into cathode surface for Langmuir probe access.

configuration. The "Access Slot" referenced in Figure 3.1 allows diagnostics into the plasma domain. The physical opening can be seen in Figure 3.4. The slot is 4.76 mm wide and spans the radius of the discharge domain which makes the area of the opening 0.86 cm^2. As a control, the discharge is fed a closed loop controlled 0.5 sccm of xenon in every test case. With the flow rate and orifice area, the neutral density is approximately 4×10^{19} m^{-3} or 1.8 mTorr. These values are based on neutral temperatures of $\sim$ 500 K from thermocouple measurements on the device. The measurement domain samples the meridian plane of the cylindrical domain. In this particular study, the magnet depth is much smaller than the radius of curvature. Because of this, the applied field is assumed axisymmetric, allowing the measurements to yield a complete description of the discharge chamber. The complete device assembled out of vacuum can be seen in Figure 3.5.

3.1.2 Support Facilities

The miniature ring-cusp discharge experiment was operated in a vacuum chamber at NASA's Jet Propulsion Laboratory seen in Figure 3.6. The chamber is outfitted with two 10-inch cryogenic pumps capable of providing a base pressure of 10^{-8} Torr. The pressure during operation is steady for a given test case and is typically around 8×10^{-6} Torr.

The experimental apparatus is mounted next to a two-dimensional, vacuum-prepped, translation stage assembly. The stages are positioned to move the probe on a rectilinear grid aligned with the plasma domain's radial and axial directions as shown in Figure 3.1. An attached armature carries a cylindrical Langmuir probe with a length of 1 mm and a half mm diameter, shown in Figure 3.7, to map out spatially resolved contours of the plasma properties. The Debye length

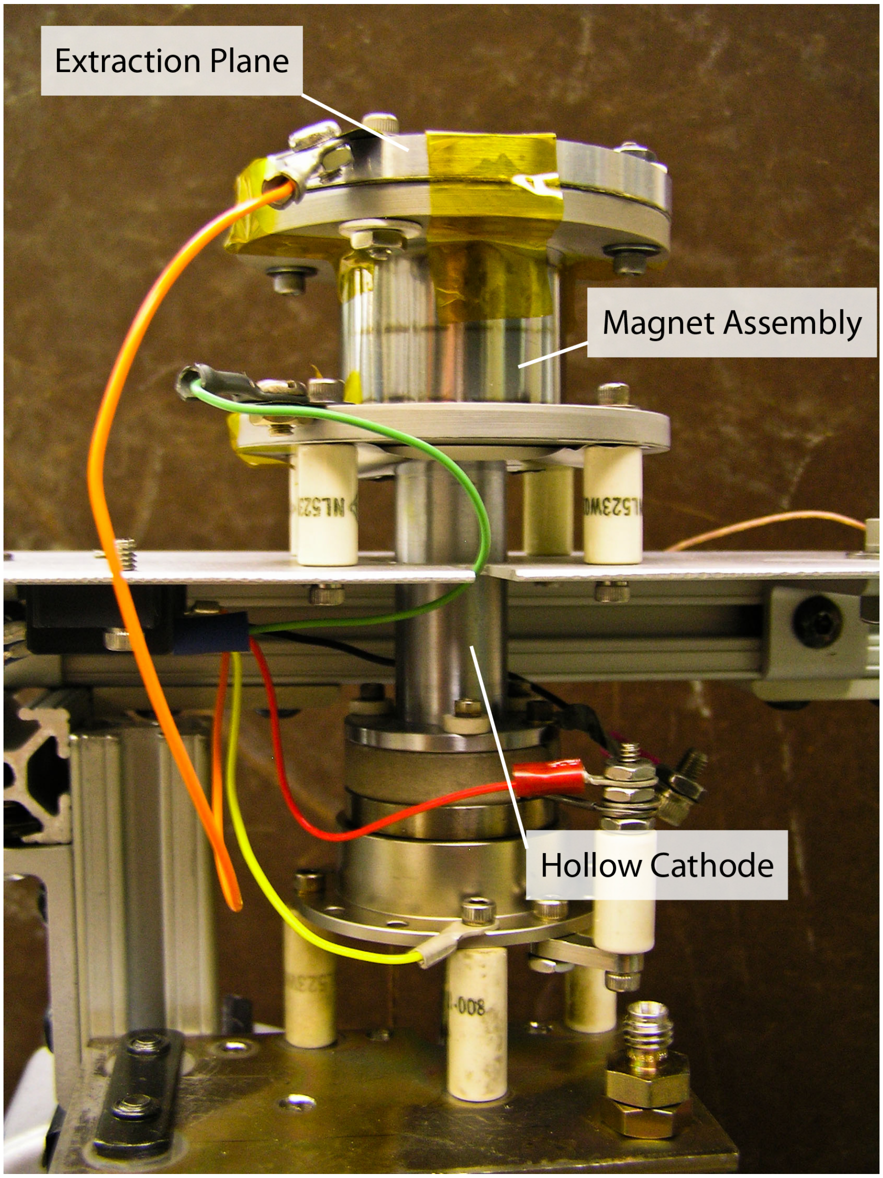

Figure 3.5: Miniature discharge device.

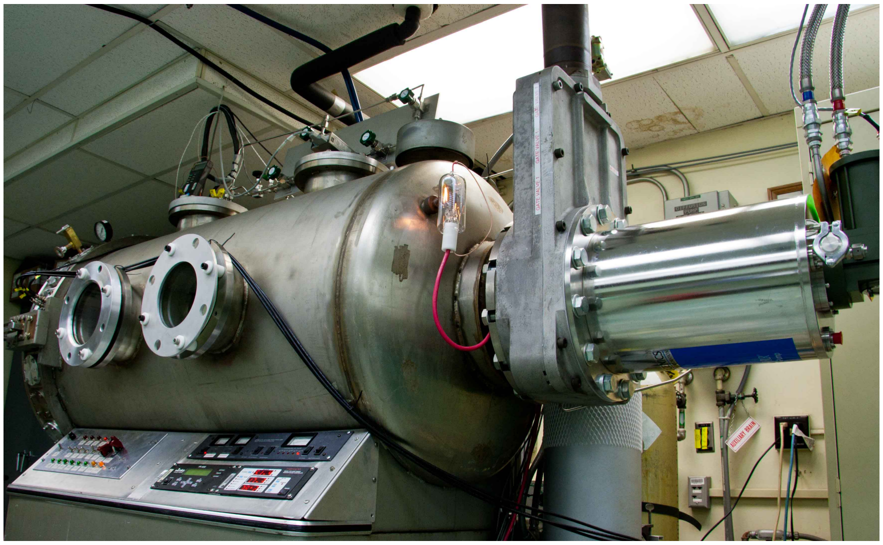

Figure 3.6: Vacuum chamber used for current effort.

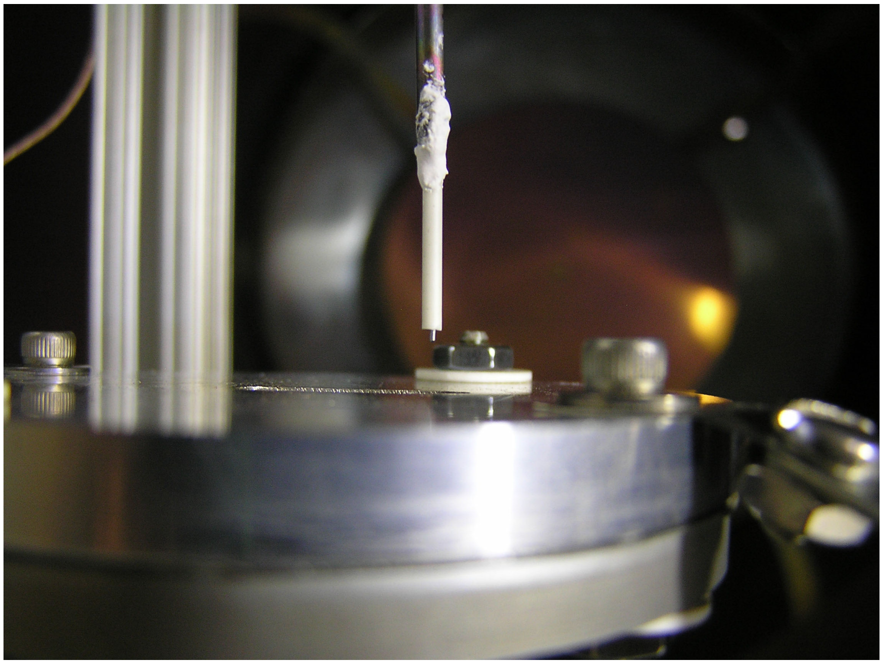

Figure 3.7: Cylindrical Langmuir probe. Probe dimensions are 0.5 mm in diameter and 1 mm in length and made from a tungsten wire with an alumina sleeve.

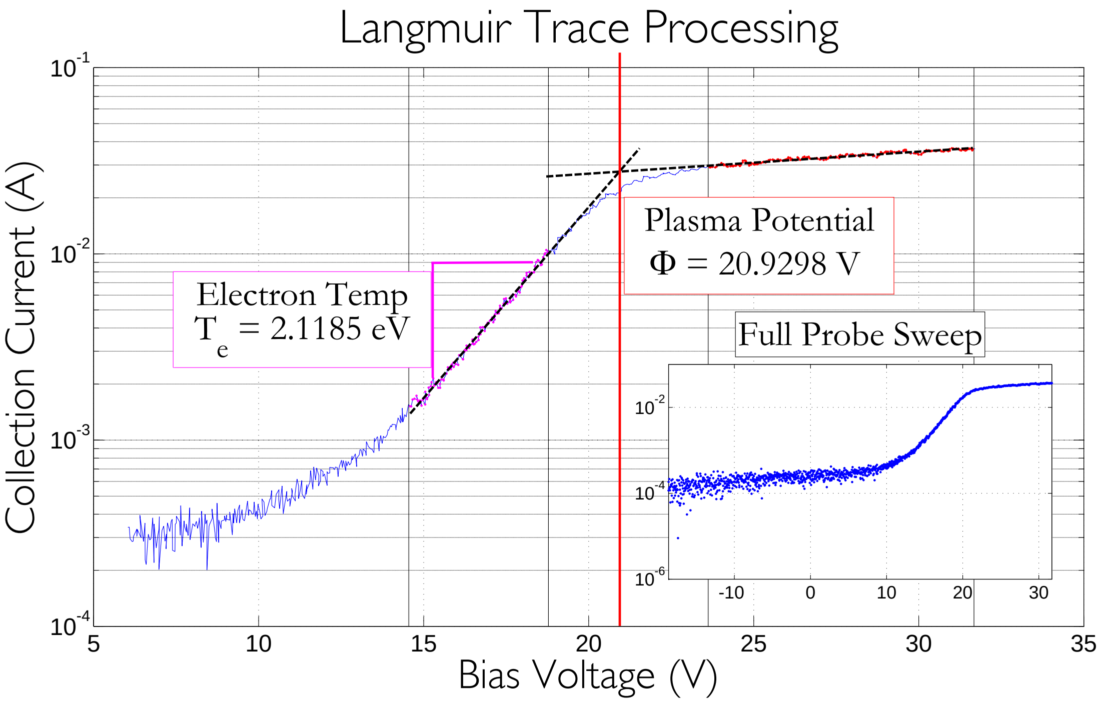

Figure 3.8: Example Langmuir trace.

is estimated to be 1.3×10^{-5} m, much smaller than the probe dimensions allowing for the thin sheath approximation. This states that all ions that enter the sheath are collected by the probe and do not orbit the probe.

The translation stages are capable of sub-mm step sizes, yet post-processing consideration, along with the probe dimensions, limit the grid resolution to a 1 mm x 1 mm. The measurement grid is overlaid in Figure 3.1. The total measurement domain is 14 mm x 35 mm, making for a total of 490 Langmuir traces for each case. Additionally, because of the large variance in plasma densities, each case must be run up to three different times due to the range of the data acquisition system. The sets of traces are then sorted and spliced together depending on the signal range. Finally, the individual traces are processed for electron temperature and plasma potential. It should be noted that the plasma density measurements are taken using a battery to bias the probe, as opposed

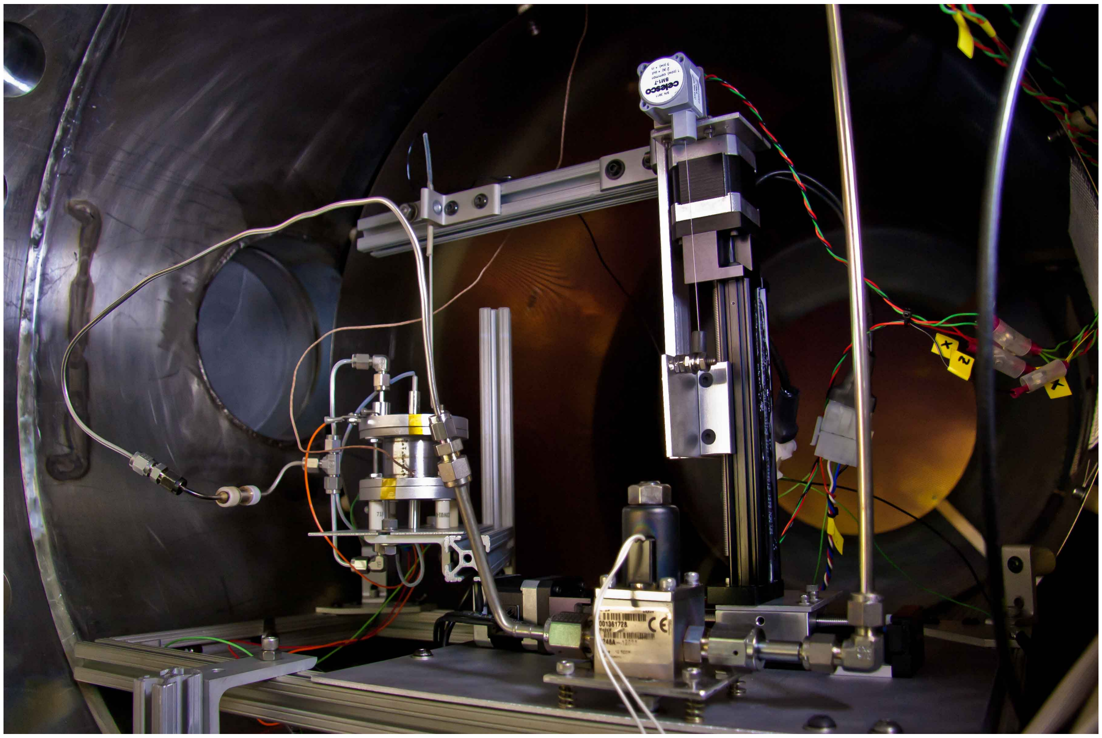

Figure 3.9: Miniature discharge testbed installation with translation stages and Langmuir probes.

to a regulated power supply, providing a relatively noise-free signal. As can be seen in Figure 3.8, the resulting probe sweeps are quite clean, but because the probe physically enters the plasma, the discharge voltage for a desired discharge current can vary throughout the measurement process. The deviation from the undisturbed discharge voltage is at most 10% and mainly occurs on the centerline when the probe obstructs the hollow cathode orifice. The disturbance falls off rapidly away from the centerline, and measurements taken toward the anode wall are true to the undisturbed plasma. The complete installation of the experiment is shown in Figure 3.9. The device in operation is shown in Figure 3.10.

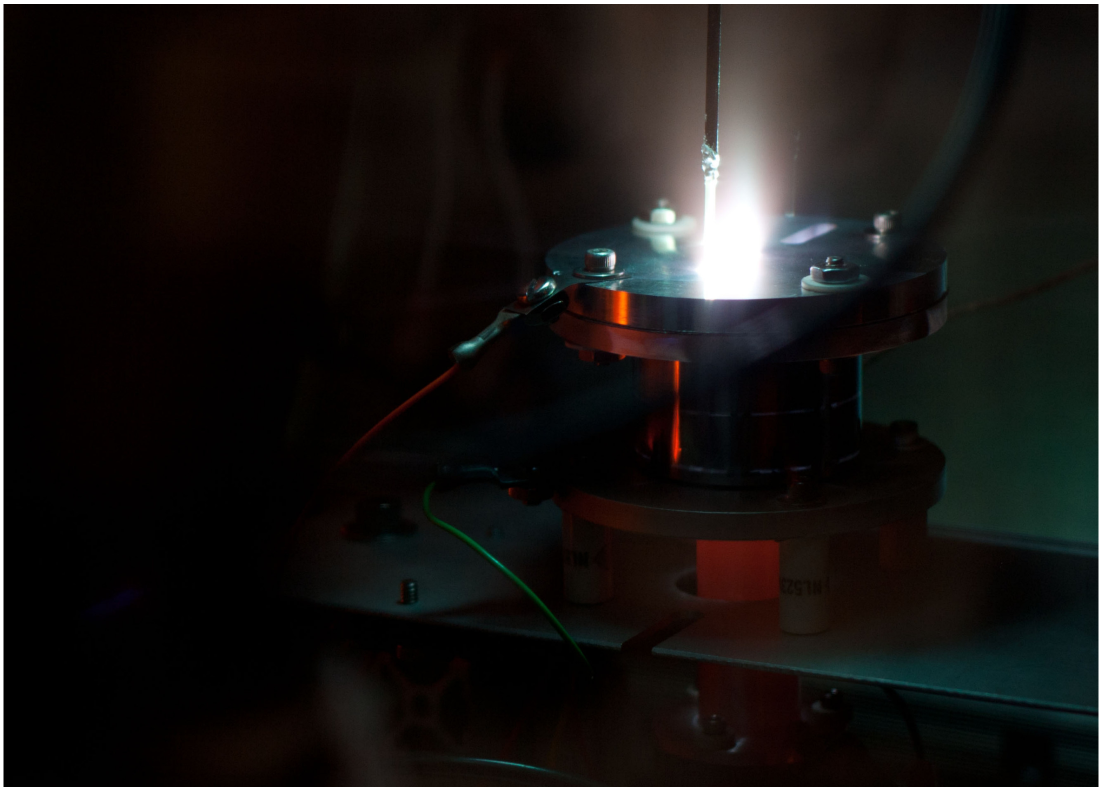

Figure 3.10: Miniature discharge device with hollow cathode operation. The exposure time has been increased to reveal the device's silhouette.

3.2 Magnetic Field Analysis

To facilitate the analysis of the plasma properties, it is useful to have an analytical expression for the magnetic field. Because the magnet width is much smaller than the chamber radius, it stands to reason that the magnetic field can be approximated by an axisymmetric field. Based on the work of Ravaud, Babic et al. developed an analytical formula for a radially magnetized ring magnet[37, 38]. These formulae, and the errors associated with making an axisymmetric assumption, can be found in Chapter 4. The plasma within the chamber is not expected to affect the magnetic field since the plasma density is relatively sparse or in the so-called low-β regime.

The magnets relative location to the measurements are shown to scale in Figure 3.11. The application of Babic's formulae to the magnetic field configurations are shown in Figure 3.12 and again in Figure 3.13 focused on the measurement domain. The values were checked using a hand-held Gauss meter. Both values on the centerline and the wall were measured and showed good agreement. The maximum field strength in the baseline configuration is 1877 G while the maximum field strength in the strong configuration is 2730 G agreeing with analytical calculations. The full domain inside the chamber is shown, where the dashed box outlines the measurement region that the probe is able to traverse. Here, it can be seen that the Langmuir probe is unable to measure directly against the wall. The thick lines are Stokes stream contours that represent magnetic field lines[39]. The calculation of the stream contours is discussed in Chapter 4 and provides a useful reference when evaluating the plasma structure contours. It is important to note the streamlines encapsulate a constant magnetic flux. The values of the plotted fluxes lines are the same for both cases in Figures 3.12.

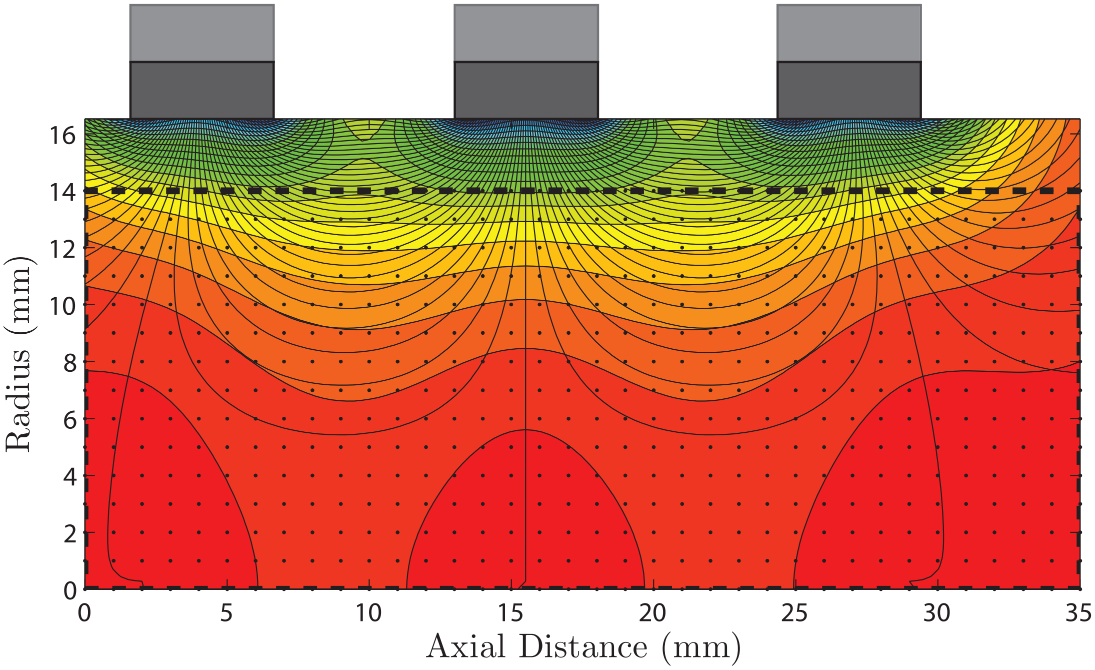

Figure 3.11: Schematic showing the magnet location to scale relative to the measurement domain. The magnets will be removed in all following figures. The convergence of field lines will be used to indicate the magnet location. The baseline configuration is shown. The additional magnet layer used for the strong configuration is shown faded.

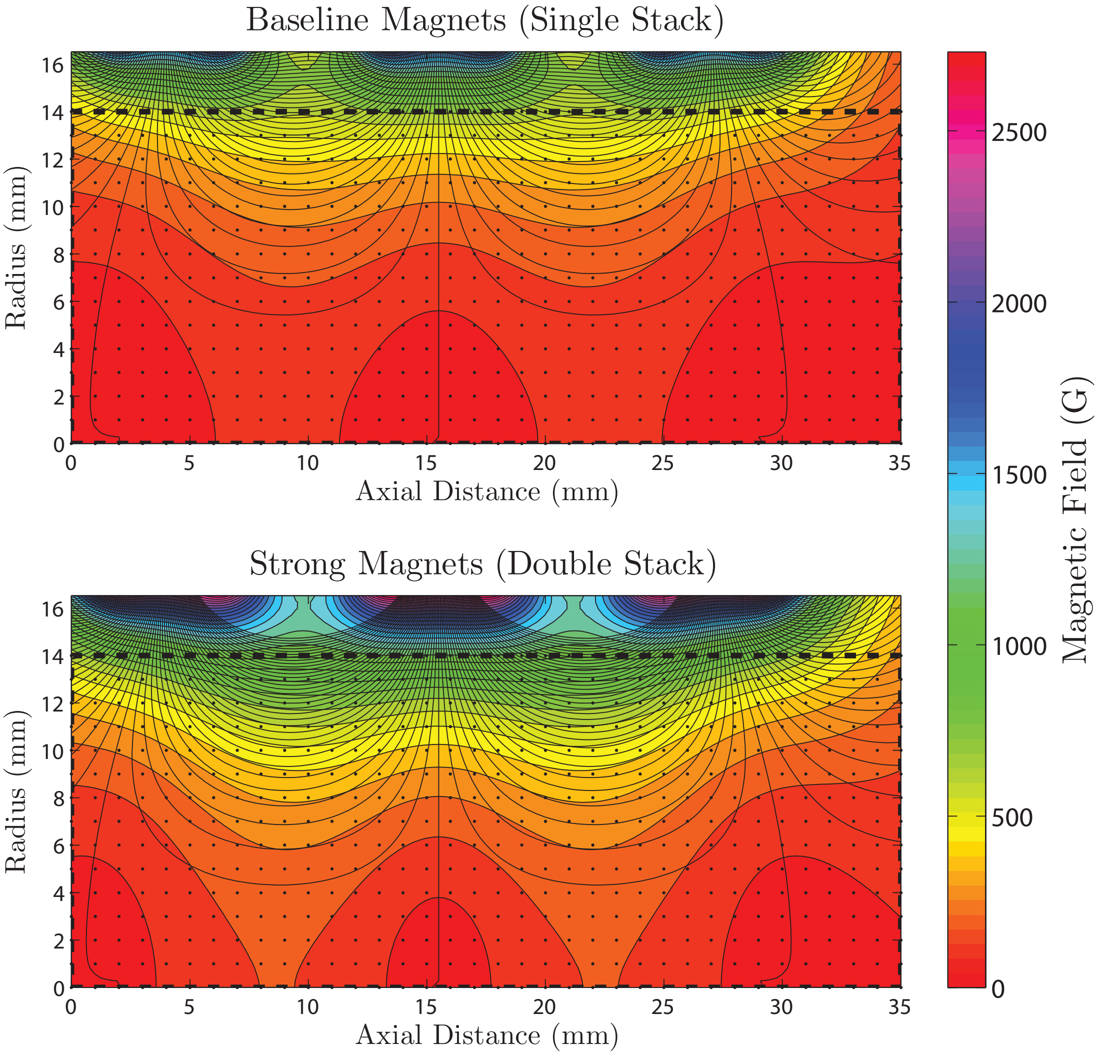

Figure 3.12: Analytical magnetic field calculations. The thick lines represent magnetic field lines. The dashed box and nodes show the measurement domain. Note the alternate color map used to highlight the differences in the weak field region where the red hue marks both extrema.

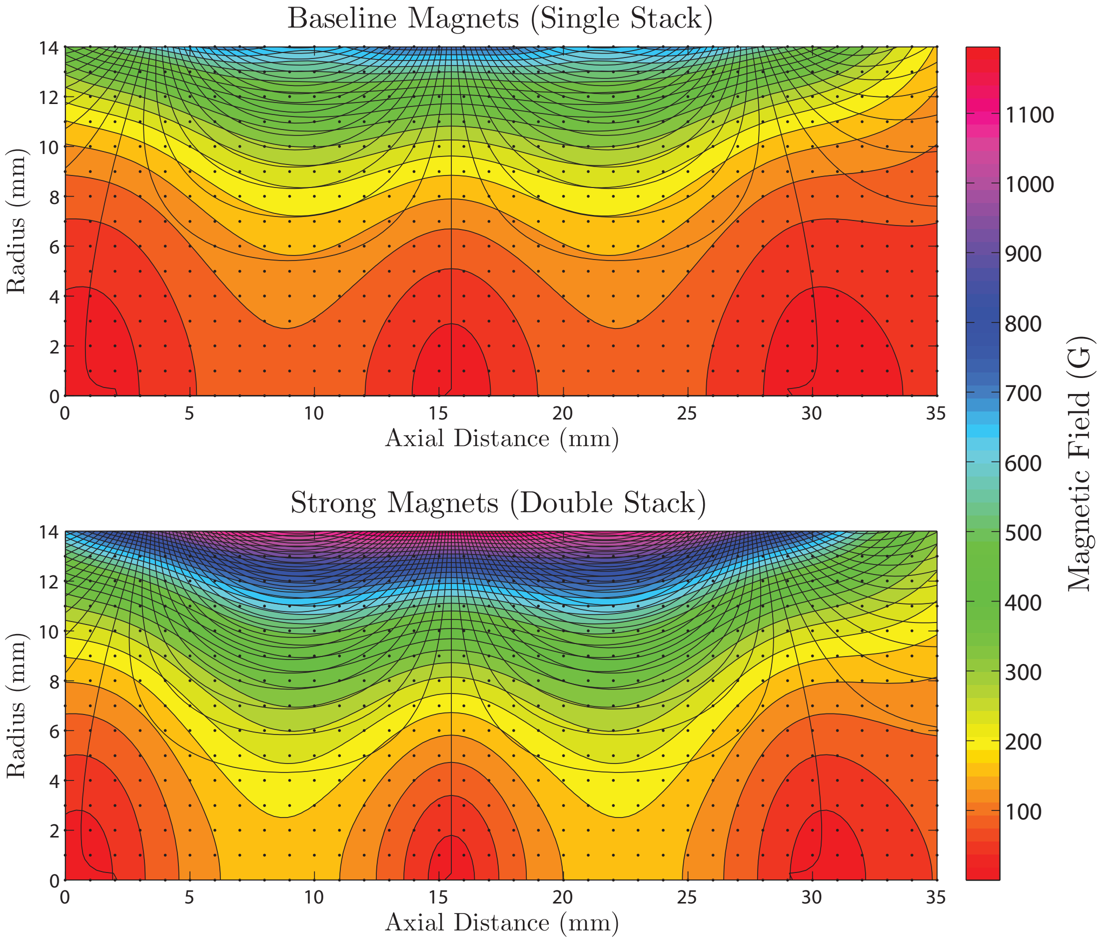

Figure 3.13: Figure 3.12 rescaled to the measurement domain.

3.3 Results and Discussion

Plasma measurements of the miniature discharge chamber are taken with both of the previously mentioned magnetic field configurations. Each field configuration is run at a discharge current of 0.5 A and 1.5 A. The total discharge voltage and resulting power is given in Table 3.2. The discharge chamber was preconditioned by running the discharge until thermal equilibrium was reached. This was measured with a thermocouple in contact with the magnets. Care was taken not to exceed 573 K, the maximum operating temperature for samarium cobalt (Sm_2Co_{17}). At this point, permanent demagnetization begins to occur. The equilibrium temperature range for all operating conditions was (450 K – 525 K). For all cases, the cathode was fed a constant 0.5 sccm xenon flow and the keeper current was maintained at 2 A to sustain the plasma in the hollow cathode.

Table 3.2: Discharge test matrix. Values represent average discharge voltage and power during operation.

	Baseline Magnets	Strong Magnets
0.5 A	(22.0 V, 10.0 W)	(19.7 V, 8.96 W)
1.5 A	(22.5 V, 32.8 W)	(22.7 V, 33.1 W)

3.3.1 Plasma Density

As stated above, each configuration was run for two discharge currents. The current changes the plasma density of the chamber by increasing the electrical power run through the discharge. The one amp difference in discharge current more than doubles the resultant plasma density throughout the chamber; however, if these data are normalized by the highest measured value, as shown in Figures 3.14 & 3.15, the qualitative features for a given magnetic field look similar. This suggests that the magnetic field not only determines the physical shape of the plasma, but also the relative density found at a given location. For the data shown, this approximation is good within 25% of the maximum density in the entire domain of the plasma. This approximation may prove useful for determining internal properties for different operating conditions for a single magnetic field; however, on a more detailed level, variations can still be observed between the discharge powers such as the slight spread seen in the strong magnet, high discharge power case. These minor variations can be used to help explain discrepancies seen in the electron temperature as discussed later. It should be noted that the irregularities within the plasma density stem from the density's dependence on electron temperature measurements as seen in Equation (3.1).

$$I_{sat} = 0.6enA_{probe}\sqrt{\frac{kT_e}{M_{Xe}}} \tag{3.1}$$

Magnetic confinement typically works on the principle that a stronger magnetic field should better utilize the primary electron energy by extending their residence time and creating a denser plasma. This is reflected in the maximum density values for the strong magnet configuration. However, it is clear that the baseline magnetic field fills the volume of the discharge chamber. This can be shown with an effective plasma density using

$$n_{eff} = \frac{\iint n(z,r)r\mathrm{d}r\mathrm{d}z}{\iint r\mathrm{d}r\mathrm{d}z} \tag{3.2}$$

The effective plasma densities are shown in Table 3.3. Note that although the high power cases have similar effective densities, the baseline configuration is

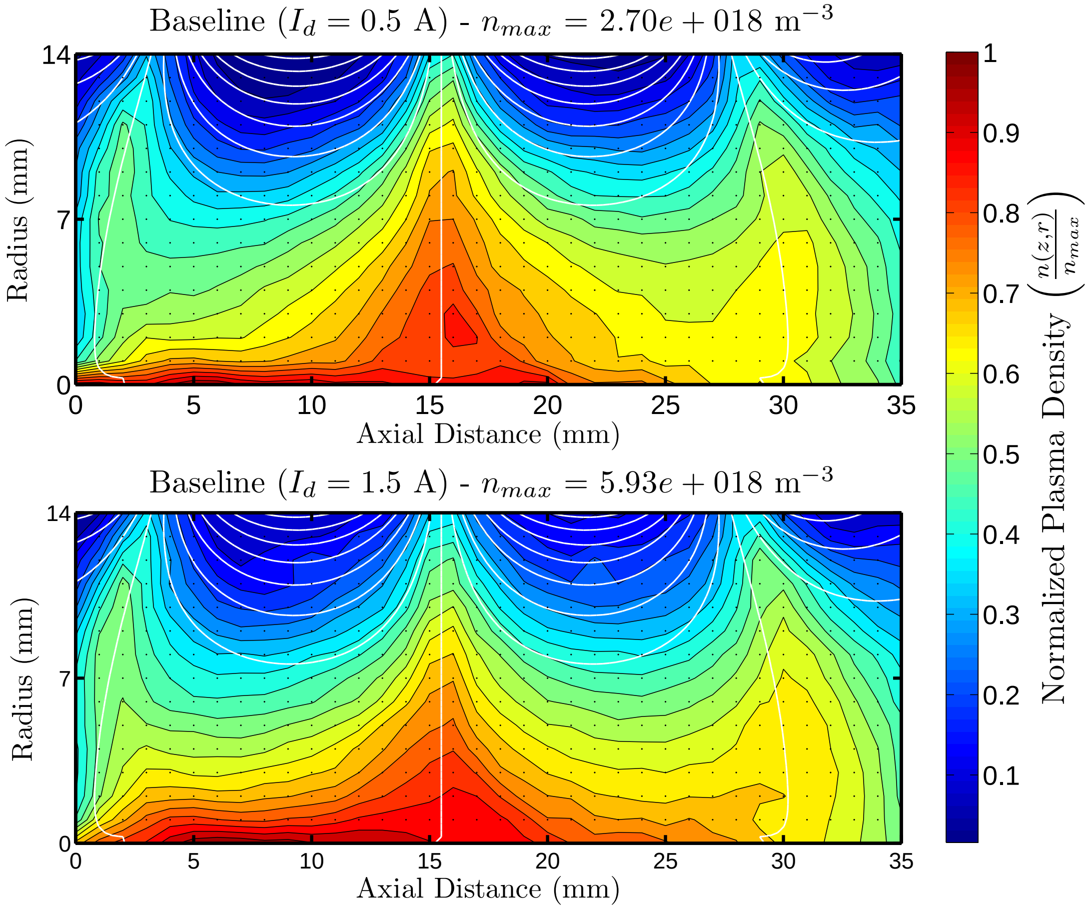

Figure 3.14: Plasma density for the baseline configuration. Plasma density measurements are normalized by the max density value.

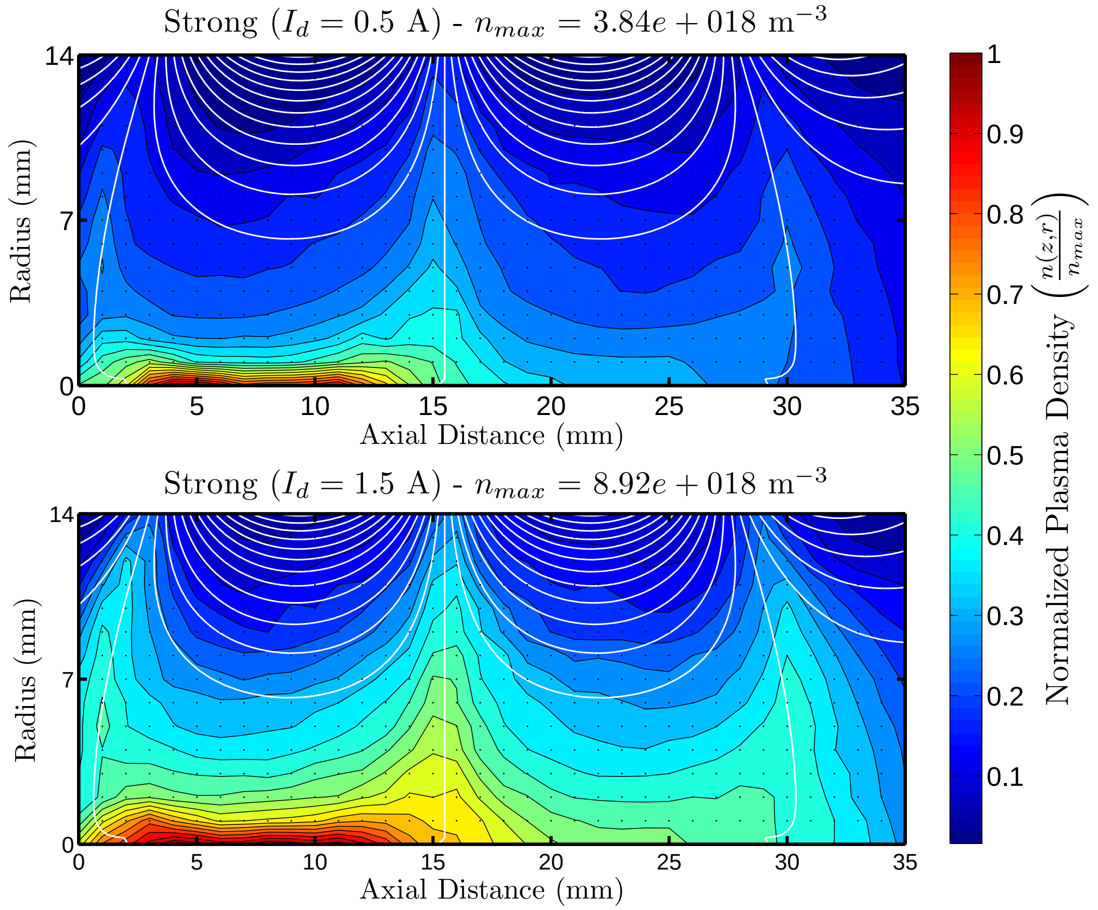

Figure 3.15: Plasma density for the strong magnetic field configuration. Plasma density measurements are normalized by the max density value.

more uniform and thus delivers more plasma to the extraction region. This keeps with the thought that a field-free region is better for performance[40]. Further, state of the art miniature ion thruster design would suggest that choosing magnet strength is a trade-off between confinement and plasma stability. As one may anticipate, Figure 3.14 shows that miniature ion thrusters must still obey the tenet of employing a field-free region to improve discharge utilization. In fact, the density at the edge of the domain, where the extraction grids would be, shows that the theoretical beam is flatter in the baseline case. This is a desirable property for extraction grid utilization efficiency and thruster life. This occurs because the magnetic field does not prevent diffusion to the radial extremes of the grids as it does in the strong configuration. The strong configuration's density profile is concentrated to the center line which signals poor volume utilization of the discharge chamber. The magnetic field over-confines the plasma in this case. This creates a higher maximum plasma density but lower uniformity. Figures 3.14 & 3.15 as well as the following measurement plots have the hollow cathode located at the origin. This explains the negative axial gradient.

Table 3.3: Effective plasma density, n_{eff}, is given by the total particle count normalized by the discharge chamber volume.

	Baseline Magnets (m^-3)	Strong Magnets (m^-3)
0.5 A	1.05×10^{18}	6.06×10^{17}
1.5 A	2.35×10^{18}	2.32×10^{18}

To measure approximate thruster performance parameters, the technique similar to that proposed by Brophy is used to account for an equivalent neutral flow rate[34]. Brophy's model requires grid transparencies and currents, neither of which are present in the system; therefore, a modification of the method, similar to that used by Goebel, must be applied[36]. Two main assumptions are made in order to obtain the approximations. The first is that the values measured at the exit are azimuthally symmetric. The second assumes that the exit values occur at the sheath entrance to the extraction plane. The plasma density can then be integrated to approximate the beam current using Equation (3.3). This is integrated numerically using a simple trapezoid scheme. Note that the beam is only taken out to the measurement region and is not extrapolated to the anode wall. This region is simply neglected and can be assumed to be similar to the end of the gridded region. Strictly speaking, Equation (3.3) calculates the ion current to the plane of the screen grid rather than the actual beam current, thus the beam current is approximated by assuming an ion transparency for the extraction planes. Here the Bohm velocity is assumed due to the positive potential with respect to the cathode surface[25].

$$I_b = (2\pi e)\eta_{trans} \int_0^R n(r, z_{max})r \left(0.6\sqrt{\frac{kT_e(r, z_{max})}{M_{Xe}}}\right) \mathrm{d}r \tag{3.3}$$

With an approximation for the beam current, discharge losses and mass utilization can be calculated. It is important to remember that the device was not optimized for performance. Instead, it was built to investigate the physical behavior in miniature discharges. In that regard, these values should not be taken to indicate miniature ion thruster performance, but rather the floor for such a device's capability.

The discharge loss given in Equation (1.5) can be modified to include the power to the keeper. This is given in Equation (3.4). Because the miniature hollow cathode is replaced with a relatively large neutralizer cathode that is designed for much larger thrusters, the discharge loss is unrealistically high if the keeper power requirements are included. To account for this, the keeper power is assumed to be negligible to determining a ceiling in performance for this miniature discharge. One could also assume a comparable power fraction between the discharge and keeper given the development of a proper miniature hollow cathode source. Conservatively, the keeper power is typically less than 5% of the discharge power, so 0%-10% is used in these calculations, where 0% represents the idealized case of no required keeper power.

$$\varepsilon_{Bk} = \frac{I_d V_d + I_k V_k}{I_b} \tag{3.4}$$

The mass utilization from Equation (1.4) is typically a function of grid transparency and other extraction assembly properties. Because there is no beam extraction, the ions hitting the cathode surface must be treated as a virtual gas feed. To first-order, the virtual gas feed is simply the beam current to the extraction plane less the area of the access slot. This ignores the radial variance in discharge properties. Equation (3.6) gives the formula used to calculate the adjusted mass utilization efficiency. Because of the 3 cm scale, miniature ion thrusters can use optics with small apertures which help keep the neutral density high, hence the neutrals transparency due to the access slot is $\sim 10\%$, similar to that found in MiXI.

The summary of the approximate discharge losses and the mass utilizations are shown in Table 3.5. The beam currents are calculated by integrating the density values at the screen grid plane. The reported values assume an 80% ion transparency. The neutral temperature is assumed to be equal to that of the chamber wall[1]. From a plasma density analysis, the baseline magnetic field outperforms the stronger field in every way. The baseline magnetic field produces a higher total beam current as shown in Figure 3.16 and the beam flatness parameters, as given in Equation (3.5), are nearly similar. This is shown in Table 3.4. These are poor flatness parameters; however, the magnetic field is designed for symmetry and not for optimized plume profiles. Even though the strong field configuration has a higher peak density, the magnetic field structure does not allow the plasma to efficiently utilize the volume of the discharge chamber or the extraction area. This is reflected in the discharge loss where it is postulated that a small ionization volume in the strong, low current case is responsible for the relatively high discharge loss. Given the conservative 0%-10% of a proper miniature hollow cathode, the discharge loss falls well within the range of typical ion thrusters. There is certainly strong evidence towards favorable performance for miniature ion thrusters. Further research efforts should continue with the development of a miniature hollow cathode[41, 6].

$$F_B = \frac{\int_0^R 2\pi r \frac{n(z=L,r)}{n_{max}} \mathrm{d}r}{\pi R^2} \tag{3.5}$$

Table 3.4: Beam flatness parameters, F_B, for operating conditions. Note that the device is not tuned to achieve favorable beam flatness.

	Baseline Magnets	Strong Magnets
0.5 A	0.29	0.31
1.5 A	0.10	0.15

$$\eta_m = \frac{M_{Xe} I_b}{e\dot{m}_d} = \frac{1}{\frac{I_{in}}{I_b} + \frac{A_{cat}-A_{slot}}{A_{cat}}} \tag{3.6}$$

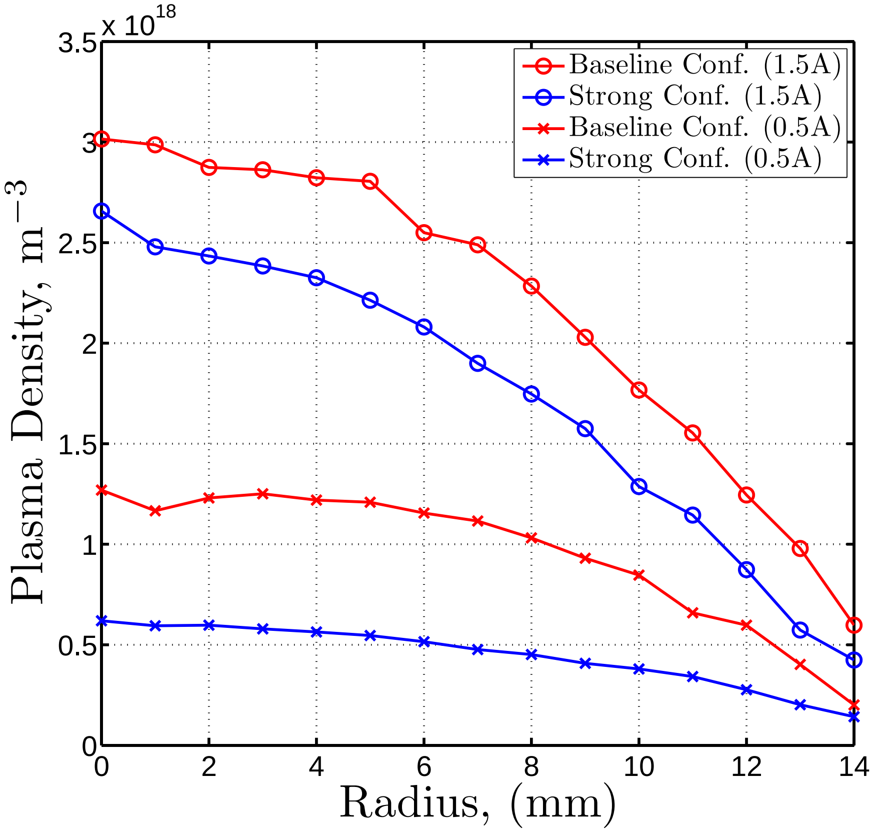

Figure 3.16: Plasma density at the extraction plane. The baseline configuration delivers more plasma with similar uniformity.

Table 3.5: Summary of calculated performance values for the ring-cusp discharge experiment. Beam currents are reported with $\eta_{trans} = 80\%$ to approximate reduction from the extraction apparatus.

Magnet ID	I_b (mA)	P_d (W)	P_k (W)	ε_{Bk} $(\frac{\text{eV}}{\text{ion}})$ w/ P_k	ε_{Bk} $(\frac{\text{eV}}{\text{ion}})$ $P_k = (0-10\%)P_d$	η_m	T_o(K)
Baseline 0.5 A	47.9	10.0	32	876	209-230	60.5%	158
Baseline 1.5 A	109.6	32.8	26	536	299-329	81.3%	206
Strong 0.5 A	20.6	8.96	30	1888	434-478	37.7%	185
Strong 1.5 A	75.0	33.1	26	788	441-486	72.4%	238

3.3.2 Electron Temperature

The electron temperature measurements are taken from individual Langmuir traces. Because there is a fair amount of subjective choice in the post-processing procedure, the noise can be rather large when compared to the relatively smooth plasma density data. The electron temperature profiles are presented in Figures 3.17 & 3.17. Qualitatively, the electron temperature does not change very much for the different discharge powers in the baseline magnetic field configuration. This is consistent with the theory that the electron temperature is primarily dominated by neutral density where high neutral densities lead to low electron temperatures[1]. This is keeping with the finding in the previous section that the device is operating in a favorable discharge loss regime for the baseline magnetic field. The figures show that the electron temperature is nearly constant along a field line for both cases. Further, the baseline field case shows a higher temperature at the centerline indicating neutral depletion. This is reflected in the favorable mass utilization efficiencies of the baseline case.

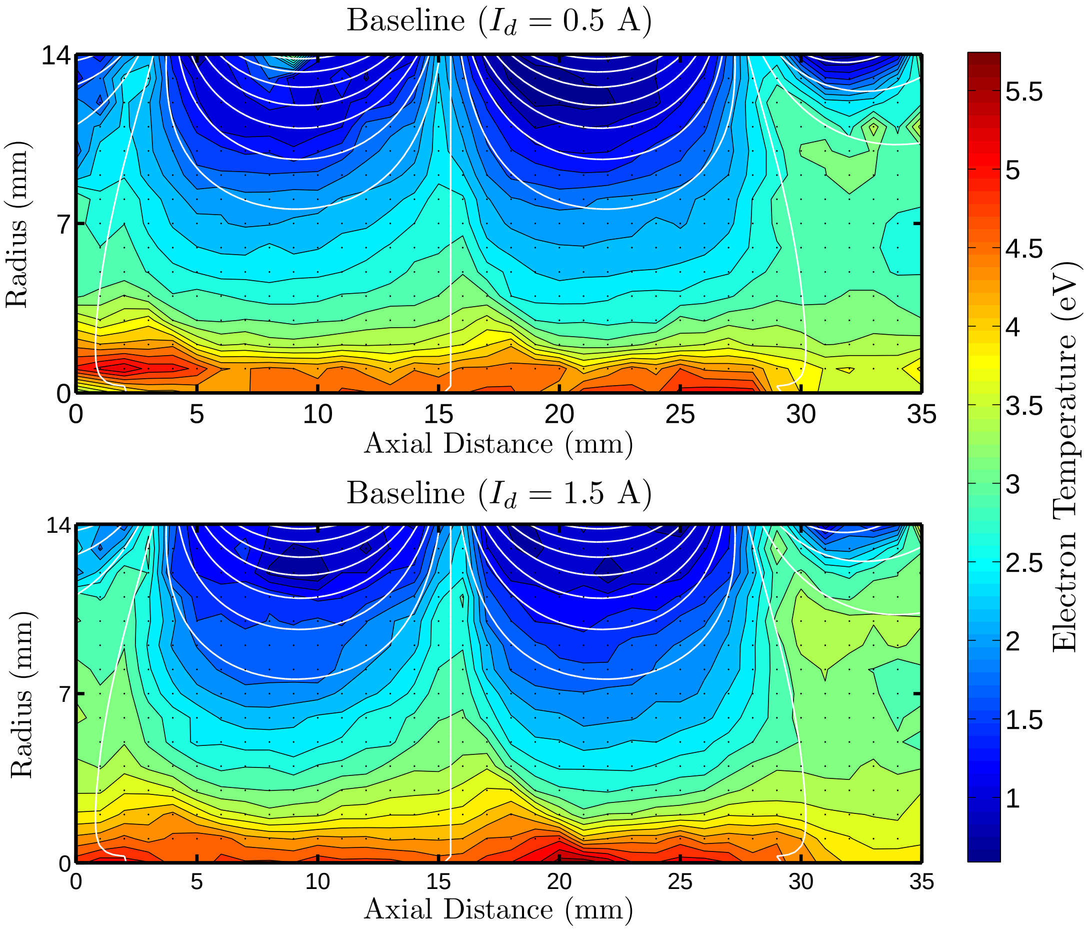

Figure 3.17: Electron temperature for the baseline magnetic field configuration.

In contrast, the strong magnetic field configuration cases have visibly different behavior. The 0.5 A case has lower overall electron temperatures. This could be explained by a general inefficiency in ionization. The peaked plasma density profile shown in Figure 3.15, along with the low electron temperatures in Figure 3.18, suggest that ionization occurs in a confined region and is quickly replenished by surrounding neutrals. The high discharge power case more efficiently utilizes the mass which is supported by the relatively larger plasma density seen in Figure 3.15.

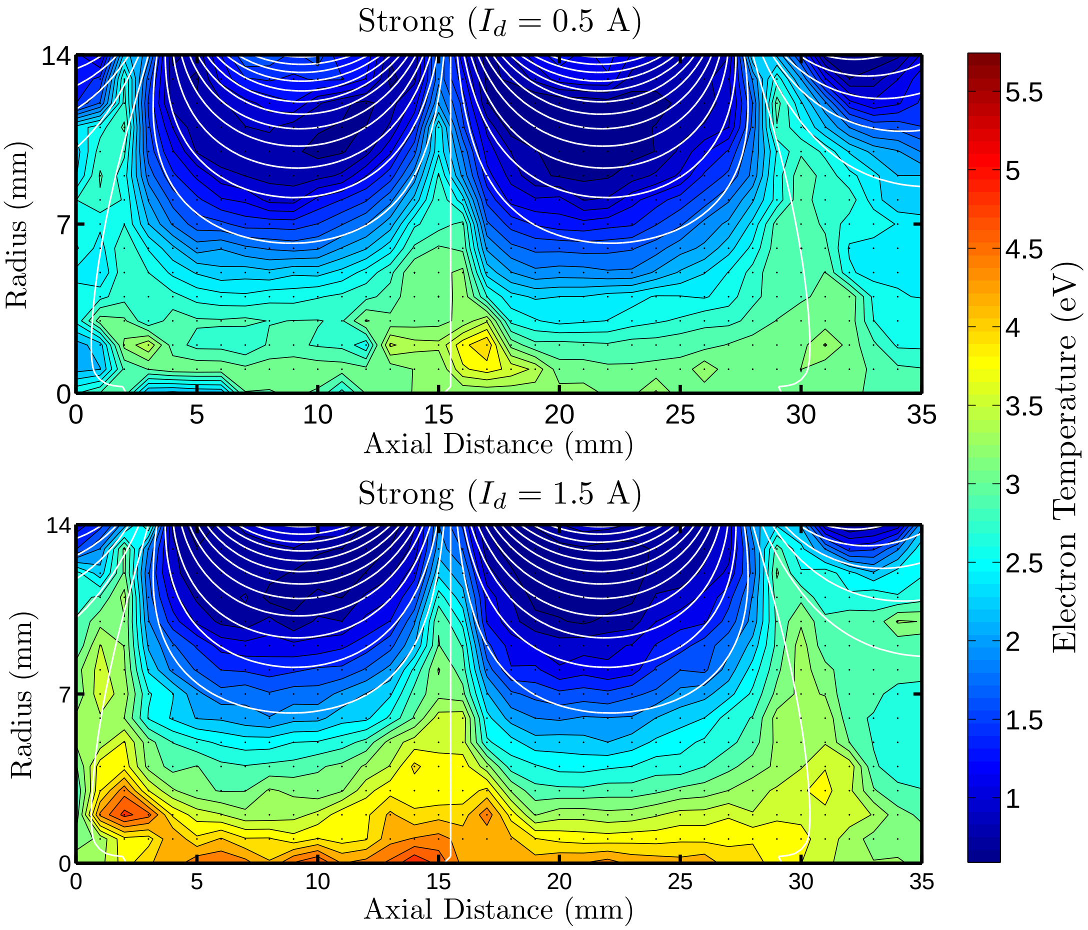

Figure 3.18: Electron temperature for the strong magnetic field configuration.

3.3.3 Plasma Potential

The overall plasma potential within the chamber is governed by the discharge voltage seen at the anode surface. The voltage is set in order to fulfill the current demanded by the power supply. Because of this, the plasma potential measurements shown in Figures 3.19 & 3.20 are scaled relative to the anode voltage. Similar to the other plasma properties, the potential structure is a function of the magnetic field configuration and invariant to the discharge power. In the baseline magnet field configuration, potential valleys can be seen around $r = 7$ mm into the discharge chamber. In contrast, the double stacked magnetic field configuration does not have local minima apart from the centerline. From the perspective of a newly born ion, the potential field would draw the ion to utilize the chamber volume in the baseline field and towards the centerline in the strong field case.

The potential structure is indicative of an over-confined plasma. Typically, a plasma establishes a positive potential with respect to the anode due to the energetic electrons reaching the wall too quickly. The sheath acts to maintain the quasi-neutrality by impeding the electron progress to the wall. In a case such as MiXI, where stronger magnets may be required, the magnetic fields tend to be stronger locally and confine the electrons. This instead would cause rapid ion loss to the walls. To counteract this, the bulk plasma establishes a negative potential with respect to the wall in order to maintain quasi-neutrality. From a performance perspective, this electrostatic ion confinement reduces ions loss to the wall; however, if the potential drops too low, there will be insufficient primary energy for ionization as discussed in Chapter 2.

In the baseline case, there seems to be a hybrid of plasma scenarios. In the center, the field is weak enough to establish a semblance of a bulk plasma. This is seen at $z = 15$ mm on the centerline in Figure 3.19. From there, the magnetic

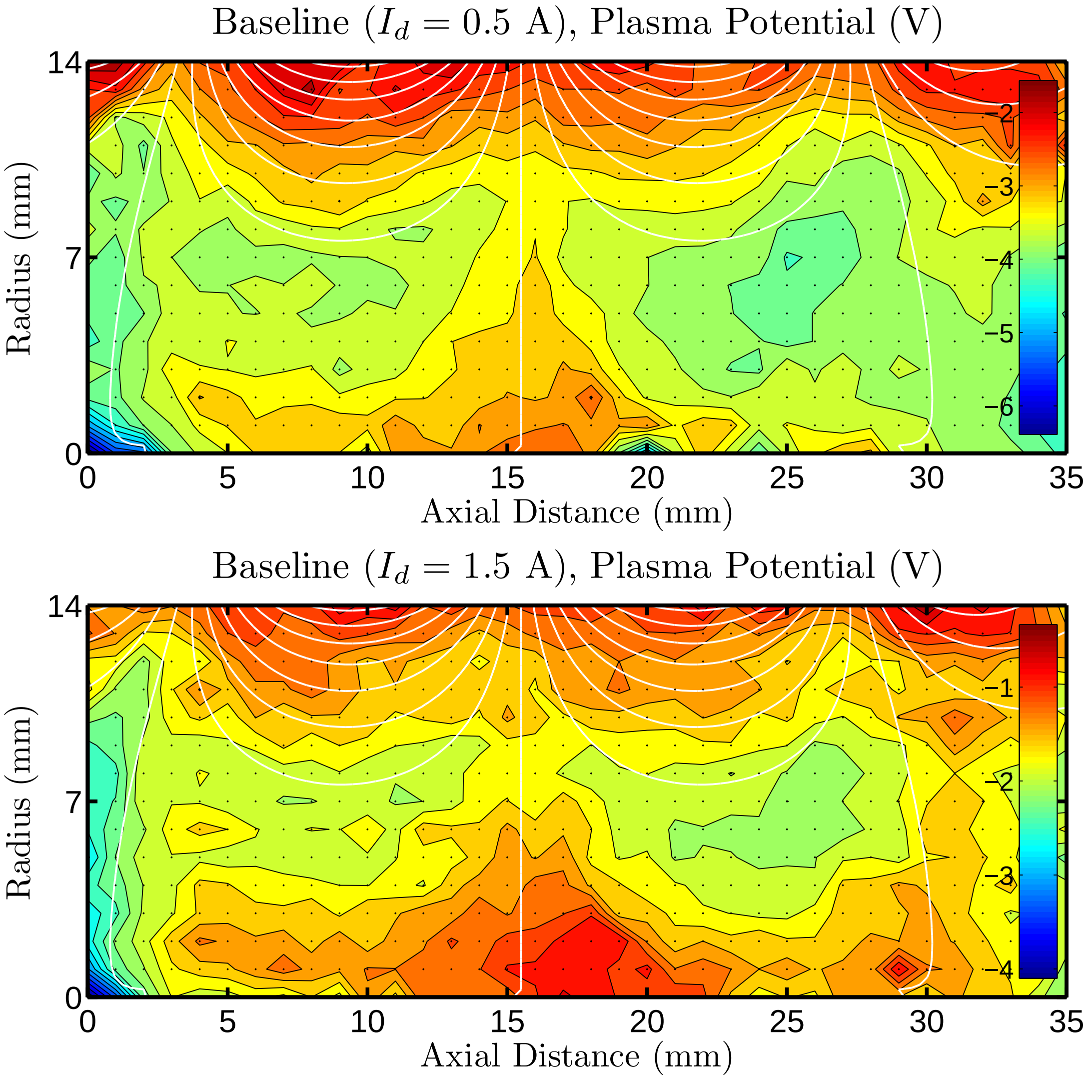

Figure 3.19: Plasma potential measurements for the baseline configuration. Plasma potentials are reported with respect to the anode voltage.

field begins to restrict the electron flow and a negative potential is established. This feature is seen in larger devices under certain conditions, but it is likely a more prominent problem in miniature ion thrusters due to the larger surface to volume ratio.

The strong magnet case's potential structure in Figure 3.20 indicates the higher magnetic fields are likely to approach the onset of instability at the cathode region. The confinement of the electrons is strong enough to extend the cathode potential, yet there is still sufficient energy for ionization.

3.4 Experimental Summary

The internal plasma measurements presented in the current effort provide insight into the behavior of miniature ring-cusp discharges. By scaling the plasma parameters, it is shown that the plasma density, electron temperature, and plasma potential structures are determined by the magnetic field configuration. The plasma density, when normalized by the peak density value, appears to be independent of discharge power. This empirical conclusion is useful in predicting, to first-order, the normalized plasma density topography within a discharge chamber for a given magnetic field configuration as discussed in subsequent chapters. The electron temperature does not vary greatly for the different discharge powers; therefore, it does not require scaling. This occurs because of the constant flow rate used since the neutrals act as a sink and suppress the electron temperature. The plasma potential is strongly correlated with the overall plasma density; however, the potential structures are largely determined by the magnetic field.

The comparisons of the strong and baseline magnet cases show that the latter configuration is better for both stability and performance. The baseline field con-

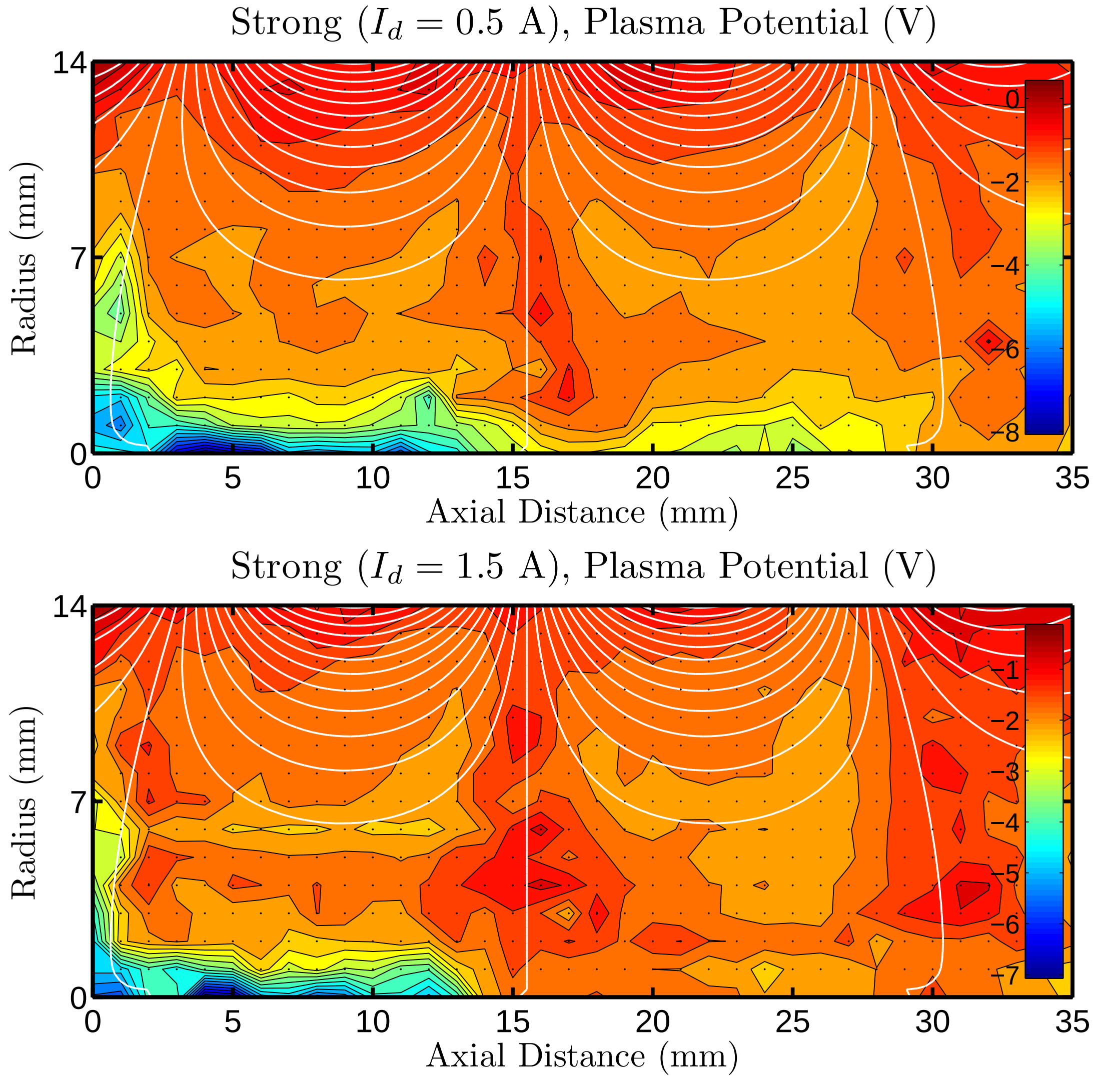

Figure 3.20: Plasma potential measurements for the strong configuration. Plasma potentials are reported with respect to the anode voltage.

figuration also behaves favorably from a plasma discharge utilization perspective as shown by the mass utilization efficiency. Although the maximum value for the plasma density is much higher in the strong magnet case, the field strength does not allow the plasma to spread throughout the chamber. Most importantly, it inhibits migration to the extraction region at the downstream end of the discharge. Consequently, the plasma density at the extraction plane is much lower and peaked for the strong magnet case. This makes it less favorable from a thruster or ion source perspective[21].

Performance values were approximated using the plasma density at the downstream cathode surface. The results show the baseline configuration's superiority and demonstrated expected performance values for both cases. Given a properly designed miniature hollow cathode, the performance values are on par with traditional ion thrusters. This assumes a similar discharge to keeper power ratio. While the focus of this research was the fundamental plasma structure, these results support the overall confidence in miniature ion thruster technologies and improves the understanding of discharge behavior and performance at this scale.

CHAPTER 4

Magnetic Field Analysis

The measurements in Chapter 3 demonstrate a correlation between the magnetic field configuration and the plasma behavior when scaled appropriately. Traditionally, ion thrusters are designed by dictating a maximum closed contour for the magnetic field strength[42]. This value is chosen to be strong enough to provide good plasma confinement, yet still allow a large field-free region in the bulk of the plasma chamber. This field-free region creates a relatively uniform plasma region that can be investigated to first order with a bulk control volume analysis[1]. Due to the requirement to provide a cusp field strength sufficient for mirror confinement (1-3 kG), the field free region for miniature discharges is a small portion of the discharge volume. Therefore, the magnetic field in a miniature discharge is prominent and the plasma cannot be analyzed using uniform approximations. While still important for an efficient discharge, as shown in Chapter 3, often the field free region is smaller than that of the magnetically dominated region. In these cases, it is useful to develop an alternative coordinate system that accounts for the magnetic field complexity. Additionally, recent studies suggest that the magnetic field geometry plays a considerable role in larger devices, further motivating the need for a more detailed magnetic field analysis beyond the maximum closed contour[43].

In order to quantitatively analyze the miniature plasma chamber, a methodology using the magnetic field lines seen in Figure 3.12 is developed. The field lines are described using a Stokes stream function which has properties that are closely related to the adiabatic invariants seen in charged particles. By definition, the constant contours of the stream function are everywhere tangent to the magnetic vector field. Developing a coordinate system around the stream function allows the plasma to be analyzed in complex magnetic fields while still maintaining the ability to decouple anisotropic behavior, namely parallel and perpendicular to the magnetic tangents. The objective of the current chapter is to develop a general framework for studying all axisymmetric magnetized plasmas in the low-β regime.

4.1 Stream Function Construct

The magnetic field lines shown in Figure 3.12 show the local tangent along with the magnitude. That is, the density of the field lines correspond to the relative field strength of the local magnetic field. Typically, computed lines seen in plasma literature are simply path lines traced from some initial position. These contours typically only yield the direction of the magnetic field without any correlation to the magnitude. This is similar to the stream function used in fluid mechanics.

In incompressible flow, constant stream function contours trace out path lines from the velocity vector field; however, the values of the stream function contours also give some indication of the volumetric flow rate[44]. In a two dimensional geometry, the difference between any two stream function directly yields the volume flow rate, or velocity flux, between the contours as shown in Figure 4.1. In regions of acceleration, the distance between stream functions must converge in order to maintain constant flux. Replacing the velocity vector with the magnetic vector field gives a way to generate magnetic field lines. In order to make this substitution, the surrogate vector field must be solenoidal just like the velocity

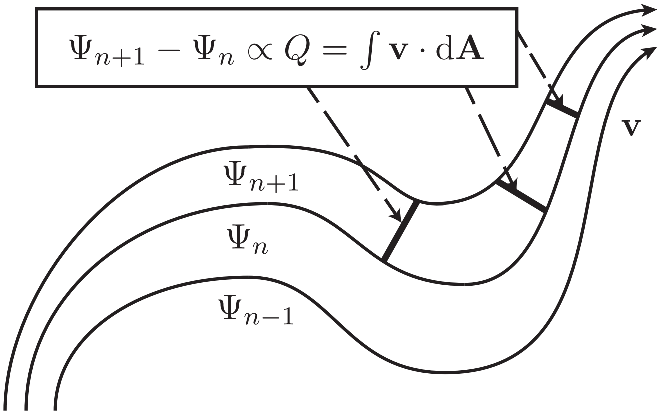

Figure 4.1: In incompressible flow, the volume flow rate is given by the difference in stream function contours.

field in incompressible flow. This condition is satisfied for the magnetic field by Gauss's law for magnetism in Maxwell's equations given in Equation (4.1).

$$\nabla \cdot \mathbf{B} = 0 \tag{4.1}$$

Typically a stream function can only be defined in two-dimensions; however, if a dimension can be eliminated by symmetry, such as in spherical or cylindrical coordinates, a Stokes stream function can be defined[39]. Note that the "Stokes" designation simply refers to an axisymmetric domain. Equation (4.2) gives the differential equation for the Stokes stream function contours. Much like the two-dimensional case the stream function contours are directly related to the vector flux, but in the case of a Stokes stream function, the zero stream function is always the axis of the surface contour. Therefore, the stream function value at a particular location gives the total flux through a stream tube with Equation (4.3). The flux through an annulus can be calculated by subtracting the stream function values of two stream tubes as illustrated in Figure 4.2.

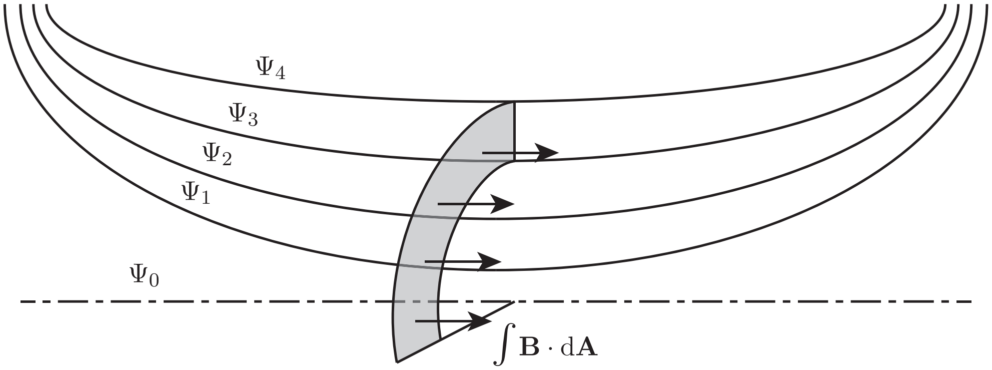

Figure 4.2: Stokes stream function construct applied to a magnetic field.

$$B_r = \frac{1}{r}\frac{\partial \Psi}{\partial z} \ ; \ B_z = \frac{-1}{r}\frac{\partial \Psi}{\partial r} \tag{4.2}$$

$$\int_{\Psi_b}^{\Psi_a} \mathbf{B} \cdot \mathrm{d}\mathbf{A} = 2\pi \Delta \Psi \tag{4.3}$$

4.2 Charged Particle and Plasma Motion

In a low-β plasma, where the magnetic field is unchanged due to the local plasma currents, the ambipolar plasma motion is closely tied to the vacuum magnetic field. The Stokes stream function simplifies the magnetic domain by outlining the the constrained motion of the plasma. This constrained motion ties features of the stream function to the adiabatic invariants[25]. For example, as an electron goes through it's helical gyromotion, the guiding center of the electron remains along a constant stream function value in the absence of collisions. Additionally, as the electron is reflected due to the magnetic mirror effect[45], its oscillations remain on the same stream function value. Finally, the azimuthal drifts due to the interactions of the charge particles and the fields act to contain a constant magnetic flux. This property is known as the third adiabatic invariant and is exactly the quantity described by the Stokes stream function.

From the short timescale gyromotion behavior to the relatively long timescale processional motion, undisturbed charged particles remain on the stream tube values described in Section 4.1. However, in a partially ionized regime, such as those found in ion thrusters, collisions are quite frequent. Therefore, rather than using the stream function to describe constrained motion, it is used as the basis for a flux aligned coordinate system to decouple constrained plasma motion with collisional diffusion across field lines.

4.3 Magnetic Field Aligned Coordinates

The stream function contours provide a convenient foundation to describe all magnetized plasmas. The low-β regime allows for the assumption of a stationary magnetic field and consequently the basis for a stationary coordinate system. Typically plasma equations of motion are separated into perpendicular and parallel components to analyze the decoupled behavior[46]. This analysis is largely academic and can be quite difficult to apply to complex configurations such as a magnetic ring-cusp. By developing a coordinate system based on the stream function values, the decoupled analysis can be used for any axisymmetric configuration[47]. A representation of this coordinate system in seen in Figure 4.3. The orthonormal basis chosen has three components, the stream function, the azimuthal coordinate, and the magnetic scalar potential. Because the basis chosen is orthonormal, the direction of the vectors can be considered to be the gradient of the scalar field[48]. Below, the physical interpretations of these values are described. Following the calculation of the values, the mathematical

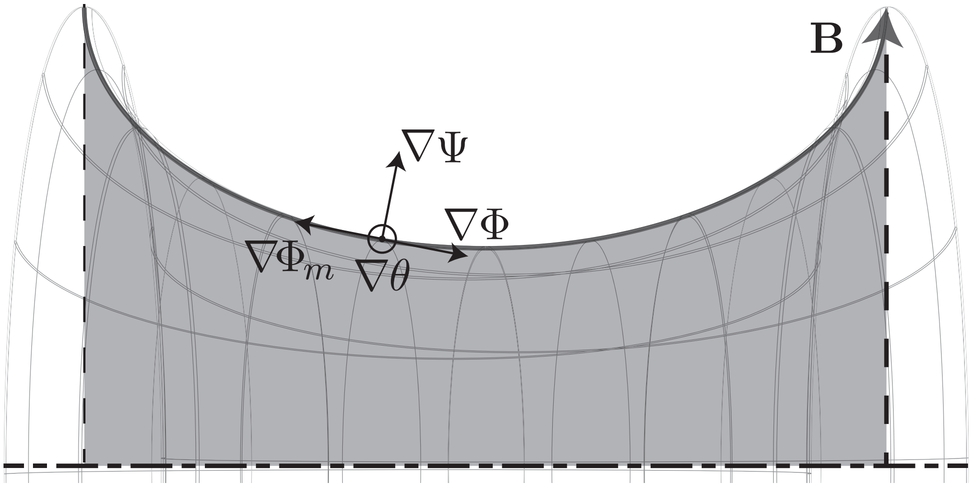

Figure 4.3: Orthonormal basis formed by the stream function, azimuthal angle, and the magnetic scalar potential. The sign of the magnetic scalar potential, $\nabla\Phi_m$, is reversed to form a right-handed coordinate system.

derivation of the coordinate system is given to conclude the chapter.

Stream Function Basis

The stream function coordinate represents the plasma motion perpendicular to the magnetic field. This acts as the primary coordinate, and represents the direction of impeded plasma motion in the magnetic field. As stated previously, the stream function value represents the magnetic flux through the enclosed surface. Here, the reference line, or zero contours, are the centerline of the domain as well as magnetic field lines that connect to the center of the magnet to the centerline.

Azimuthal Basis

The second coordinate is the azimuthal direction which is defined similarly to that of other curvilinear coordinate systems. Typically in an axisymmetric domain this direction can be ignored. While gradients in the azimuthal direction may indeed be neglected, in the case of plasmas various drifts in the azimuthal direction occur. Note that because of the axisymmetry assumed in the magnetic field, the azimuthal basis is orthogonal to the stream function and scalar potential bases.

Magnetic Scalar Potential Basis

There are several choices for the final basis vector. An acceptable choice would be the arc length of the magnetic field. This would have the convenience of having units of length and would eliminate the need for a scale factor; However, using arc length breaks the orthogonality of the coordinate system. A better option is to use the magnetic scalar potential. In fluid mechanics, the appropriate analog would be the velocity potential. This scalar field has constant contours that are everywhere orthogonal to the stream function contours, a property that maintains the orthogonal basis and eliminates the need for a reciprocal basis pair[48].

The magnetic scalar potential addresses the parallel motion of the plasma. It flows freely along the field lines compared to the perpendicular motion, with the exception of the magnetic reflection caused by the converging field lines described by Equation (4.4). In general, the scalar potential basis describes the plasma loss through the magnetic cusps. Magnetic reflection in this direction can be treated with the fluid description of plasmas as shown by Comfort[49]. The magnetic scalar potential is typically defined by Equation (4.5); however, the negative of this quantity is used here to maintain a right handed coordinate system.

$$m\dot{v}_{\parallel} = -\mu \nabla_{\parallel} B \tag{4.4}$$

$$-\nabla \Phi_m = \mathbf{B} = \nabla \Phi \tag{4.5}$$

The exact values do not have any direct physical meaning unlike with the stream function. In fact, the zero value is arbitrary just as in the case of gravitational and electrostatic potential. The reference values for the miniature discharge in Chapter 3 are taken to be the center of the outside magnets.

To summarize, the permanent magnet rings essentially act as a source and sink for the vector field. This field can be calculated using the equations given in Section 4.4.2. The vector field components are then used to solve the PDEs for the stream function and magnetic scalar potential. The two scalar quantities provide the bases for the magnetically field aligned coordinate system shown in Figure 4.3. The transformation from potential flow is further illustrated in Table 4.1 by displaying the corresponding units in the magnetic flux analogy. Differential operators are developed for the flux aligned coordinates (similar to cylindrical and spherical coordinates) in Section 4.6.2 allowing for the plasma behavior to be investigated in its natural coordinate system.

Table 4.1: Potential flow analogy for the magnetic flux aligned coordinates.

	Vector Field	Stokes Stream Function	Scalar Potential
Potential Flow	$\mathbf{v}\ \left(\frac{\text{m}}{\text{s}}\right)$	$\Psi\ \left(\frac{\text{m}^3}{\text{s rad}}\right)$	$\Phi\ \left(\frac{\text{m}^2}{\text{s}}\right)$
Magnetic Flux Coordinats	$\mathbf{B}$ (T)	$\Psi\ \left(\frac{\text{Tm}^2}{\text{rad}}\right)$	Φ (Tm)

4.4 Magnetic Field Formulae

In order to calculate the stream function and magnetic scalar potential fields, analytical formulae are needed for the permanent magnet configurations of interest. The following sections seek to introduce the analytical equations for rectangular and radially magnetized ring magnets. The block magnet serves as a good tool to develop intuition of how the magnet dimensions effect the magnet field behavior. Additionally, ion thrusters typically use a series of block magnets to construct ring-cusp configurations. This is done to account for the differences in thermal expansion between the magnetic material and the discharge chamber. The existence of a stream function, however, demands that there be at least one axis of symmetry, a requirement that is clearly broken by the use of individual block magnets. Because of these symmetry requirement, the block magnets used in the true configuration of the miniature discharge are approximated as radially magnetized ring magnets. A comparison is made between the two magnetic arrangements to quantify the error of the approximation.

4.4.1 Block Magnet

The equation for the block magnet can be derived by integrating the magnetization vector over the block magnet volume which is carried out by Engel-Herbert[50]. The analytical formula for the magnetic field is given in Equations (4.6), (4.7), and (4.8) for the block magnet illustrated in Figure 4.4. The field from individual block magnets can be superimposed to calculate the field configuration seen in the miniature discharge experiment. The largest deviations from the axisymmetric approximation occur on the meridian plane in between adjacent block magnets.

To calculate a B_x or B_y, use Equation (4.7) bu first calculating Pr for the x or y direction. Pr is calculated using the appropriate "[ ]" permutation for the x or y direction. The ± in the "[ ]" permutations correspond the right and left hand side. For example, $[- + -]_x$ would correspond to $(y + d) + L_B(-, +, -)$. This pattern is used for all the $\pm_s$ shorthand notations including the "$\langle\ \rangle$" terms

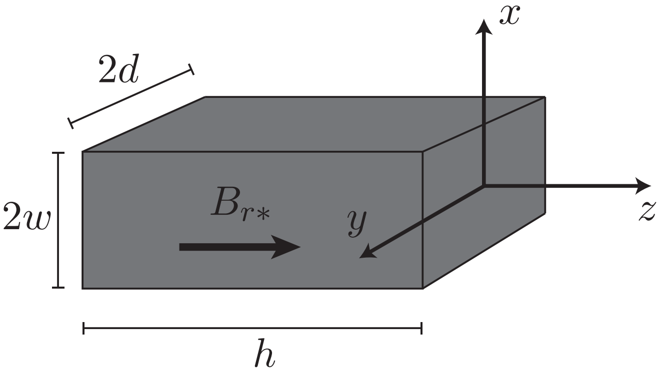

Figure 4.4: Definition for the block magnet dimensions. B_{r*}, the residual induction is a function of the magnetic material used and its treatment process assuming saturation.

used to find B_z.

$$L_B\left(\pm_1, \pm_2, \pm_3\right) = \sqrt{(x \pm_1 w)^2 + (y \pm_2 d)^2 + \left(\left[z + \frac{h}{2}\right] \pm_3 \frac{h}{2}\right)^2} \tag{4.6}$$

$$\begin{aligned}
\left[\pm_1, \pm_2, \pm_3\right]_x &= (y \pm_2 d) + L_B\left(\pm_1, \pm_2, \pm_3\right) \\
\left[\pm_1, \pm_2, \pm_3\right]_y &= (x \pm_1 w) + L_B\left(\pm_1, \pm_2, \pm_3\right) \\
Pr_{x,y} &= \frac{[- - -]_{x,y}\,[- + +]_{x,y}\,[+ - +]_{x,y}\,[+ + -]_{x,y}}{[+ + +]_{x,y}\,[+ - -]_{x,y}\,[- + -]_{x,y}\,[- - +]_{x,y}} \\
B_{x,y} &= \left(\frac{-B_{r*}}{4\pi}\right) ln\left[Pr_{x,y}\right]
\end{aligned} \tag{4.7}$$

$$\begin{aligned}
\langle \pm_1, \pm_2, \pm_3 \rangle &= tan^{-1}\left(\frac{(x \pm_1 w)(y \pm_2 d)}{\left(\left[z + \frac{h}{2}\right] \pm_3 \frac{h}{2}\right) L_B\left(\pm_1, \pm_2, \pm_3\right)}\right) \\
Pr_{z^+} &= \langle + + + \rangle + \langle + - - \rangle + \langle - + - \rangle + \langle - - + \rangle \\
Pr_{z^-} &= \langle - - - \rangle + \langle - + + \rangle + \langle + - + \rangle + \langle + + - \rangle \\
B_z &= \left(\frac{-B_{r*}}{4\pi}\right)\left[Pr_{z^+} - Pr_{z^-}\right]
\end{aligned} \tag{4.8}$$

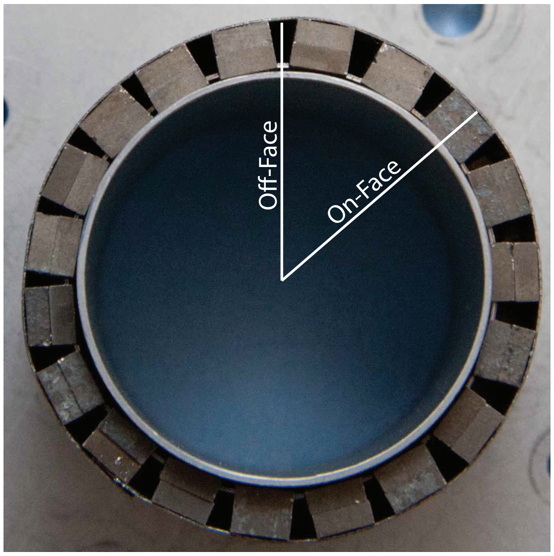

Figure 4.5: Measurement planes for "Off-face" and "On-face" regions in Figure 4.6. The image shown is of the strong magnet configuration.

4.4.1.1 Block Magnet Configuration

The magnetic field configurations for the miniature discharge are calculated along two meridian planes to capture the azimuthal change due to the discrete block magnets. The extremes are located on the plane normal to the magnet face, the "On-face" region, and the plane located in between two adjacent magnets within a ring, the "Off-face" region. This is shown in Figure 4.5 These fields are shown in Figure 4.6 for both the baseline and the strong magnet configurations. The plots show that the magnetic field is only slightly weaker in the "Off-face" locations. The local orientation of the field lines has a negligible shift between the two locations supporting the conclusion that the current configuration approaches the axisymmetric limit.

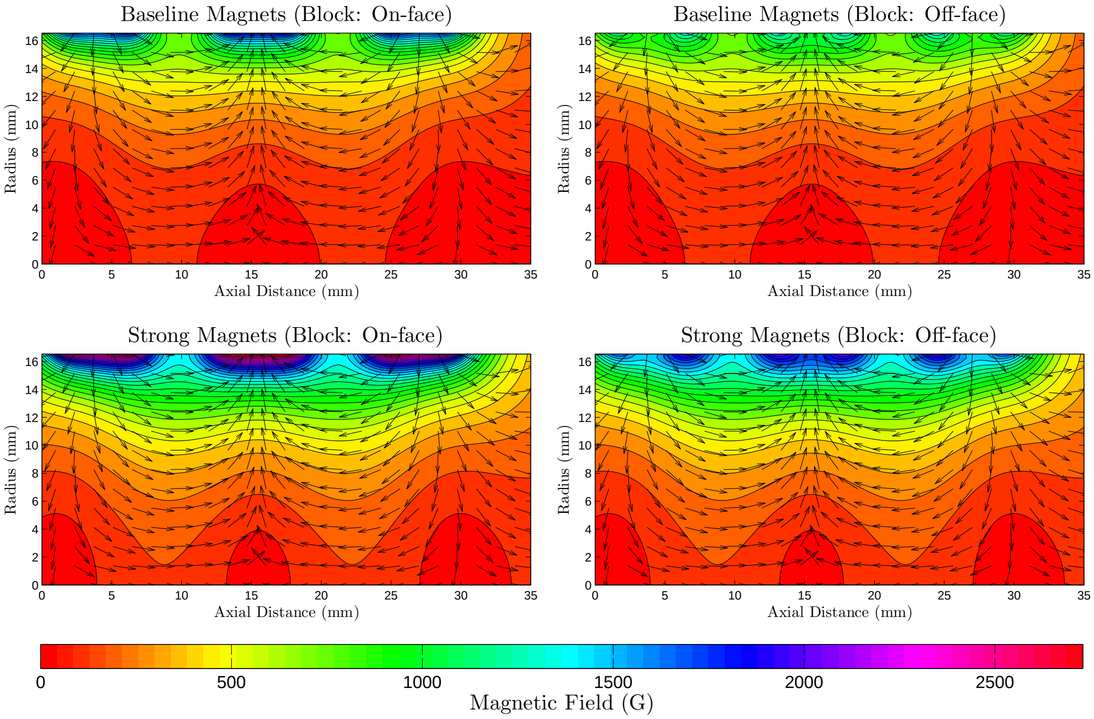

Figure 4.6: Block magnet calculations for the baseline and strong magnet configurations. The left plots represent the magnetic field on the plane normal to the magnet face while the right plots represent the plane between two adjacent magnets. Vectors are normalized and indicate field orientation at the arrow base.

4.4.2 Radially Magnetized Ring Magnet

The magnetic fields shown is Section 3.2 are calculated from Ravaud and Babic's analytical formula for a radially magnetized ring magnet[37, 38]. The analytical formulae are given in Equations (4.9) & (4.10). Here, $K(k_n^{\pm})$ and $\Pi(h^{\pm}, k_n^{\pm})$ are the complete elliptical integrals of the first and third kind respectively. Note that the surface magnetic pole density has been replaced by the residual induction expressed in Tesla. This calculation is based on the sum of the inner and outer surfaces' contribution to the magnetic field. The surfaces used are normal to the magnetic field alignment. Additionally, it is assumed that the magnetization, M, which is related to the residual induction, is constant for samarium cobalt[51]. This is a reasonable approximation due to the linearity of samarium cobalt's demagnetization curve[52].

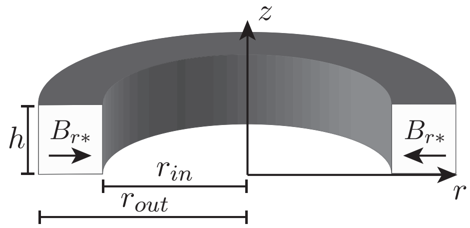

Figure 4.7: Ring magnet geometry and nomenclature.

$$\begin{aligned}
B_z^+(r,z) &= \frac{B_{r*}}{2\pi}\sum_{n=1}^{2}(-1)^{(n-1)}k_n^+\sqrt{\frac{r_{in}}{r}}K(k_n^+) \\
B_z^+(r,z) &= -\frac{B_{r*}}{4\pi}\sum_{n=1}^{2}(-1)^{(n-1)}k_n^-\sqrt{\frac{r_{out}}{r}}K(k_n^-) \\
B_z &= B_z^-(r,z) + B_z^+(r,z)
\end{aligned} \tag{4.9}$$

$$
\begin{aligned}
B_r^+(r,z) &= -\frac{B_{r*}}{4\pi}\sum_{n=1}^{2}(-1)^{(n-1)}\frac{t_n k_n^+}{r}\sqrt{\frac{r_{in}}{r}}\left[K(k_n^+) + \frac{r-r_{in}}{r+r_{in}}\Pi(h^+,k_n^+)\right] \\
B_r^-(r,z) &= \frac{B_{r*}}{4\pi}\sum_{n=1}^{2}(-1)^{(n-1)}\frac{t_n k_n^-}{r}\sqrt{\frac{r_{out}}{r}}\left[K(k_n^-) + \frac{r-r_{out}}{r+r_{out}}\Pi(h^-,k_n^-)\right] \qquad (4.10) \\
B_r(r,z) &= B_r^-(r,z) + B_r^+(r,z)
\end{aligned}
$$

where,

$$
\begin{aligned}
(k_n^+)^2 &= \frac{4rr_{in}}{(r+r_{in})^2+t_n^2} \qquad & h^+ &= \frac{4rr_{in}}{(r+r_{in})^2} \qquad & t_1 &= z-h \\
(k_n^-)^2 &= \frac{4rr_{out}}{(r+r_{out})^2+t_n^2} \qquad & h^- &= \frac{4rr_{out}}{(r+r_{out})^2} \qquad & t_2 &= z
\end{aligned}
$$

4.4.2.1 Ring Magnet Approximation

The calculations from Equations (4.8) & (4.10) can be seen in Figure 3.12 and are repeated in Figure 4.8. An alternative color plot is used where the extremes are associated with the red hue. This is to highlight the subtle variations in both the weak field region and the strong field region. Figure 4.8 and Figure 4.6 have been plotted using identical color scales. Additionally, the markings associated with the experimental data have been removed in favor of the magnitude contours and arrows indicating the local magnetic field.

Because of the field configuration, there will always exists null regions equal to the number of magnetic rings. The stronger magnetic field acts to penetrate the center of the chamber, isolating the null regions and shrinking the so-called "field-free" region. This is also seen in the block magnet configuration, but seems to slightly augmented in the ring magnet approximation. Ultimately, the ability to sustain the field-free region affects the volume utilization of the discharge.

4.4.2.2 Error in Axisymmetric Assumption

The block magnet configuration is compared to the ring magnet approximation to verify the assumption of axisymmetry. The relative error is taken with respect to the block magnet values. As seen in Figure 4.9, the relative error in a large portion of the chamber is within 5% with the largest error stemming from the null values along the centerline and should thus be ignored. The next largest regions of error are found at the cusps for the off-plane location. This is predictable due to the lack of magnetic material between block magnets. It is important to note that while the magnetic field strength in the off-face region departs from the axisymmetric case, the field orientation is largely unaffected.

4.4.3 Dimension Sensitivity: One-Dimensional study

Much can be gleaned from the one-dimensional analysis of a single block magnet. By examining the effects of changing the various magnet parameters on the on-axis field strength, intuition can be developed regarding how to manipulate the field configuration in various ways. This understanding is useful in determining the magnetic field configuration of future miniature discharge designs which is considered in Chapter 6. The following analysis is conducted by limiting Equation (4.8) to the $(x = 0, y = 0, z)$ axis. An equivalent formulation is given in Equation (4.11)[53].

$$\mathbf{B} = \frac{B_{r*}}{\pi}\left[tan^{-1}\left(\frac{z+h}{dw}\sqrt{d^2+w^2+(z+h)^2}\right) - tan^{-1}\left(\frac{z}{dw}\sqrt{d^2+w^2+z^2}\right)\right] \tag{4.11}$$

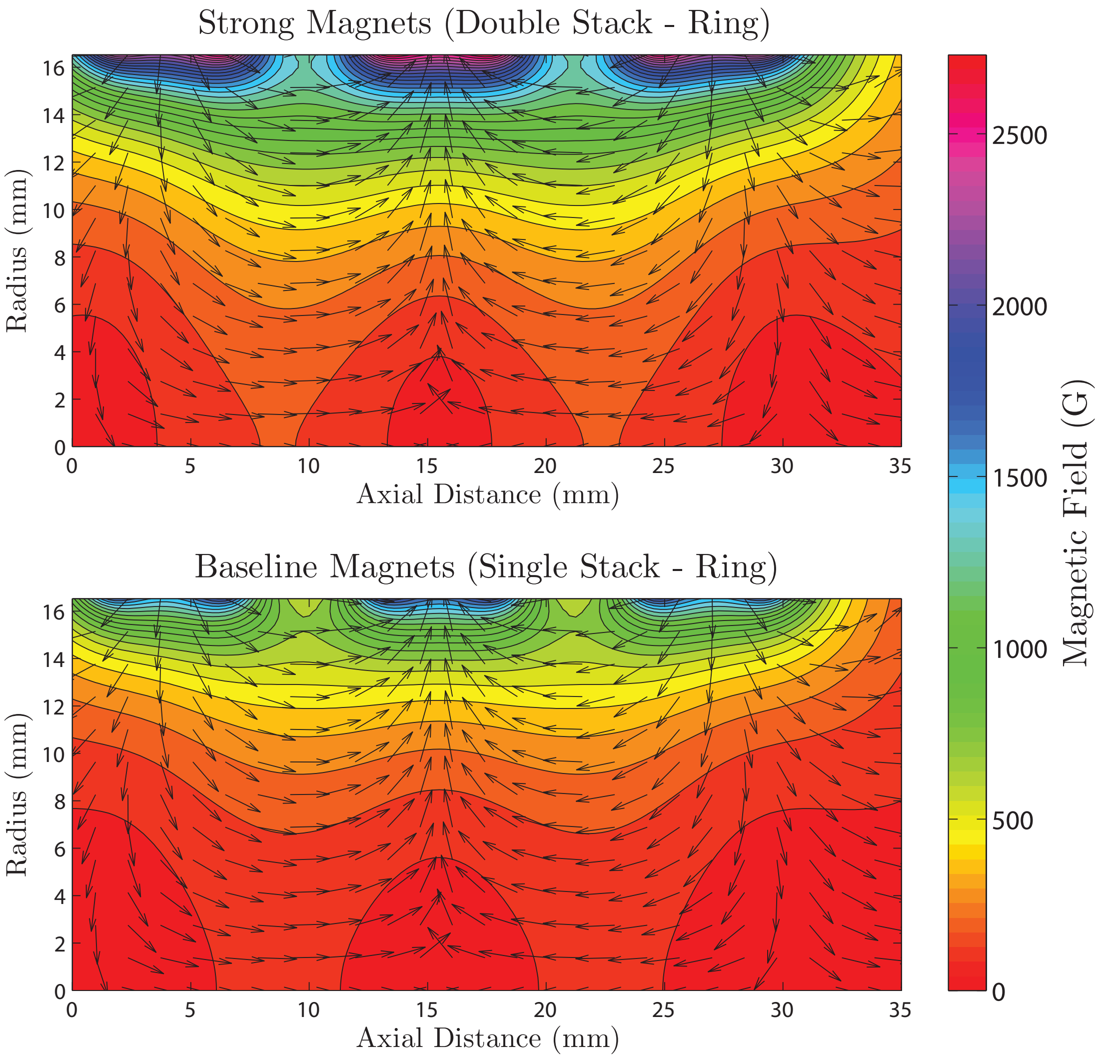

Figure 4.8: Analytical magnetic field calculations for the ring magnet approximation as seen in Figure 3.12 without the experimental overlays. Vectors are normalized and indicate field orientation at the arrow base. Magnet dimensions and locations can be found in Figure 3.11.

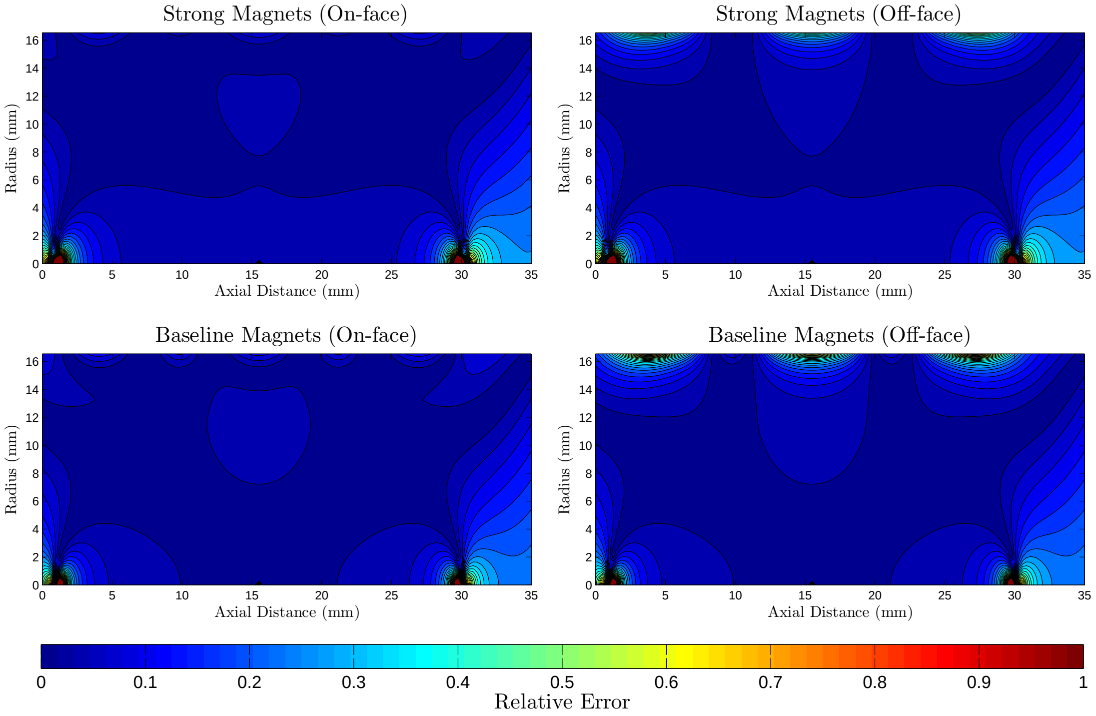

Figure 4.9: Error associated with axisymmetric approximation. Large errors on the centerline are caused by null magnetic field values and should be ignored. Largest discrepancy occurs at the magnet locations of the off-face plane as expected.

Field Strength Effect

By increasing the magnetization or residual induction of the material, each magnetic dipole within the material produces a larger field strength and acts to bolster the entire field. Figure 4.10 shows the effect of successively larger values of the residual induction, B_{r*}. Because of the r^3 drop-off, this effect is limited to the near field region; however, there does not appear to be an asymptotic limit to the field strength.

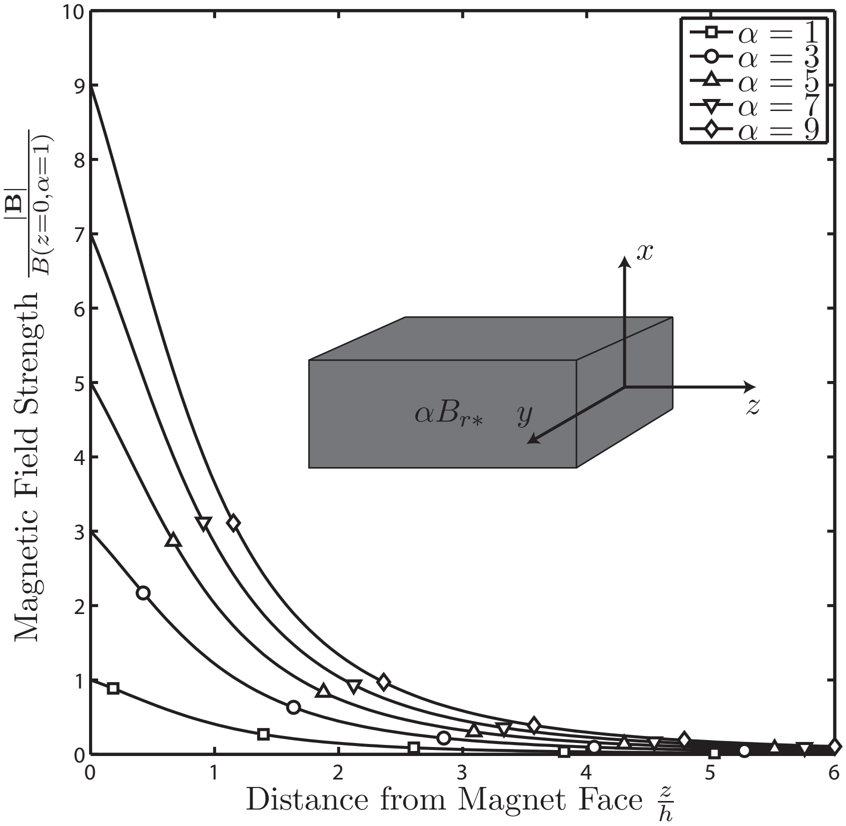

Figure 4.10: Effect of increasing the residual induction. Because the residual induction is a material property, the limitation of this effect is based on the availability of high B_{r*} materials.

Predictably, at $z = 0$, the gain of the magnetic field is equivalent to α, the multiplicative constant of the residual induction. In this way, the near-field effect of various residual inductions can be predicted. Physically, changing the residual induction requires changing the permanent magnet material. Because of this, the limitation on B_{r*} lies in the availability of materials. This can be achieved with the use of electromagnets, however, this is not commonly done in ring-cusp ion thruster discharges due to the additional power required. Additionally, as seen in Chapter 3, a stronger field is not always better for thruster performance.

Magnetization Height Effect

Figure 4.11 shows an asymptotic limit as the permanent magnet is increased along the magnetization dimension. This is due to the drop-off of field strength from the rear sections on the region directly in front of the magnet. In all of the cases seen in Section 4.4.3, the $\alpha = 1$ base magnet is a single block magnet used in Chapter 3. Figure 4.11 shows that doubling the magnet height is within the asymptotic limit. As can be seen by the $\alpha = 1$ and $\alpha = 3$ curves, an increase in height in this region has a similar effect to increasing the residual induction . Ultimately, altering this dimension has the effect of increasing the field strength near the cusp to a limit while leaving the far-field region relatively untouched.

Width Effect

Increasing the permanent magnet along the dimension transverse to the magnetization vector acts to decrease the field on the face while increasing the magnetic field further into the discharge chamber. This is due to the outer dipoles field opposing the center region on axis. In contrast, the outer dipoles have a field orientation constructive with the field emanating from the center region in the far-field region. Similar to the “Height Effect”, this effect approaches a limit with increasing α. From Chapter 3, it was shown that a field-free region is still fairly

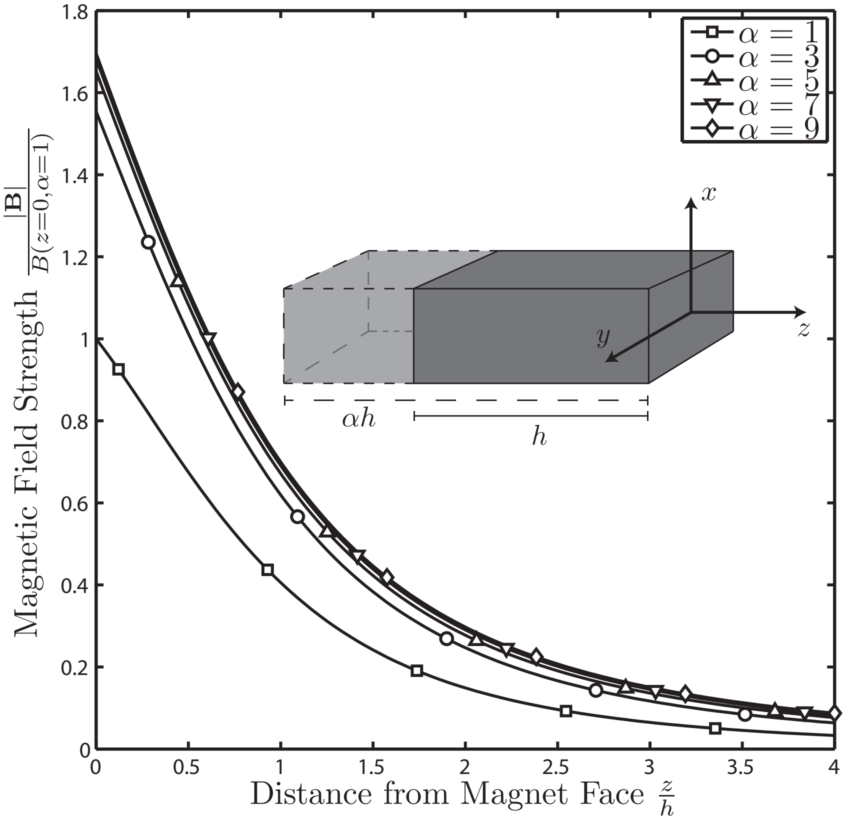

Figure 4.11: Effect of increasing the dimension along the magnetization vector. Material toward the rear of the block has a decreasing effect thus limiting the α value. Change in height acts to increase the near field region while leaving the far-field region relatively unaffected.

important for discharge performance. Therefore, increasing the field in the center of the discharge chamber is not a desirable effect and is taken into consideration for miniature discharge design.

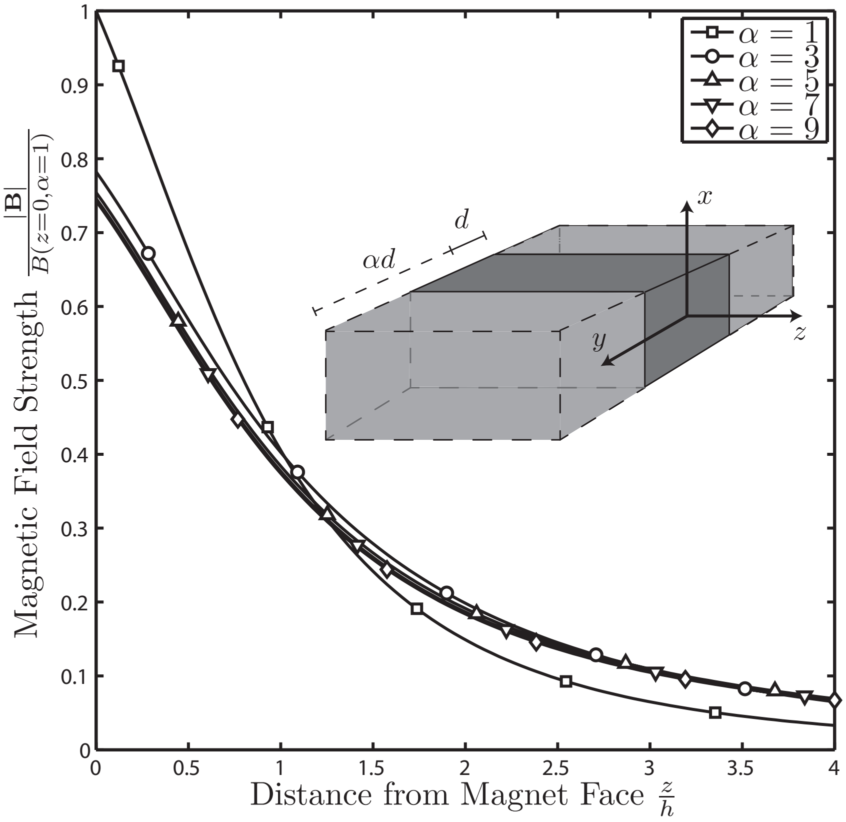

Figure 4.12: Effect of increasing the dimension transverse to the magnetization vector. The outer edges of the magnet act to suppress the on axis field in the near-field region while increasing the field in the far-field region. This manipulation allows for the magnetic field to penetrate further into to discharge volume. Like Figure 4.11, the on-axis profile asymptotes with increasing α.

4.5 Numerical Calculation of the Stream Function and the Scalar Potential

The stream function and magnetic potential are dependent on the magnetic field configuration. In general, an analytical solution cannot be found so these properties must be solved numerically. Both of the partial differential equations for the stream function and scalar potential can be reduced to a Poisson equation with Neumann boundary conditions. This is discretized with a finite difference method[54, 55].

The numerical solution provides the transformation from cylindrical coordinates to the stream function and the scalar potential, the complete domain is in general not onto. Because of this, the transformation is not invertible[47]. In larger magnetic field configurations, it may be necessary to divide the domain into sub-domains that are locally onto. In ring-cusp configurations, each magnetic ring has a corresponding null streamline. If there are adjacent counter-polarized rings, the null streamlines enclose a region with the chamber boundary. In general, a sub-domain consisting of two such regions is onto, and thus has an invertible transformation with cylindrical coordinates. In the current configuration these two regions are encapsulated by the three ring magnets.

4.5.1 Stream Function Formulation

The partial differential equation is given by Equation (4.2). The first-order system can be combined by taking the divergence of the gradient of the stream function. This is seen in Equation (4.13) where a short hand notation is defined by Equation (4.12). The result is a Poisson equation

$$g_r = rB_z \ ; \ g_z = -rB_r \tag{4.12}$$

$$\begin{aligned} \nabla \cdot \nabla\Psi &= \nabla \cdot \left(g_r\hat{\mathbf{r}} + g_z\hat{\mathbf{z}}\right) \\ \nabla^2\Psi &= \frac{1}{r}\frac{\partial}{\partial r}\left(rg_r\right) + \frac{\partial}{\partial z}\left(g_z\right) \end{aligned} \tag{4.13}$$

Poisson's equation for the stream function has mixed boundary conditions. By definition, the magnetic flux through the centerline is zero, thus the $r = 0$ boundary can be expressed with Equation (4.14). The other boundary conditions can be derived from the original partial differential equation as outlined in Equations (4.15).

$$\Psi(0, z) = 0 \tag{4.14}$$

$$\frac{\partial\Psi}{\partial n} = \frac{\partial\Psi}{\partial r} = g_r(r = R, z) \quad ; \quad \frac{\partial\Psi}{\partial n} = \frac{\partial\Psi}{\partial z} = g_z(r, z = (0; L)) \tag{4.15}$$

4.5.2 Scalar Potential Formulation

Before the calculation of the scalar potential, the existence of such a function must be verified for the system. In order for a velocity potential to exist in fluid mechanics, the velocity field must be irrotational[44] as prescribed by Equation (4.16).

$$\nabla \times \mathbf{v} = 0 \tag{4.16}$$

By replacing the velocity field with the magnetic field and comparing it to Ampere's law, Equation (4.17), it can be seen that a scalar potential exists in the absence of external currents as well as time changing electric fields. Because of these strict requirements, the utility of the magnetic scalar potential is usually limited to deriving the field of permanent magnets. Although there exists charge carriers in the plasma, the density is assumed to be low enough such that the field is unaffected. Additionally, the DC discharge in ion thrusters operate with little to no oscillations in the plasma.

$$\nabla \times \mathbf{B} = \mu_0 \mathbf{J} + \mu_0 \epsilon_0 \frac{\partial \mathbf{E}}{\partial t} \approx 0 \tag{4.17}$$

The PDE for the scalar potential is derived in a similar fashion to the stream function; however, taking the divergence of Equation (4.5) yields a homogeneous right hand side by applying Equation (4.1). The result is

$$\begin{aligned} \nabla \cdot \nabla \Phi &= \nabla \cdot (B_r \hat{\mathbf{r}} + B_z \hat{\mathbf{z}}) \\ \nabla^2 \Phi &= 0 \end{aligned} \tag{4.18}$$

Because the reference value of the potential can be arbitrarily prescribed, Laplace's equation for the scalar potential is given the Neumann boundary conditions stated in Equation (4.19) which is based on the definition of the scalar potential.

$$\frac{\partial \Phi}{\partial n} = \frac{\partial \Phi}{\partial r} = B_r(r = (0; R), z) \quad ; \quad \frac{\partial \Phi}{\partial n} = \frac{\partial \Phi}{\partial z} = B_z(r, z = (0; L)) \tag{4.19}$$

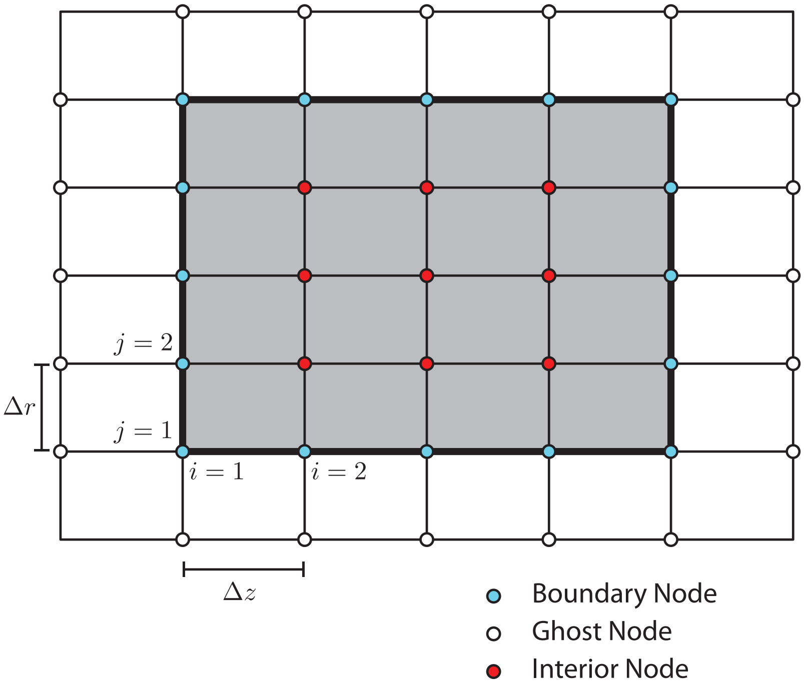

Figure 4.13: Discretization of the cylindrical domain. The physical boundary is outlined with the weighted black line.

4.5.3 Numerical Method

The solution to Equations (4.18) & (4.13) are found by using a finite difference method on a rectilinear discretization of the cylindrical domain similar to Figure 4.13. Here the distinction for various node points are color-coded. The interior nodes are shown in red. The boundary and ghost nodes, blue and white respectively, are used to treat the Neumann boundary conditions.

After a grid resolution is chosen, the magnetic field is calculated on the node points using the equations given in Section 4.4.2. Next, the Laplacian is approximated using a five-point stencil such as that shown in Figure 4.14. This method is chosen for the simple structure as well as for its second-order accuracy. The approximation of the Laplacian can be found through a Taylor expansion, the results of which are given in Equation (4.20). The first partial in the radial

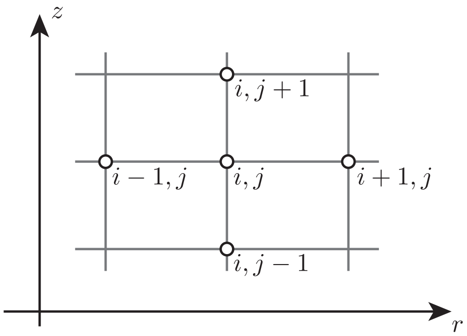

Figure 4.14: Stencil used to approximate the derivatives.

direction has been replaced with the component of the gradient. Here the approximation is given for the scalar potential, however, the stream function takes on an identical form with the substitution of Ψ for Φ and g_r for B_r. The scalar potential is homogeneous and thus does not require discretization of the right hand side. For the stream function, Equation (4.13) is approximated using a central differencing scheme given in Equation (4.21).

$$\begin{aligned}\nabla^2\Phi &= \frac{\partial^2\Phi}{\partial r^2} + \frac{\partial^2\Phi}{\partial z^2} + \frac{1}{r}\frac{\partial\Phi}{\partial r} = \frac{\partial^2\Phi}{\partial r^2} + \frac{\partial^2\Phi}{\partial z^2} + \frac{B_r}{r} \\ &\approx \frac{\Phi_{i+1,j} - 2\Phi_{i,j} + \Phi_{i-1,j}}{\Delta z^2} + \frac{\Phi_{i,j+1} - 2\Phi_{i,j} + \Phi_{i,j-1}}{\Delta r^2} + \frac{B_{r(i,j)}}{r_{i,j}}\end{aligned} \tag{4.20}$$

$$\begin{aligned}\nabla\cdot\mathbf{g} &= \frac{1}{r}\frac{\partial}{\partial r}(rg_r) + \frac{\partial}{\partial z}(g_z) = \frac{\partial g_z}{\partial z} + \frac{\partial g_r}{\partial r} + \frac{g_r}{r} \\ &\approx \frac{g_{z(i+1,j)} - g_{z(i-1,j)}}{2\Delta z} + \frac{g_{r(i,j+1)} - g_{r(i,j-1)}}{2\Delta r} + \frac{g_{r(i,j)}}{r_{i,j}}\end{aligned} \tag{4.21}$$

The Neumann boundary conditions are treated similarly with Equation (4.20); however, ghost node values of (i, j), those that occur outside of the boundary, are solved for by discretizing Equations (4.19) & (4.15). Using a second-order method given in Equations (4.22) through (4.25), the ghost node values can be solved as a function of interior and boundary nodes. Here, N_i & N_j are the total number of nodes in the z and r direction respectively. The Dirichlet boundary condition for the stream function, Equation (4.14), is explicitly prescribed.

$$\begin{aligned} \frac{\partial \Phi}{\partial n} = \frac{\partial \Phi}{\partial r} = \frac{\Phi_{i,N_j+1} - \Phi_{i,N_j-1}}{2\Delta r} &= B_{r(i,N_j)} \\ \Phi_{i,N_j+1} = 2\Delta r B_{r(i,N_j)} + \Phi_{i,N_j-1} \end{aligned} \tag{4.22}$$

$$\begin{aligned} \frac{\partial \Phi}{\partial n} = \frac{\partial \Phi}{\partial z} = \frac{\Phi_{N_i+1,j} - \Phi_{N_i-1,j}}{2\Delta z} &= B_{r(N_i,j)} \\ \Phi_{N_i+1,j} = 2\Delta z B_{z(N_i,j)} + \Phi_{N_i-1,j} \end{aligned} \tag{4.23}$$

$$\begin{aligned} \frac{\partial \Phi}{\partial n} = \frac{\partial \Phi}{\partial r} = \frac{\Phi_{i,j=2} - \Phi_{i,j=-1}}{2\Delta r} &= B_{r(i,j=1)} \\ \Phi_{i,j=-1} = -2\Delta r B_{r(i,j=1)} + \Phi_{i,j=2} \end{aligned} \tag{4.24}$$

$$\begin{aligned} \frac{\partial \Phi}{\partial n} = \frac{\partial \Phi}{\partial z} = \frac{\Phi_{i=2,j} - \Phi_{i=-1,j}}{2\Delta z} &= B_{z(i=1,j)} \\ \Phi_{i=-1,j} = -2\Delta z B_{z(i=1,j)} + \Phi_{i=2,j} \end{aligned} \tag{4.25}$$

The interior equations with the boundary conditions combined create a $N_i \times N_j$ linear system. The result is a banded tridiagonal matrix on the LHS. As an example, for $\Delta r = \Delta z = 1$ and a 3x3 grid, the resulting matrix is,

$$\begin{pmatrix} -4 & 2 & 0 & 2 & 0 & 0 & 0 & 0 & 0 \\ 1 & -4 & 1 & 0 & 2 & 0 & 0 & 0 & 0 \\ 0 & 2 & -4 & 0 & 0 & 2 & 0 & 0 & 0 \\ 1 & 0 & 0 & -4 & 2 & 0 & 1 & 0 & 0 \\ 0 & 1 & 0 & 1 & -4 & 1 & 0 & 1 & 0 \\ 0 & 0 & 1 & 0 & 2 & -4 & 0 & 0 & 1 \\ 0 & 0 & 0 & 2 & 0 & 0 & -4 & 2 & 0 \\ 0 & 0 & 0 & 0 & 2 & 0 & 1 & -4 & 1 \\ 0 & 0 & 0 & 0 & 0 & 2 & 0 & 2 & -4 \end{pmatrix}$$

which can be solved using standard matrix inversion techniques. Because of the relatively fine grid needed to capture the cusp region, sparse matrix methods are recommended. For the current study, MATLAB's sparse matrix structure was used in conjunction with the standard matrix inversion operator, "/", which choose the best solution method given the matrix structure. The resolution used to calculate all stream functions and scalar potentials in this study is $N_i \times N_j = 393 \times 543$.

4.5.4 Solution

The numerical solution to the stream function and the scalar potential are presented for the baseline miniature discharge shown in Chapter 3. Figures 4.15, 4.16, and 4.17 give both solutions in detail along with the composite grid overlaid on the magnetic field strength. The following figures are for the baseline magnetic field configuration. In Figure 4.15, the sign of the stream function value simply indicates that the direction of the magnetic field. In order to satisfy the onto condition for an invertible transformation, the domain is limited to the region between the center of the outside rings. The origin is also relocated to the center ring. Note that in general the stream function and scalar potential can be calculated for the entire domain. Only when the transformation between coordinates requires the sub-domain treatment.

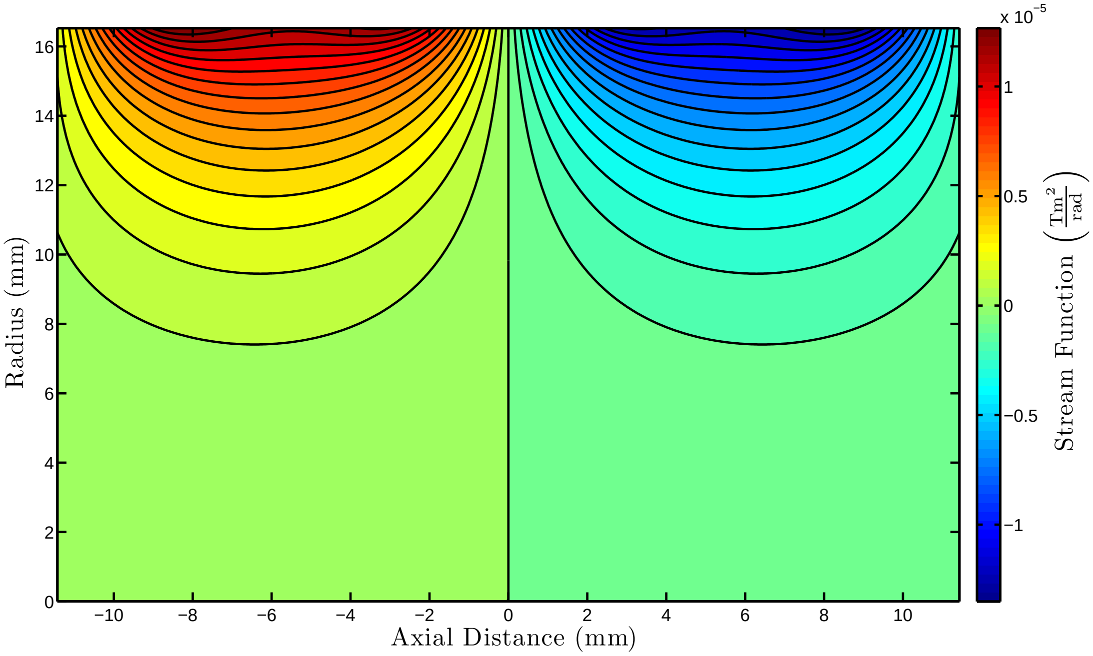

Figure 4.15: Stream Function Solution.

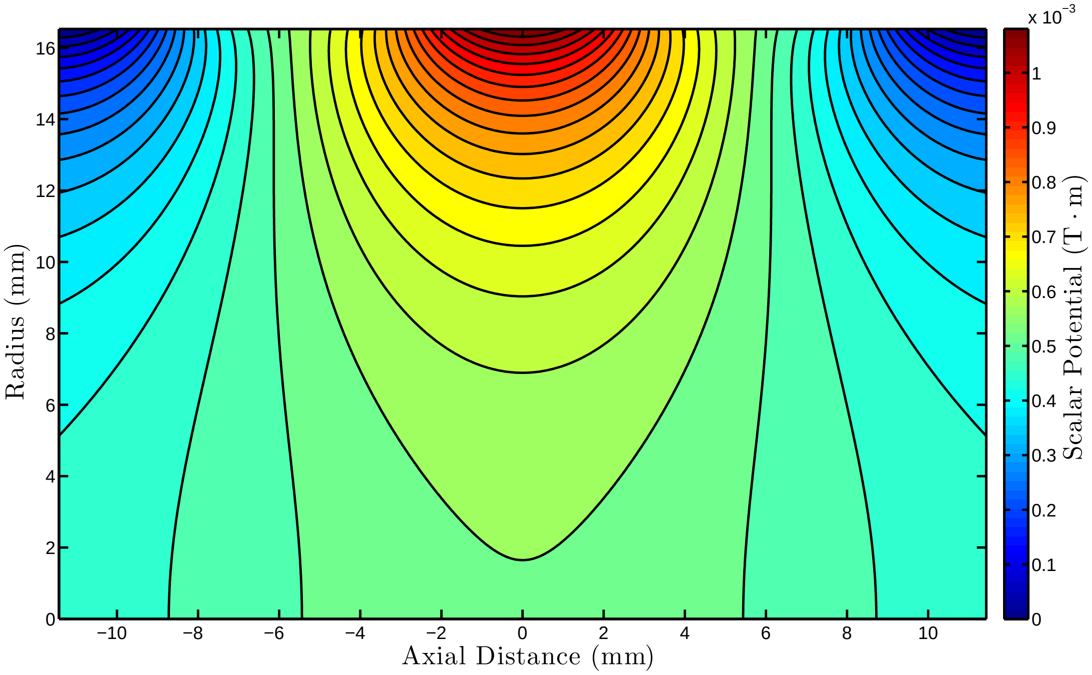

Figure 4.16: Scalar Potential Solution.

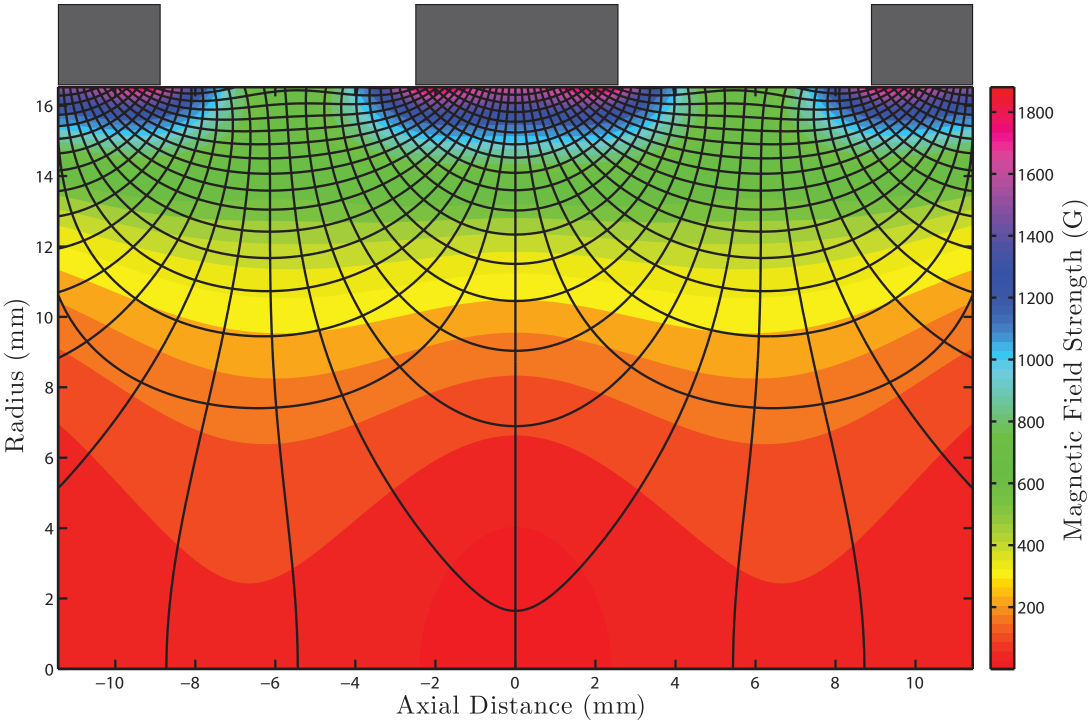

Figure 4.17: Equipotential and stream function contours superimposed on the magnetic field strength.

4.6 Flux Aligned Curvilinear Coordinates

Solving for the stream functions and scalar potentials automatically yields the transformations. This section shows the mapping between the domains followed by the derivation of the coordinate scale factors, the vector operators, and differential elements. Although the scale factors were ultimately not used in the current effort, they are derived here for posterity. The flux aligned coordinate system represents a physical interpretation of the plasma behavior due to its dependence on the magnetic field.

4.6.1 Cylindrical Coordinate Mapping

The solutions for the stream function and the scalar potential found in Section 4.5.4 are used for the mapping. The transformation exists only because of the truncation of the domain. This is done such that there is a one to one mapping between the flux coordinate system and the cylindrical domain. This mapping is shown in Figures 4.18 & 4.19. The vertical pairs demonstrate the mapping of constant contours of one coordinate system to the other. The first pair in Figure 4.18, shows constant radial and axial contours mapped on to the cylindrical and the flux coordinate domains. The same is done for the stream function contours and equipotential lines in Figure 4.19. The spacing chosen for the Figure 4.18 is a mm^2. The contours plotted in Figure 4.19 are also equally spaced, but the spacing chosen is arbitrary.

To clarify the domain transformation in flux coordinates, markers have been placed that translate the cylindrical coordinate locations to the flux coordinate domain. The centerline folds about the green marker such that the edges of the centerline, identified by a white marker and and “x” are coincident. Thus, the

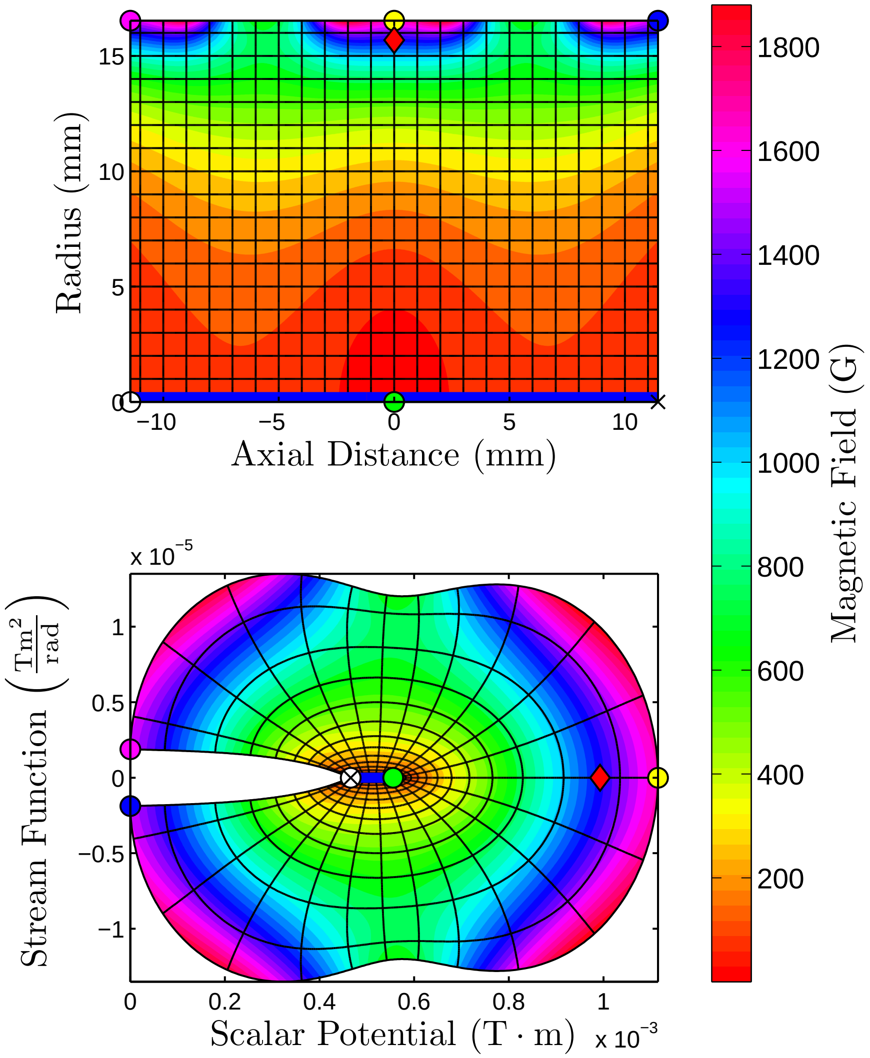

Figure 4.18: Transformation from cylindrical to flux aligned coordinates with the constant contours of the cylindrical components. Markers placed on the boundary are provided to help clarify the mapping.

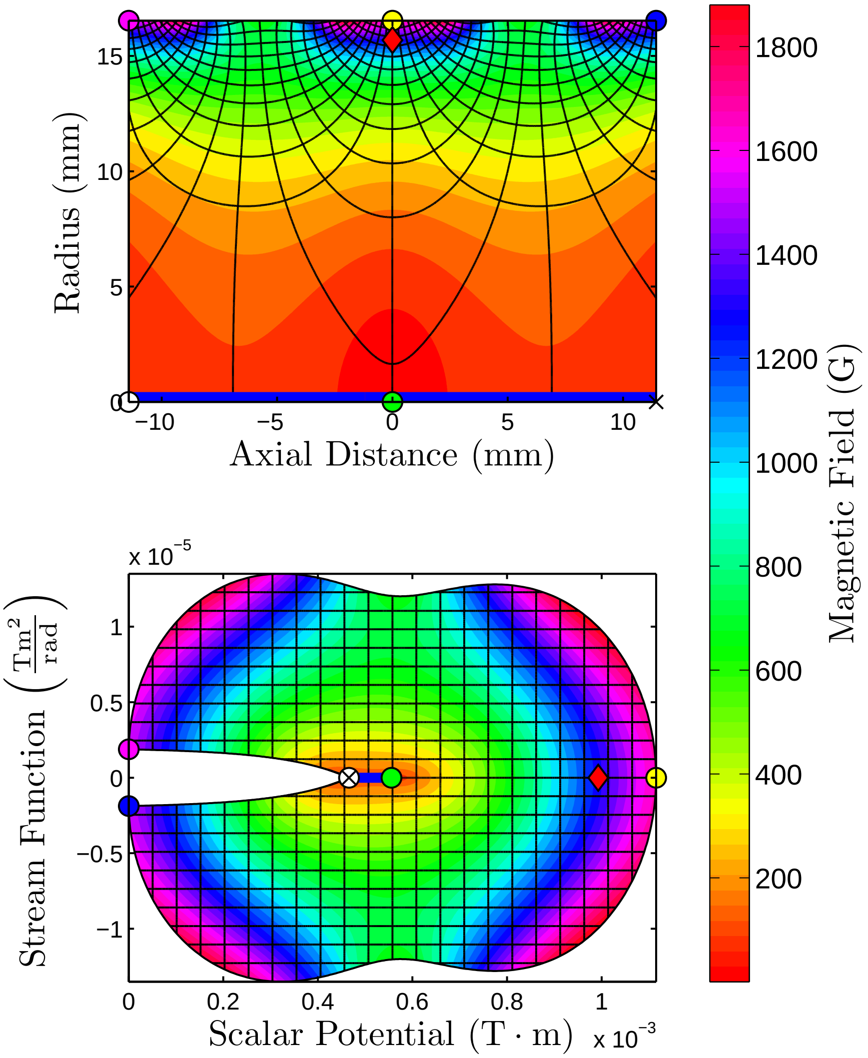

Figure 4.19: Transformation flux aligned to cylindrical coordinates with the constant contours of the flux aligned components. Markers placed on the boundary are provided to help clarify the mapping.

center line is not onto. Because this occurs at a boundary, this region must be treated with special consideration during analysis. The centerline should have a reflective boundary condition. In the flux coordinate system, this would be an interior boundary condition that must be enforced. The red diamond marker demonstrates how the flux coordinate system gives more resolution to the regions of higher magnetic field strength, a quality that is often needed in the analysis of cusped fields.

4.6.2 Scale Factors

As with any curvilinear coordinate system, scale factors must be found for the flux aligned coordinates in order to perform any calculus operations. As stated previously, the choice of the scalar potential for the coordinate along the field line forms an orthogonal coordinate system. Because of this, the covariant and contravariant components are identical and the bases have a relationship given by Equation (4.26)[48], where h_i is the scale factor and is expressed as the inverse magnitude of the gradient.

$$h_i \nabla r_i = \frac{\nabla r_i}{|\nabla r_i|} = \mathbf{\hat{e}_i} \tag{4.26}$$

Equations (4.5) & (4.2) give the gradients for the stream function and the scalar potential, but the gradient for the azimuthal coordinate has not been formally stated. From Clebsch coordinates, the magnetic field must follow Equation (4.27)[47]. For Equation (4.27) to be satisfied, $(\nabla\theta)_r$ and $(\nabla\theta)_z$ must equal zero and $(\nabla\theta)_\theta = \frac{1}{r}$. As expected this value is the same as in cylindrical coordinates. The scale factors for the remaining coordinates can be found by applying Equation (4.26) to Equations (4.5) & (4.2). The full set of scale factors is given in Equation (4.28). These scale factors can be used to derive the vector operators which are summarized in Table 4.2. Additionally, the scale factors can be used the generate differential elements, such as the differential volume given in (4.33). A schematic of the differential area is shown in Figure 4.20. Here an element of constant “area” in flux coordinates is shown in the cylindrical domain. The elements physical area scales inversely with the magnetic field strength.

$$\begin{aligned} \mathbf{B} &= \nabla\Psi \times \nabla\theta = B_r\hat{\mathbf{r}} + B_z\hat{\mathbf{z}} \\ &= rB_r\left(\nabla\theta\right)_\theta \hat{\mathbf{r}} + r\left(B_r\left(\nabla\theta\right)_r - B_z\left(\nabla\theta\right)_z\right)\hat{\boldsymbol{\theta}} + rB_z\left(\nabla\theta\right)_\theta \hat{\mathbf{z}} \end{aligned} \tag{4.27}$$

$$\begin{aligned} h_\Psi &= \frac{1}{|\nabla\Psi|} = \frac{1}{rB} \\ h_\theta &= \frac{1}{|\nabla\theta|} = r \\ h_\Phi &= \frac{1}{|\nabla\Phi|} = \frac{1}{B} \end{aligned} \tag{4.28}$$

Table 4.2: Vector operators in flux aligned coordinates.

$$\nabla\Xi = (rB)\frac{\partial\Xi}{\partial\Psi}\hat{\mathbf{e}}_{\boldsymbol{\Psi}} + \left(\frac{1}{r}\right)\frac{\partial\Xi}{\partial\theta}\hat{\mathbf{e}}_\theta + (B)\frac{\partial\Xi}{\partial\Phi}\hat{\mathbf{e}}_{\boldsymbol{\Phi}} \tag{4.29}$$

$$\nabla\cdot\mathbf{a} = \left(B^2\right)\left[\frac{\partial}{\partial\Psi}\left(\frac{r}{B}a_\Psi\right) + \frac{\partial}{\partial\theta}\left(\frac{1}{rB^2}a_\theta\right) + \frac{\partial}{\partial\Phi}\left(\frac{1}{B}a_\Phi\right)\right] \tag{4.30}$$

$$\nabla\times\mathbf{a} = \left(B^2\right)\begin{vmatrix} \frac{1}{rB}\hat{\mathbf{e}}_{\boldsymbol{\Psi}} & r\hat{\mathbf{e}}_\theta & \frac{1}{B}\hat{\mathbf{e}}_{\boldsymbol{\Phi}} \\ \frac{\partial}{\partial\Psi} & \frac{\partial}{\partial\theta} & \frac{\partial}{\partial\Phi} \\ \frac{1}{rB}a_\Psi & ra_\theta & \frac{1}{B}a_\Phi \end{vmatrix} \tag{4.31}$$

$$\nabla^2\Xi = \left(B^2\right)\left[\frac{\partial}{\partial\Psi}\left(r^2\frac{\partial\Xi}{\partial\Psi}\right) + \frac{\partial}{\partial\theta}\left(\frac{1}{r^2B^2}\frac{\partial\Xi}{\partial\theta}\right) + \frac{\partial}{\partial\Phi}\left(\frac{\partial\Xi}{\partial\Phi}\right)\right] \tag{4.32}$$

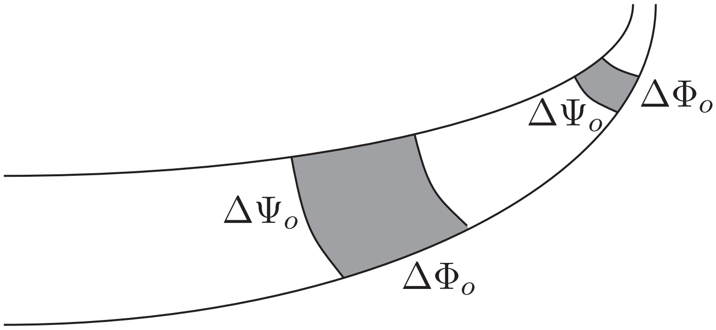

Figure 4.20: Schematic illustrating how a constant area in flux coordinates scales inversely with the magnetic field strength.

$$\mathrm{d}^3R = h_1h_2h_3\mathrm{d}u_1\mathrm{d}u_2\mathrm{d}u_3\frac{1}{B^2}\mathrm{d}\Psi\mathrm{d}\theta\mathrm{d}\Phi \tag{4.33}$$

4.7 Magnetic Field Analysis Summary

The preceding chapter has developed a framework to analyze the magnetic field's effect on plasma behavior. The flux aligned coordinate system is introduced as a way to decouple the plasma motion. This requires an axisymmetric approximation for the block magnets used in the miniature discharge experiment. A comparison of the magnetic field strength between the actual and approximated ring magnet configurations show reasonable agreement. Investigating the 1-D axial field of a block magnet revealed rules of thumb for chamber design. Ultimately, the field was used to numerically calculate the coordinate mapping to the magnetically aligned coordinate system. Along with decoupling the plasma motion, the new coordinate system gives more resolution to regions of higher magnetic field. Although not used in this study, the scale factors and differential elements developed should allow for a more detailed analysis of cusped configurations using the fluid equations.

CHAPTER 5

Bulk Plasma Structure due to Magnetic Cusp Confinement

The flux aligned coordinate system developed in Chapter 4 serves as a natural way to analyze the plasma structure within the magnetic cusp. The primary difficulty in analyzing the miniature discharges is the non-uniformity within the plasma discharge. The following chapter examines the plasma density profiles within the magnetic field to find a relationship for an arbitrary magnetic field configuration. This dependence allows for a prediction of the plasma density topography and is used to develop a miniature discharge design model in Chapter 6.

5.1 Measurement Domain in Flux Aligned Coordinates

Figure 5.1 shows the measurement domain overlaid onto the entire chamber domain. Because the flux aligned coordinate amplifies region of high magnetic field the measurement domain does not not appear to be sufficient in describing the plasma behavior within the magnetic cusps; however, Figures 3.14 & 3.15 show that the plasma density has been reduced to less than 10% of its maximum value in the majority of the measurement boundary. This occurs mainly between the magnetic cusps. At the magnetic cusp, the plasma is expected to stream freely to the walls[56]. Therefore, it is assumed that the measurement domain provides

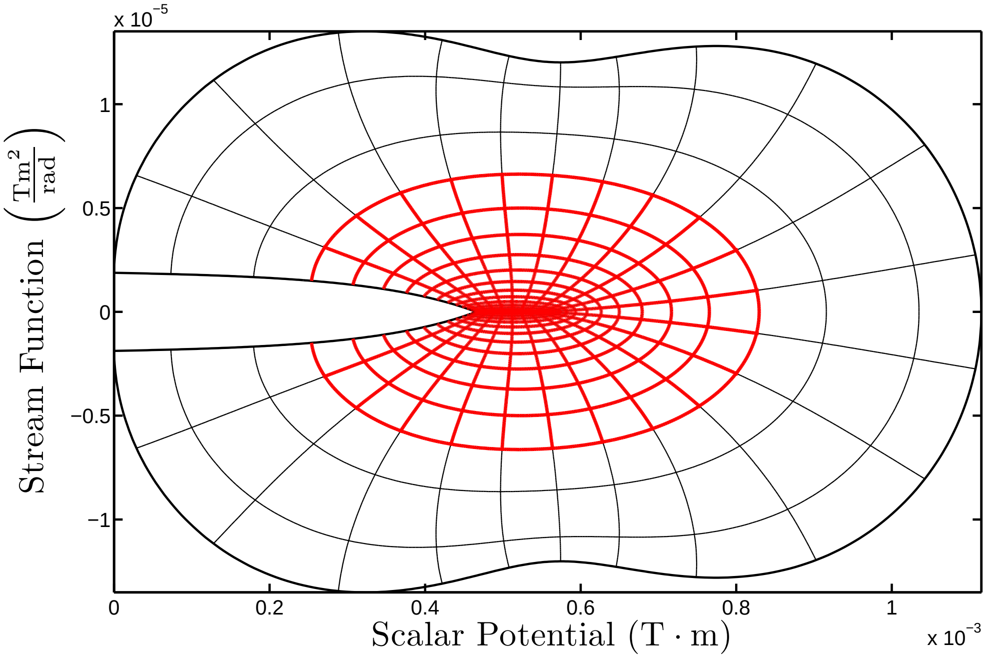

Figure 5.1: The measurement domain is shown in red superimposed on the total domain of the discharge chamber. The spacing of the contours shown is 1 mm × 1 mm.

sufficient information to infer the 2.5 mm of the unresolved domain. As discussed in Chapter 3, the region adjacent to the anode wall is not resolved due to the size of the probe.

In contrast, the high density region, or the centerline in cylindrical coordinates, has been reduced to a very small section in the flux aligned coordinate system. This low-field region includes the majority of the ion production, and the hollow cathode influence, as seen in Figure 3.20. By converting to the flux aligned coordinate system, this region becomes essentially a point source, a paradigm which decouples the plasma generation in the unmagnetized region from the plasma transport to the walls through the magnetized region.

5.2 Plasma Density Dependence on Stream Function

The plasma behavior is strongly coupled to the magnetic field lines. Figure 5.2 shows the direct mapping of the baseline normalized plasma density in the flux aligned coordinate system. The region along the center cusp (i.e. near Φ 0) is highlighted using a red manifold. Because the length scales in this region are smaller than the probe tip resolution, it is assumed that the features are smeared by the measurement. The width of the plasma is smaller than the probe diameter and is difficult to resolve using the current techniques. Because of this, the region indicated by the red manifold in Figure 5.2 should be ignored. It is typically assumed that the streamline connecting the cusp to the central plasma region take on the same density[56, 1]. This is useful in determining an appropriate replacement for the cusp region. Figure 5.3 shows Figure 5.2 from the perspective of the cyan marker. Here the unresolved region of the measurement has been removed. From this perspective it is clear that there is a direct correlation between the stream function value and the plasma density. Notice that the plasma density appears to be constant along the scalar potential coordinate. The density seems to be an even function of the stream contours allowing the density values to be plotted against the absolute value of the stream function.

To mitigate end effects, only the surrounding the center cusp is considered as illustrated in Figure 5.4. Here, the plasma density measurements along the red lines are plotted against the magnitude of the corresponding stream function values. Figure 5.5 shows the density plotted against the stream function for every case. The plots are separated into the baseline field configuration shown on the left and the strong field configuration shown on the right. Within a given field configuration, the normalized density's dependence on the stream function shows

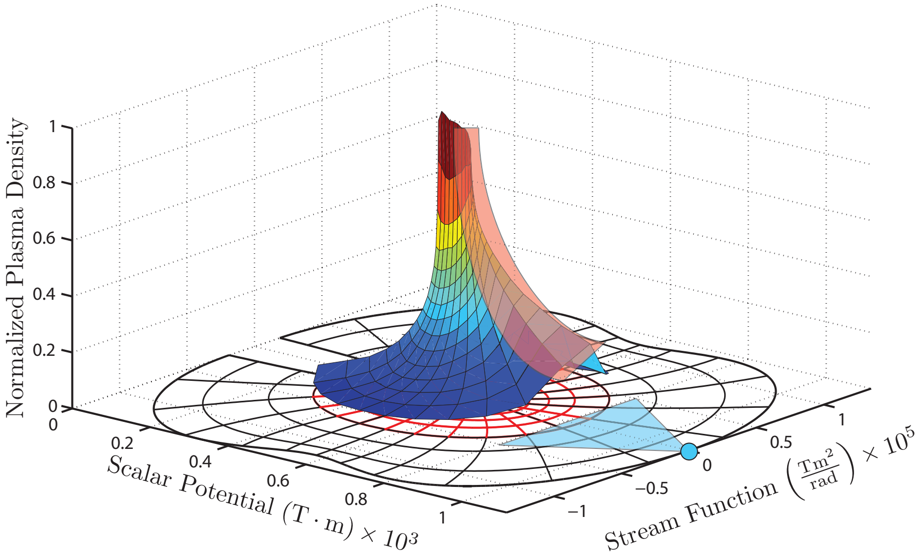

Figure 5.2: The plasma density plotted in the flux aligned coordinate system. The region highlighted by the red manifold represents the center of the magnetic cusp where the length scale is smaller than the resolution of the probe, thus the region is deemed unresolved. The cyan marker shows the perspective of Figure 5.3

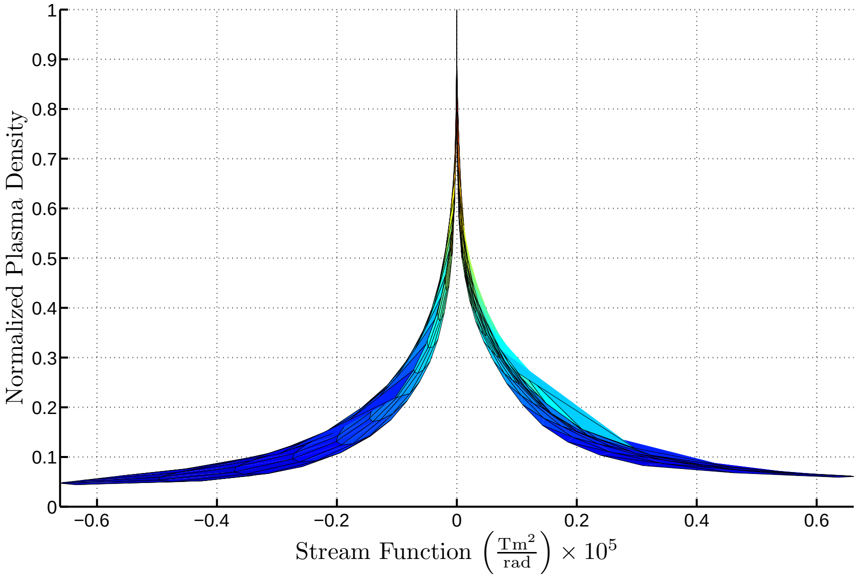

Figure 5.3: The plasma density surface shown from the perspective of the cyan marker in Figure 5.2. The unresolved measurement region has been removed. The stream function contours are isopycnic.

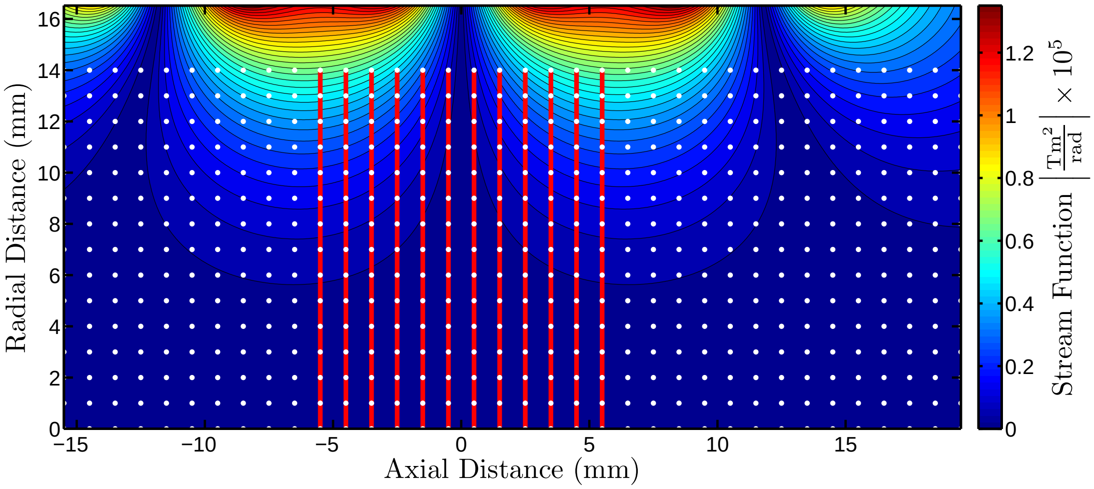

Figure 5.4: Center cusp region used in determining the plasma structure's dependence on the stream function. The white dots show the measurement locations. The red lines correspond to the periodic magnetic domain that surrounds the center cusp, as shown for the experimental apparatus in Figure 3.1.

good agreement. approximate trend lines are shown for each configuration by averaging the values.

The averaged trend lines in Figure 5.5 show similar behavior and can be divided into three regions as shown in Figure 5.6. The first region is marked by the sharp vertical drop near null values of the stream function. Here the density drops irrespective of the stream function, thus it can be concluded that "Region 1" does not have a dependence on the stream function. "Region 2" is marked by an exponential decay. This region is saved for future analysis. Finally, "Region 3" shows a very gradual fall off, however, because this region is well below the exponential cutoff; it is ignored.

The trend lines for the two magnetic field configurations have slight disagreement as seen on the left side of Figure 5.7. The reference value chosen for these curves is based on the maximum plasma density found in the domain. This occurs at the hollow cathode exit which is well within "Region 1". In order to

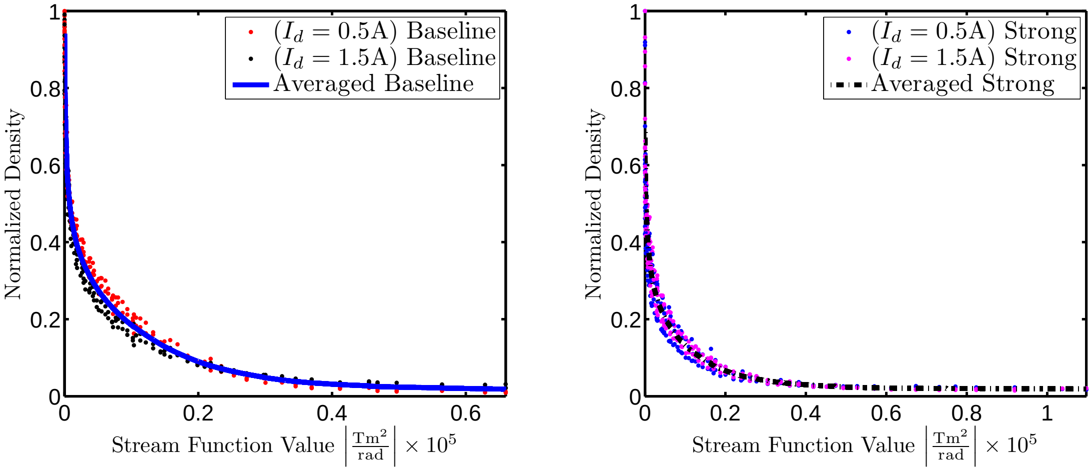

Figure 5.5: Normalized plasma density plotted against the stream function for the center cusp region.

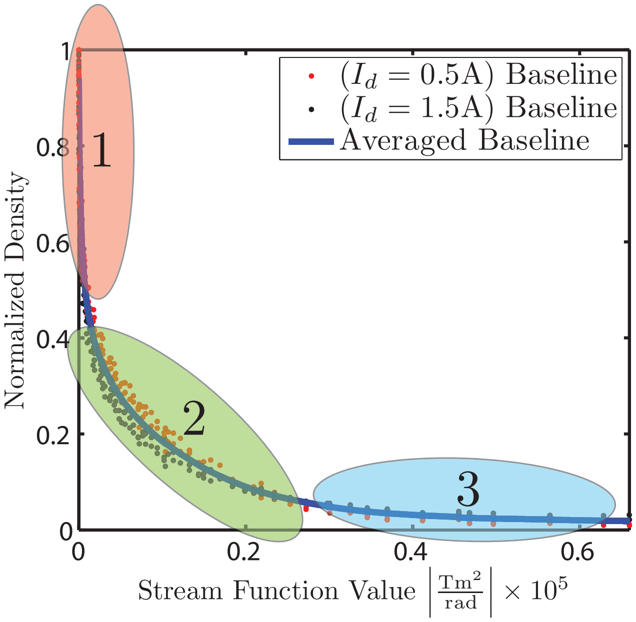

Figure 5.6: Three distinct regions describe the plasma density relation to the stream function. "Region 2 "is used to predict the plasma structure between the bulk region and the anode wall.

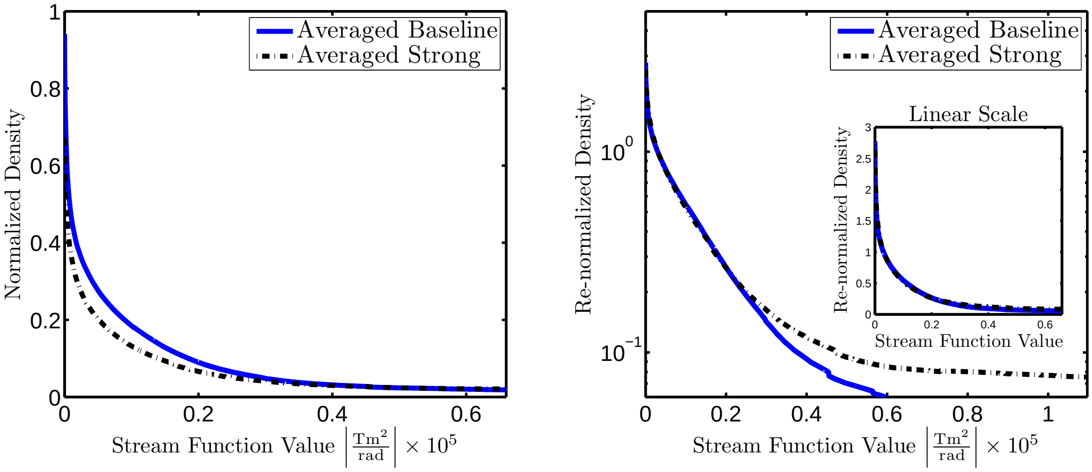

Figure 5.7: The averaged trend lines from Figure 5.5 are shown together. Re-normalizing by the density value at the "Region 2", $n_{Reg.2}$, entrance collapses the two curves as seen in the pullout in the right figure. The main graph in the right figure shows the exponential dependence in the straight section of the semi-log plot.

remove the effect of the hollow cathode, it is more appropriate to normalize the data by the value at the entrance of "Region 2", which is denoted as $n_{Reg.2}$. By using this as the new reference value, the magnetic field line's attenuation of the plasma to the wall can be compared fairly. This re-normalization of the trend lines is shown in the pullout of the right plot in Figure 5.7. The main plot shows the same curves plotted on a semi-log scale. As mentioned previously, "Region 2" is observed to have features that resemble exponential decay. This is confirmed by the straight section seen here. Further the exponential dependence is the same for both magnetic field configurations up to $\Psi \approx 2.5 \times 10^{-6}\ \frac{\text{Tm}^2}{\text{rad}}$, which is taken as the entrance to "Region 3". This corresponds to roughly 4% of the maximum density seen in Figures 3.14 & 3.15 and is considered negligible. Fitting the straight section of the re-normalized plot with the original data yields a slope of -7.6×10^5 and an empirically determined density dependence given in Equation (5.1), where $\widetilde{n}$ represents the re-normalized density.

$$\widetilde{n} = \frac{n(\Psi)}{n_{Reg.2}} \approx exp\left(-7.6 \times 10^{5}\Psi\right) \tag{5.1}$$

5.3 Adjusted Plasma Volume and Anode Loss Area

One of the primary complications with miniature ring-cusp discharge analysis is the pervasive magnetic field. In large devices, the magnetic field is generally contained in a narrow region around the surface of the discharge chamber resulting in a relatively large uniform area in the center allows for a simple control volume analysis[29]. This methodology is useful for first-order discharge chamber design, and predicting the stability of the plasma. Typically, the volume of the plasma is taken to be the physical volume of the vessel. In the miniature plasma device, however, the magnetic field occupies a large portion of the chamber thus making the actual plasma volume uncertain.

Due to the complicated cathode region which led to the need for a re-normalization, Equation (5.1) cannot be used to predict the complete density profile of a discharge chamber. It can, however, be used to predict the effective plasma volume and the loss area of the anode by developing a weighting function for the geometry of the discharge chamber. Because there is not a dependence on the stream function in “Region 1”, this region can not be predicted. The entrance to“Region 2” is taken to be the departure from linearity in the semi-log plot at $3 \times 10^{-7}\ \frac{\mathrm{Tm}^2}{\mathrm{rad}}$. Densities below this valuel are taken to have a value of unity. This yields the piecewise function given in Equation (5.2), where the constant has been added in the exponent to force a continuous function.

$$w(\Psi) = \begin{cases} 1, & \text{if } \Psi < 3 \times 10^{-7} \, \frac{\mathrm{Tm}^2}{\mathrm{rad}} \\ exp\left\{-7.6 \times 10^{-5} \left(\Psi - 3 \times 10^{-7}\right)\right\}, & \text{if } \Psi \geq 3 \times 10^{-7} \, \frac{\mathrm{Tm}^2}{\mathrm{rad}} \end{cases} \tag{5.2}$$

5.3.1 Weighting Function for Anode Loss Area

Equation (5.2) can be applied to the vessel dimensions to account for the reduced plasma dimensions. A similar approach is already used to determine the plasma loss area through the cusps. Typically, the loss area for the plasma is taken to be on the order of the hybrid gyroradius, given in Equation (2.4). This is simply the geometric mean of the ion and electron gyroradii.

The loss width's dependence on the hybrid gyroradius is based on measurements made by various research efforts[3, 27]. Although researchers generally agree that the loss is on the order of the hybrid gyroradius, there is some disagreement on the way that the length scale is measured and reported. Most of the experiments done to determine the leak width use current carrying wires to generate the magnetic field. This configuration differs from those used in ion thrusters in two ways. First, because the current source initiates at the wires, the magnetic field strength generated at the cusp between the wires is weakest at the loss point. In contrast, the magnetic field strength from a permanent magnet is strongest in the loss area as illustrated in Figure 5.8; therefore, in permanent magnet configurations the length scales are much smaller at the cusp. This can lead to the smearing of the plasma density since the probe tip is unable to resolve the spatial features of the cusp region. This is the case in the highlighted region of Figure 5.2. The second difference is in the boundary itself. The boundary in

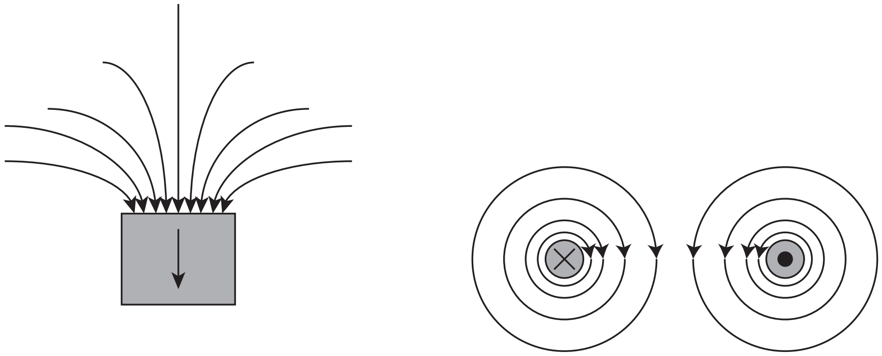

Figure 5.8: Magnetic field of a permanent magnet and a "picket fence" wire configuration on the left and right respectively. The length scales in the loss region are much smaller in the permanent magnet due to its proximity to the source.

the wired configuration is marked by a sheath to a region of sufficiently differing plasma density. The location of this sheath is somewhat ambiguous and brings up the question of where the measurement should be made to capture the loss plane. Cusp discharges that employ a magnetic field that terminates at the anode surface, however, have a definitive conducting boundary that acts as the loss surface. While this provides a definitive location for the plasma loss, measuring in this region is difficult without significant modifications to the device. All of these issues question the methodology of determining the length scale for plasma loss.

Most experiments use some variant of the "full-width at half-max" in determining the length scale of the plasma loss[3]. However, Figure 5.2 shows that the measurement of the peak value can be highly dependent on the resolution of the measurement surface. To avoid this uncertainty, Equation (5.2) is used to determine the plasma loss area at the anode surface. Although Equation (5.2) does not strictly hold for the plasma density measurements, using a nominal bulk plasma density as the reference value allows the plasma to stream freely to the wall at the cusp[56]. The profile at the anode, shown in Figure 5.9, can then

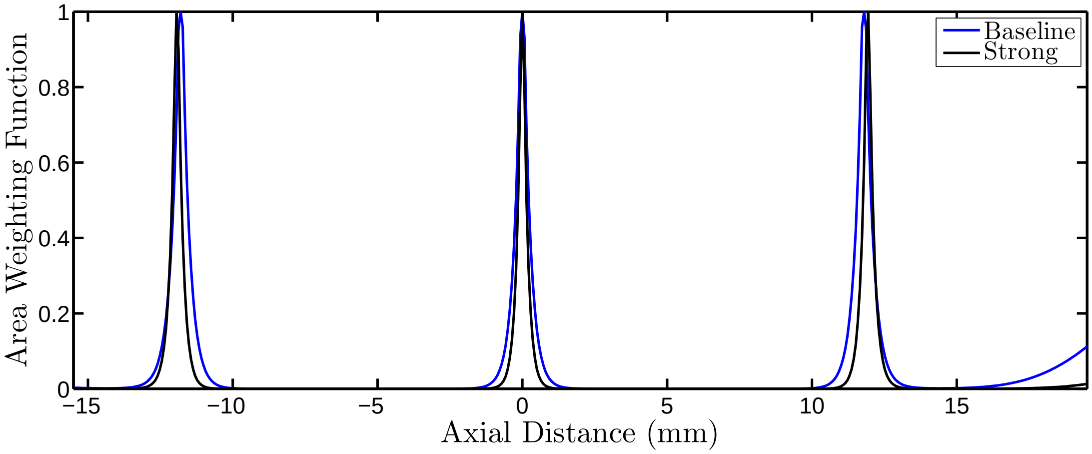

Figure 5.9: Weighting for the loss area along the anode wall for the baseline and strong magnetic field configurations.

be used as a weighting function for the plasma. This is similar to designating a loss region, however, it has the additional advantage of describing the loss to the entire anode surface including regions where the magnetic field impinges the boundaries at an oblique angle. Further, it takes in to account the attenuation of the plasma as it moves through the oblique regions. In the event that the magnetic field between the cusp is weak enough between the cusps, the plasma loss would be captured with this method as well, something that would be overlooked using the traditional hybrid loss method.

A comparison of the loss area generated by Equation (5.2) to that predicted by the hybrid gyroradii is given in Table 5.1. To calculate the total loss area, Equation (5.3) is used. Several assumptions are made on the plasma properties in Table 5.1, thus it is only used to illustrate an order of magnitude agreement with the weighting function method. Here it is assumed that the ion temperature is equivalent to the measured neutral temperature from the chamber walls. The higher values obtained using the hybrid loss width method may be attributed to the artificial smearing of the density profile when calculating the full-width at

Table 5.1: Comparison of the total hybrid loss area of the three magnet rings to that using the weighting function method of Equation 5.3. The loss width used is $4r_h$ as suggested by Hershkowitz[3]. For comparison, the surface of area of the anode is $3,632\ \mathrm{mm}^2$

	Integrated Area Equation (5.3)	**Hybrid Loss Area**, $3 \times (2\pi R 4 r_h)$
Baseline	$213\ \mathrm{mm}^2$	$242\ \mathrm{mm}^2$
Strong	$132\ \mathrm{mm}^2$	$196\ \mathrm{mm}^2$

half-max. Just as the hybrid loss width is dependent on the plasma temperature, Equation (5.2) should only be used for plasmas with similar properties.

$$A_a = 2\pi R \int_0^L w\left(\Psi\left(z, r = R\right)\right) \mathrm{d}z \tag{5.3}$$

5.3.1.1 Anode Loss Area for Negative Plasma Potentials

In the case of a negative plasma potential, as is seen in Chapter 3, the sheath potential structure repels all ions from the anode wall. The location of this reflection is on the order of a Debye length away from the wall, which in the present conditions are ~ 0.01 mm. Because the ions do not reach the wall, the loss width at the magnet face is taken to be two gyroradii of the plasma electrons at thermal velocity[31]. Therefore, Equation (5.3) should only be used in the case of plasma potentials greater than the anode potential. The magnetic field strength value for the gyroradius should be taken at the null stream function contour.

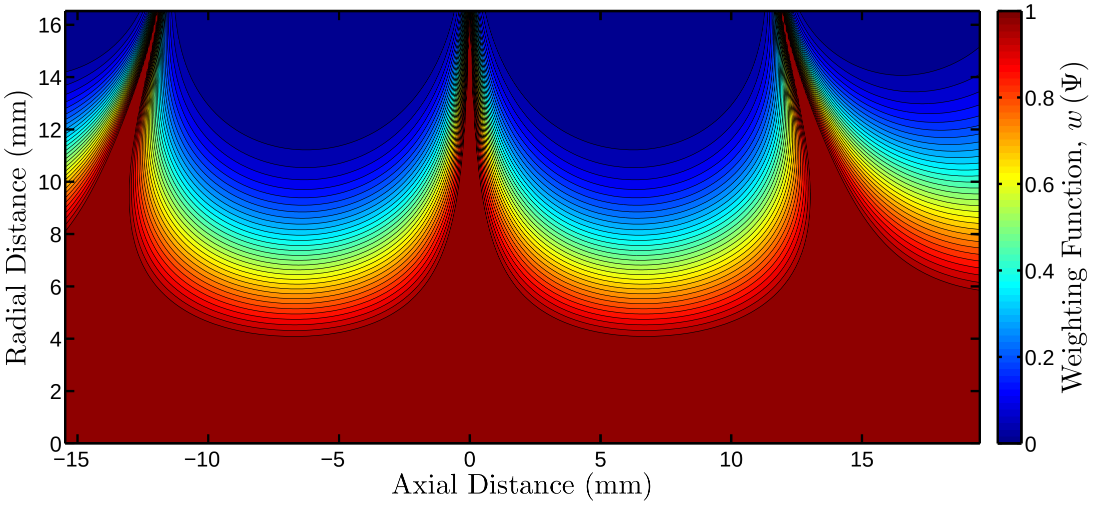

Figure 5.10: Weighting function for the entire plasma domain shown for the baseline magnetic field configuration.

5.3.2 Weighting Function to determine Adjusted Plasma Volume

The reduction of the loss area through the hybrid gyroradii is a common practice in designing multi-pole devices; however, no such reduction is done for the volume. As mentioned previously, the vessel volume is usually assumed to be equivalent to the plasma volume. The measurements from Chapter 3 show that there is a significant reduction in plasma volume from the magnetic confinement. Applying Equation (5.2) to the entire volume gives an estimate of the plasma volume. The weighting is shown in Figure 5.10. The adjusted volumes can be calculated using Equation (5.4) and is summarized in Table 5.2. Note that by using this method, an arbitrary cutoff is not necessary. Calculating the volume using the cutoff stream contour, $\Psi = 3 \times 10^{-7}$, yields roughly a 10% reduction in volume from Equation (5.4).

$$V_p = 2\pi \int_0^R \int_0^L r w\left(\Psi\left(z, r\right)\right) \mathrm{d}z \mathrm{d}r \tag{5.4}$$

Table 5.2: Plasma volume estimated using Equation 5.4. The volume of the vessel is 3.0×10^{-5} m^3 and is used for the normalized volume.

	Volume (m^3)	Normalized Volume
Baseline	1.4×10^{-5}	0.47
Strong	1.1×10^{-5}	0.37

5.4 Magnet Length Sensitivity Study

To demonstrate how the stream function contours affects the plasma volume and anode loss area, a study was conducted on the plasma volume and loss area's dependence on the permanent magnet length. The permanent magnet length was varied from 0 to 3 times the baseline magnet from Chapter 3. The baseline and strong field configurations correspond to 1 and 2 times the block magnet's length respectively. In this study, the stream function contours were calculated for each length factor while constraining the three rings to have the same value. The results are shown in Figure 5.11. Typically, discharge chambers are designed to minimize the loss area and maximize the plasma volume; therefore, the area metric is expressed as $\left(1 - \frac{A_{loss}}{A_{anode}}\right)\%$ such that a higher value is desired. This is done to more readily demonstrate the trade off of plasma volume to loss area

As described in Section 4.4.3 the effect of lengthening the magnet acts to increase the field strength near the surface of the magnet. This decreases the loss area of the plasma. Additionally, the stream lines are forced together and decrease the effective volume of the plasma. This behavior is reflected in Figure 5.11. While lengthening the permanent magnet decreases the loss area, there is a diminishing return as seen by the blue curve. Further, for a marginal decrease in anode loss area the decrease in volume can be much more significant. This explains why poor performance was seen in the strong field case of Chapter 3.

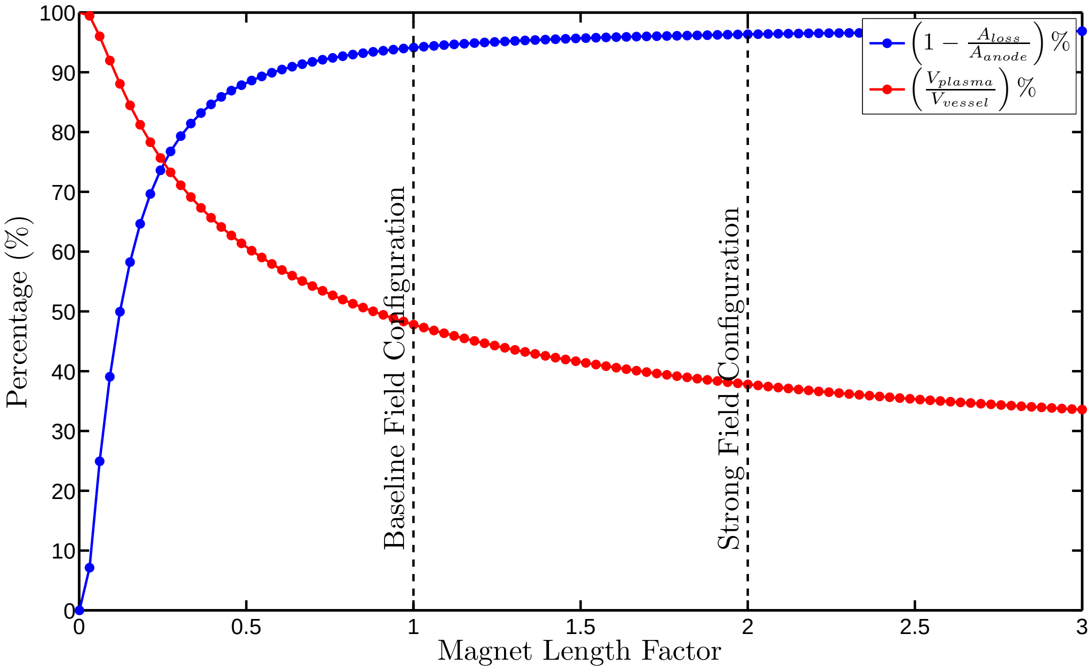

Figure 5.11: Anode loss area and plasma volume dependence on the permanent magnet length.

Although the strong field reduced the loss area, there was also a significant decrease in the plasma volume. Appropriate metrics must be created in evaluating the trade-off between maximizing the plasma volume and minimizing the anode loss area. The methodology presented here determines the plasma volume and loss area from the magnetic field configuration and is used in Chapter 6 to develop a design procedure for miniature ring-cusp discharges.

CHAPTER 6

Miniature Ring-Cusp Discharge Design

In the previous chapter it was found that the plasma density showed a strong correlation to the stream function values of the magnetic field. Because of the highly non-uniform plasma discharge from the cathode, this technique cannot be used to predict the plasma density for the entire chamber; however, it does yield a useful measure for the effective plasma volume.

The current chapter investigates the use of these parameters in developing an initial design tool for miniature discharges. Plasma potentials below the anode voltage seen in the experimental measurements of Chapter 3 suggest the existence of an ion repelling sheath. Therefore, the plasma is not only subject to a discharge instability, but also running in a non-efficient regime as stated in Chapter 2. The sheath character is nonlinear and not well understood for negative plasma potentials[2]. The behavior of the plasma as it moves through a varying magnetic field, such as the one currently considered, further complicates the situation and is suggested for future studies.

The objective of this chapter is to outline the mechanisms that determine the sign of the plasma potential as well as to develop typical values that can be used for a miniature discharge design. To conclude, a redesign of the discharge device's magnetic field is examined with imposed constraints followed by a recapitulation of the design procedure.

6.1 Plasma Electron Particle Balance

As discussed in Chapter 2, depending on the balance of positive and negative species, the plasma potential adjusts with respect to its boundaries to maintain quasi-neutrality. In laboratory plasmas, the electron population is typically much more energetic than the ion population leading to an electron repulsion sheath. However, as seen in the plasma potential measurements in Figure 3.20, miniature discharges appear to be susceptible to a scenario that is not commonly encountered. At this scale, the magnetic field strength at the cusp can inhibit the plasma electron loss and drives the plasma potential below the anode voltage, leading to an ion repelling sheath.

While the a discharge instability cannot be predicted easily, the sign of the plasma potential with respect to the anode can be calculated with a particle balance of the plasma electrons. This method has been used successfully for various studies and has been modified to take into consideration the inherent incongruence of the plasma and primary electron volumes found in small-scale devices[29, 30, 31]. The plasma electron production, I_e, comes from four separate collisions:

1. Post-ionization primaries thermalized with the background plasma, I_{ip}:

$$I_{ip} = n_o \left(n_p V_p\right) \langle \sigma_i v_p \rangle \tag{6.1}$$

   where n_o is the neutral density, $n_p V_p$ express the total number of primary electrons, and $\langle \sigma_i v_p \rangle$ is the reaction rate coefficient for the ion-neutral ionization collision given by Rapp and Englander[57].

2. Post-excitation primaries thermalized with the background plasma, I_{*p}:

   $$I_{*p} = n_o \left(n_p V_p\right) \langle \sigma_* v_p \rangle \tag{6.2}$$

   where $\langle \sigma_i v_p \rangle$ is the reaction rate coefficient for the ion-neutral excitation collision given by Hayashi[58].

3. Primaries thermalized with the background plasma in the absence of a heavy species collision, $I_{\tau p}$:

   $$I_{\tau p} = \frac{n_p V_p}{\tau} \tag{6.3}$$

   where τ is the time for a primary electron to thermalize with a background population of Maxwellian electrons given by Spitzer[59].

4. Plasma electrons generated from ionization collisions, I_i:

   $$I_i = n_o \left[\left(n_p V_p\right) \langle \sigma_i v_p \rangle + \left(n_e V_e\right) \langle \sigma_i v_e \rangle\right] \tag{6.4}$$

   where $\langle \sigma_i v_e \rangle$ is the reaction rate coefficient for ionization due to the Maxwellian population.

These terms can be combined to yield the plasma electron production,

$$I_e = I_{ip} + I_{*p} + I_{\tau p} + I_i \tag{6.5}$$

Because the ion loss surfaces are at cathode potential, it is assumed that the majority of the plasma electron loss, I_a, occurs at the anode. The anode loss area, A_a, for the plasma electrons is calculated using the stream function technique.

The total particle loss can be expressed,

$$I_a = \left[\frac{1}{4} n_e \sqrt{\frac{8kT_e}{\pi m_e}} A_a\right] f^{-1}(\phi) \tag{6.6}$$

where the bracketed term in Equation (6.6) is the random plasma electron loss to the anode wall and the sheath modifier, $f(\phi)$, is the attraction or repulsion of the plasma electrons by the sheath. Values of $f(\phi) < 1$ represent an ion repulsion sheath and $f(\phi) > 1$ represent electron repulsion sheaths. There is a portion of the tail of the Maxwellian that has sufficient energy to be lost to the cathode surfaces. The contribution from this current was calculated to have a small effect and is neglected.

The change in current due to the sheath, $f(\phi)$, can be solved for by equating Equations (6.6) & (6.5).

$$f(\phi) = \frac{\frac{1}{4} n_e \sqrt{\frac{8kT_e}{\pi m_e}} A_a}{n_p V_p \left[n_o \left(2\langle\sigma_i v_p\rangle + \langle\sigma_* v_p\rangle\right) + \frac{1}{\tau}\right] + n_o \left(n_e V_e\right) \langle\sigma_i v_e\rangle} \tag{6.7}$$

In order to maintain quasi-neutrality, the sheath modifier, $f(\phi)$, balances the random plasma electron loss with the electrons generated within the control volume. The experimental measurements from Chapter 3 indicate a negative plasma potential for both the baseline and strong field configurations, thus $f(\phi)$ has a value less than unity.

6.1.1 Primary and Plasma Electron Particle Calculation

As stated in Section 2.3.2, the ideal value of $f(\phi)$ is unity. Because the terms in Equation (6.7) for $f(\phi)$ are highly dependent on the operating condition of the device, representative values must be chosen for the various plasma parameters before determining the optimal magnetic field configuration. The stream function analysis can be used to calculate the various geometric properties such as the anode area, ion loss area, and the plasma volume. These change with the magnet dimensions. Experimental data can be used to determine typical values of the remaining plasma parameters.

For the current discharge chamber geometry, the neutral density has been calculated to be 4.0×19 m^{-3} for a xenon flow rate of 0.5 sccm and the probe access slot. The electron temperature, T_e, has been chosen to be ~ 3 eV and the reaction rate coefficients have been calculated for primary energies of ~ 18 eV. The plasma density is highly dependent on the operating condition; however, using a nominal value of 1×10^{18} m^{-3} for the plasma density, the Spitzer slowing time, τ can be calculated for the primaries[59].

The remaining values in Equation (6.7) involve the electron species. While densities are also a strong function of the discharge operating conditions, nominal ratios can be calculated from experimental data. Because of the variability of the density throughout the chamber, the order of magnitude for the ratio of species count is solved for keeping with the control volume approach. The two unknowns are then the plasma and the primary electron particle count. The ratio of these can be found by rearranging Equation (6.7) as seen in Equation (6.8).

$$\frac{n_p V_p}{n_e V_e} = \frac{\frac{A_a}{4V_e} n_e \sqrt{\frac{8kT_e}{\pi m_e}} - f\left(\phi\right) n_o \langle \sigma_i v_e \rangle}{f\left(\phi\right) \left[n_o \left(2\langle \sigma_i v_p \rangle + \langle \sigma_* v_p \rangle \right) + \frac{1}{\tau} \right]} \tag{6.8}$$

The representative plasma potentials for the sheath function are taken from the centerline of the measurements beyond the cathode influence. This is done to mitigate the influence of the magnetic field as the plasma travels to the boundaries. A summary of the plasma potentials relative to the anode voltage are given in Table 6.1. Because the plasma potentials are negative, the electron gyroradii is used for the loss width as stated in Section 5.3.1.1. The magnetic field values should be taken at the null stream function value. In the case of a positive plasma potential, the stream function method of Equation (5.3) should be used. In both cases, the plasma volume is estimated with Equation (5.4). The merging of these two regions is not well understood in terms of how the loss area for the plasma electrons merges to the loss region calculated by Equation (5.3). For the cases measured, the plasma electron loss area is on the order of 10% of that calculated by the stream function method. The treatment of the loss area for plasma electrons for different conditions is an unresolved issue and is closely tied to the ambiguity of the ion repelling sheath structure[2].

Table 6.1: Representative plasma potentials relative to anode potential. Values are taken at the centerline beyond the cathode influence.

	Baseline Magnets	Strong Magnets
0.5 A	−3.0	−3.7
1.5 A	−1.0	−2.7

Solving the system yields electron species ratios summarized in Table 6.2. The values used for the calculation are taken from experimental measurements rather than the assumed values stated earlier; these will be used in the following design cases. The primary to plasma electron ratio is dependent on the discharge power, thus as the discharge current is ramped up, the ionization level increases producing more plasma electrons. The order of magnitude of the primary to plasma electron ratio is 10% and is similar to that found in other studies[18]. This is used for the rough design tool in later sections. A 20% ratio was found by Oksuz in his studies of negative plasma potentials[31]. It should be noted that the conditions are much different than the current study.

Table 6.2: Primary electron to plasma electron ratio, $\frac{n_p V_p}{n_e V_e}$.

	Baseline Magnets	Strong Magnets
0.5 A	0.33	0.47
1.5 A	0.12	0.22

6.1.1.1 Quasi-neutrality and Electron Structure

Typically, quasi-neutrality is expressed as the balance between the ion and electron density, or,

$$n_i = n_e + n_p \tag{6.9}$$

While this could be used to solve for the electron density values and the primary electron volume, doing so would not be representative of the plasma structure. Due to the primaries' confinement to the magnetic field, they typically are kept with in a vary narrow region along the null stream function contour. Therefore, the plasma electron structure can be thought of as having a skeleton structure of primary electrons surrounded by plasma electrons. Local high plasma density regions could indicate such a structure even though the high primary currents do not show up in the Langmuir traces.

In the baseline magnetic field configuration, the primary skeleton extends to the length of the chamber while in the strong field configuration the high densities seem to be confined to the first set of ring-cusps. This further supports the notion that the strong field configuration represents a general over-confinement of the plasma. Since the optimal magnetic field configuration is expected to be weaker than the baseline configuration, it is assumed that the primary electron structure has sufficient penetration throughout the discharge chamber.

6.1.1.2 Order of Magnitude Analysis

An order of magnitude analysis can be made on Equation (6.7) to yield a simplified form. Dividing Equation (6.7) through by the plasma electron particle count yields Equation (6.10).

$$f\left(\phi\right) = \frac{\frac{1}{4V_e}\sqrt{\frac{8kT_e}{\pi m_e}}A_a}{\left(\frac{n_p V_p}{n_e V_e}\right)\left[n_o\left(2\langle\sigma_i v_p\rangle + \langle\sigma_* v_p\rangle\right) + \frac{1}{\tau}\right] + n_o\langle\sigma_i v_e\rangle} \tag{6.10}$$

For the current conditions, the Maxwellian contribution is one to two orders of magnitude below that of the primary contribution; therefore, this term is dropped. As stated previously, the anode loss area is taken to be 10% of the anode loss area based on the stream function calculations. Because the primary to plasma density ratios are also on the order of 10% these terms are assumed to approximately cancel out yielding the simplified form in Equation (6.11).

$$f\left(\phi\right) \approx \frac{\frac{1}{4V_e}\sqrt{\frac{8kT_e}{\pi m_e}}A_a(\Psi)}{\left[n_o\left(2\langle\sigma_i v_p\rangle + \langle\sigma_* v_p\rangle\right) + \frac{1}{\tau}\right]} \tag{6.11}$$

Typical values for ring-cusp discharges can be used for most of the parameters. The remaining variables in Equation (6.11), V_e & A_a, are dependent on the magnetic field and can be evaluated using the methodology outlined in Chapter 5. Therefore, Equation (6.11) can be used to evaluate the merit of magnetic field configurations for miniature discharges.

6.2 Discharge Design Sensitivity Analyses

As a demonstration, the above design methodology is applied to the discharge device under constraints to reduce the design space. The guidelines for this exercise are:

1. Use the original discharge chamber geometry
2. Use the original ring magnet location and spacing
3. The dimensions of each ring must be the same
4. Use samarium cobalt for the magnetic material

Samarium cobalt is the only material with the combination of high operating temperature and resistance to demagnetization[53, 51]; therefore, only the magnet dimensions are allowed to change for this particular problem. Both the magnet depth and the magnet width are explored creating a design space with two degrees of freedom. The ring magnets' outer radius and axial dimension serve as the two variables for the optimization problem.

From the foregoing analysis of the experimental results, the optimal outer radius, or depth, is expected to be less than that of the baseline configuration. The one-dimensional study in Section 4.4.3 predicts a reduction in magnetic field at the cusp. While this reduces the confinement of the plasma species, it also allows the escape of plasma electrons, thus bringing the plasma potential closer to that of the anode potential. The design space for this variable, the depth scale factor, D^*, ranges from 0.1% to 250% of the baseline outer radius.

Changing the ring magnet's axial width reduces the field strength along the centerline, as shown in Section 4.4.3. Reduction in this parameter expands the field free region and thus the volume utilization of the discharge chamber while increasing the anode loss area. Since the spacing among the magnet rings is fixed, the width factor, W^*, varies from 0.1% to 100%. This corresponds with a very thin magnet to the maximum width given the fixed magnet spacing. A schematic of both design parameters is shown in Figure 6.1.

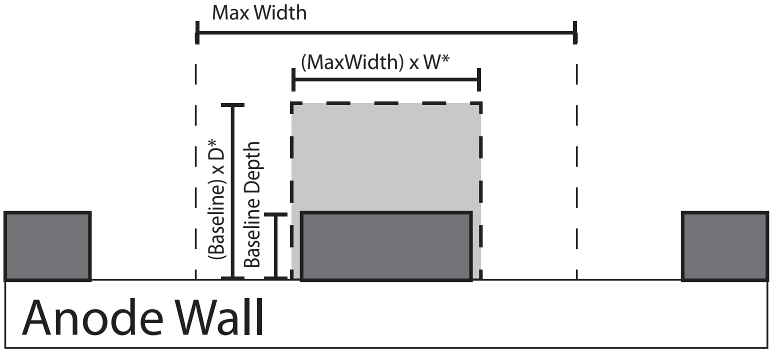

Figure 6.1: Schematic of the design parameters for the magnet dimensions.

By iterating through the design space and calculating the stream function contours, the approximate plasma volumes and loss areas can be found with Equations 5.3 & 5.4. These values, along with nominal values for the intensive properties of the plasma discharge, can be used to calculate the sheath modifier function which yields the plasma potential. Figure 6.2 shows the sheath modifier function versus D^* and W^*. The optimal contour, $f(\phi) = 1$, is highlighted using a red line, and the conditions for the baseline and strong field configuration are marked with yellow and green respectively.

The configuration should be chosen from the optimal contour in Figure 6.2. The optimal point on the contour will ultimately depend on the purpose of the miniature discharge. These may include design objectives such as:

1. Minimizing the anode area: For the most confinement
2. Maximizing the plasma volume: For the most plasma generation
3. Minimizing the magnetic material: For the least cost/weight
4. Maximizing the extraction area: For the most ion throughput

The configurations that correspond to these design objectives are summarized in Figure 6.3. Details for each optimization are given in Figures 6.4-6.11.

Designing for a minimum anode area yields the highest confinement for the plasma species. This leads to relatively large density values, but a poor volume utilization. In an ion thruster this translates to centerline concentrated wear, and thus poor lifetimes. This configuration is shown in Figure 6.5.

Optimizing for a maximum plasma volume would avoid these issues at the expense of plasma density. This occurs due to the reduction in magnetic material. To achieve comparable density values, higher discharge powers may be necessary. Because plasma generation is a function of volume, as seen in Equation (6.4), maximizing the plasma volume allows the discharge to be replenished faster during high thrust operating conditions.

Reducing magnet volume may be considered to increase the thrust to weight ratio of the device as well as reduce the cost of magnetic material if many units

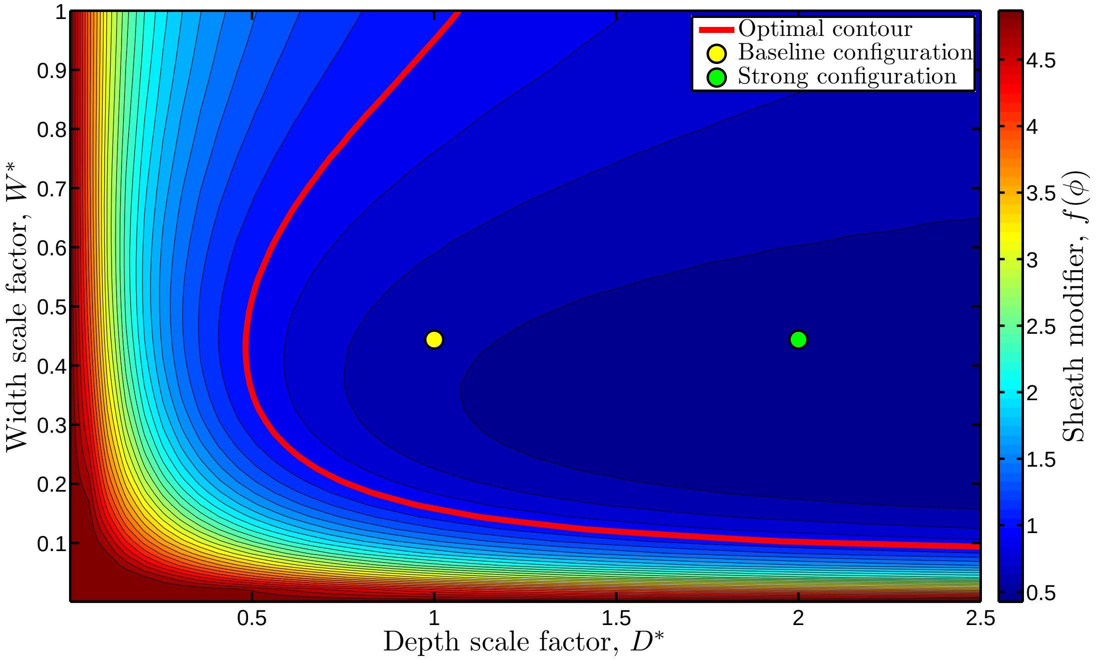

Figure 6.2: Sheath modifier contours for the design space. The red line indicates the boundary between the ion and electron repelling sheath conditions.

are to be built. Reducing magnet volume and cost may be of primary consideration for terrestrial applications. For space applications, this may likely not be a concern since the primary consideration for mass is related to the overall wet mass of the propulsion system. This may become a factor in missions that require a large number of thrusters such as the TPF-I example discussed in Chapter 1. The parameters for minimum magnetic material are seen in Figure 6.8.

The most important optimization parameter for ion sources is the ion flux surface area. Maximizing the extraction area translates directly to a more efficient thruster by better utilizing the surface area of the extraction plane. The results for this optimization are shown in Figure 6.10.

As seen in Figure 6.3, designing for plasma volume, extraction area, and magnetic material all occur in roughly the same design space. The ideal magnet configuration, under the current design restrictions, would have $\sim 75\% - 95\%$ depth scale factor and have a width scale factor of roughly 18%.

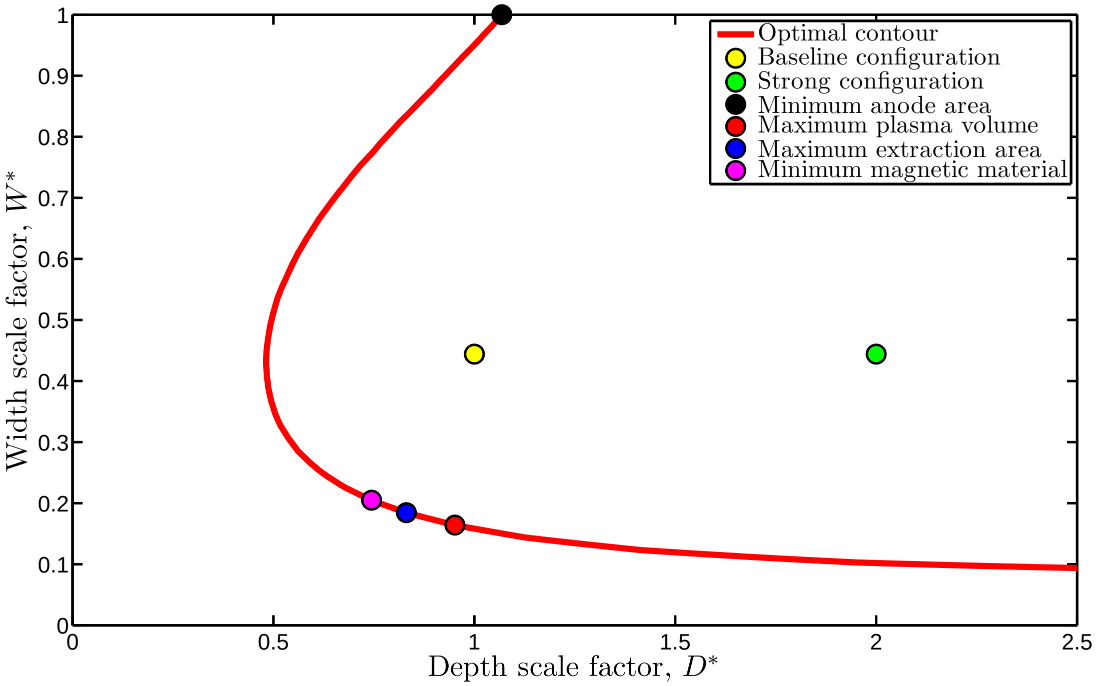

Figure 6.3: Summary of the different optimization conditions shown along with the baseline and strong field configurations. The red line represents efficient discharge operation.

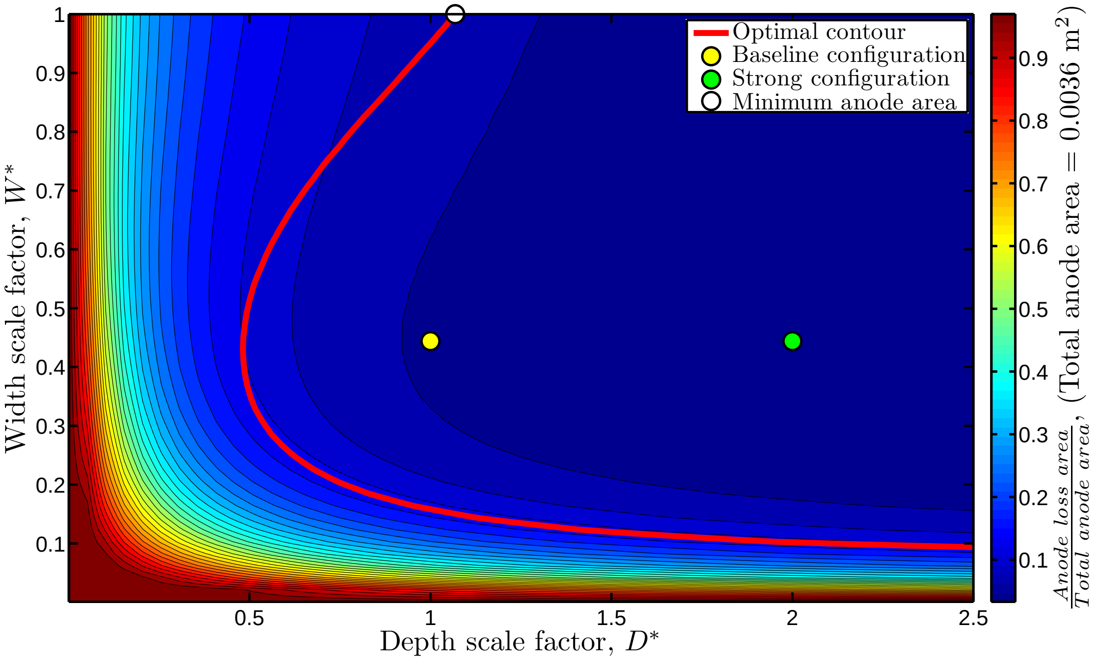

Figure 6.4: Anode area contours normalized by the total anode surface area. The minimum anode area maximizes peak plasma density at the expense of volume utilization. This is typically not desirable.

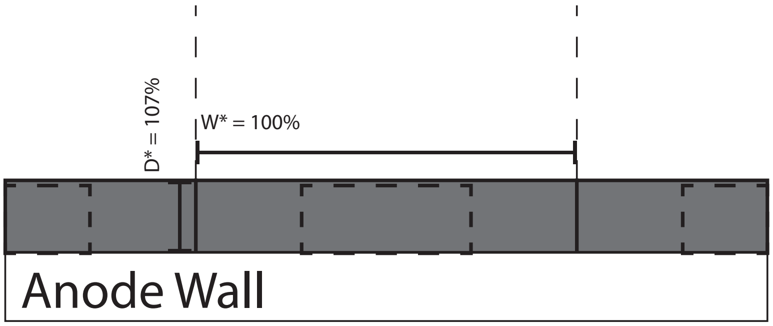

Figure 6.5: Illustration of magnets optimized for minimum anode area. The baseline configuration is shown in dashes.

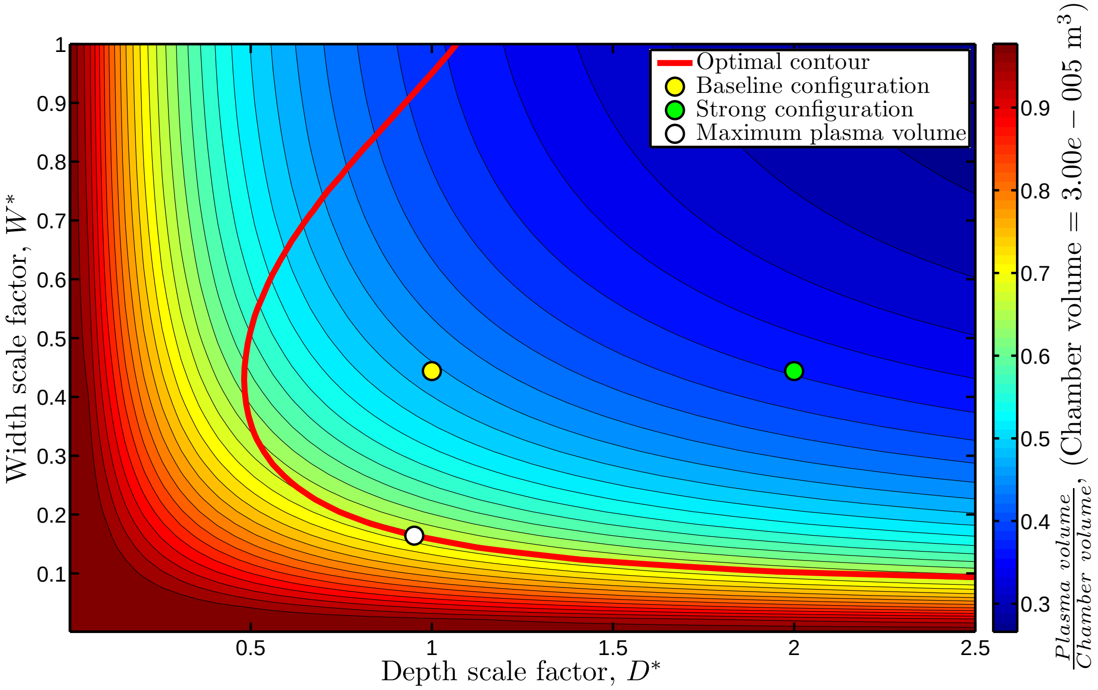

Figure 6.6: Plasma volume contours normalized by the chamber volume. Maximizing the volume increases volume utilization, but may need to run at higher powers to achieve desired plasma density.

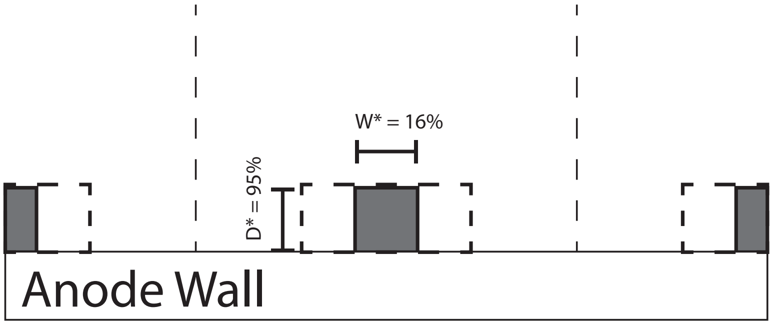

Figure 6.7: Illustration of magnets optimized for maximum plasma volume. The baseline configuration is shown in dashes.

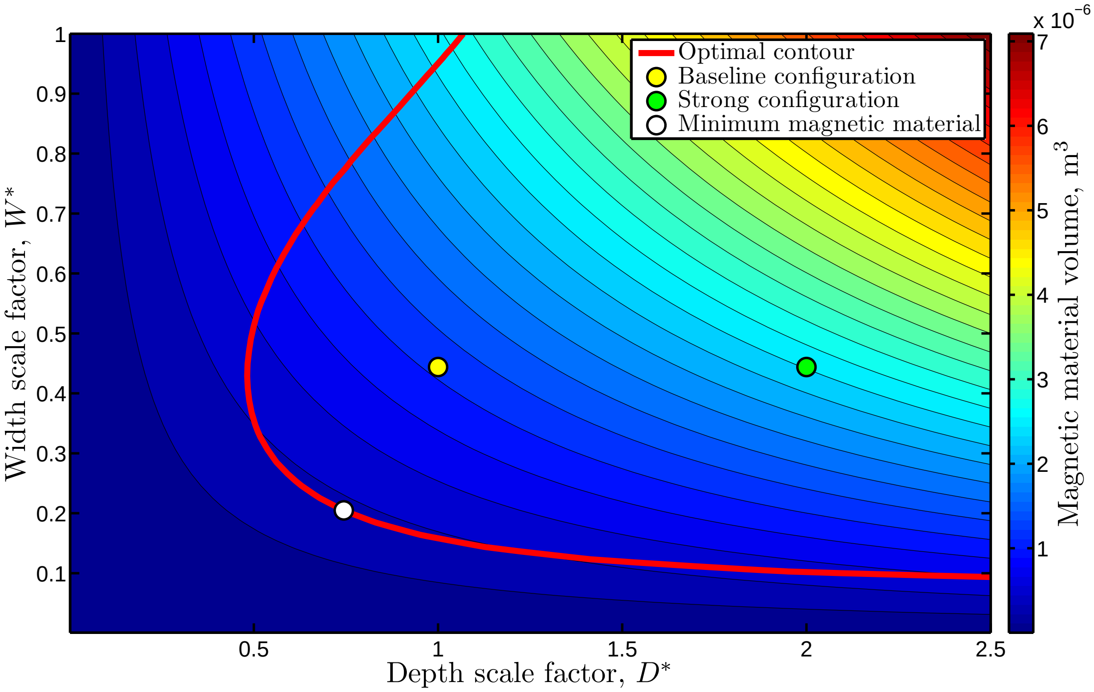

Figure 6.8: Contours for the total permanent magnet volume. Reducing the magnet volume increases the thrust to weight ratio of the device. Reducing the material also reduces the cost for the device in non-space applications.

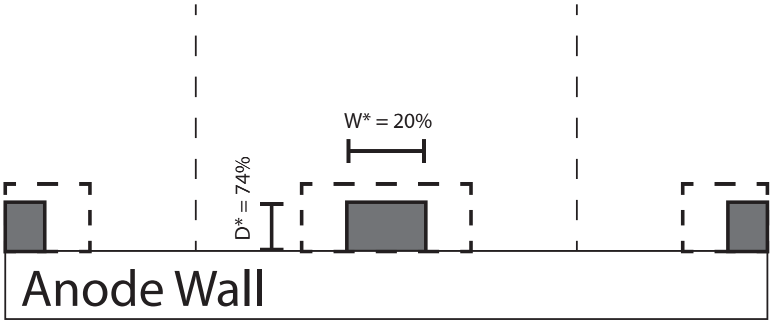

Figure 6.9: Illustration of magnets optimized for minimum permanent magnet volume. The baseline configuration is shown in dashes.

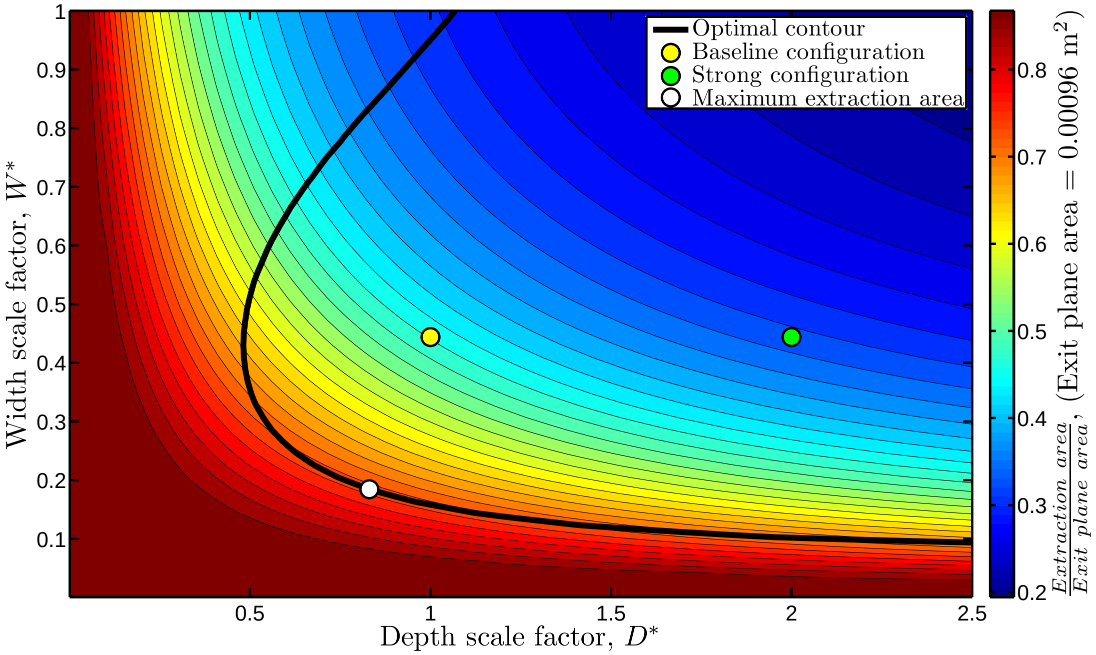

Figure 6.10: Extraction area contours normalized by the geometric exit plane area. Maximizing the extraction area optimizes the total available region to produce beam current.

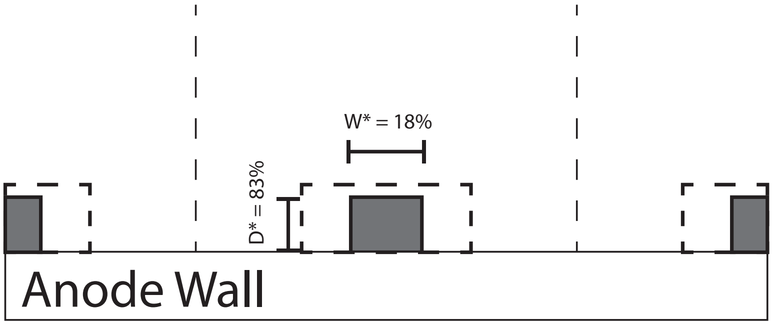

Figure 6.11: Illustration of magnets optimized for maximum extraction plane area. The baseline configuration is shown in dashes.

6.2.1 Discharge Redesign Summary

The preceding analysis examines for possible optimization parameters:

1. Minimum anode area
2. Maximum plasma volume
3. Minimum magnetic material
4. Maximum extraction area

Table 6.3 summarizes the plasma volumes, the extraction areas, and the percent change from the baseline configuration. These values are estimated using Equation (5.2) on the plasma volume and the extraction plane. The extraction plane gives an approximation of the total beam current available for thrust. From Table 6.3 it is clear that designing for maximum plasma volume, minimum magnetic material, and maximum extraction area is approximately equivalent. In comparison to the baseline case, this approach increases the total ion throughput and has the added benefit of reducing magnetic material. A comparison of the estimated plasma structure is given in Figure 6.12. The increase in plasma volume at the radial locations further form the axis have a larger contribution, thus the improvement in volume utilization is larger than the visual impression from a two dimensional plot of the discharge.

6.3 Miniature Ion Thruster Design Procedure

The design methodology discussed in Section 6.2 provides a means to quickly asses the merits of different magnetic field designs for miniature discharges. The figure of merit in this case is the plasma potential since the performance is dependent

Table 6.3: Summary of the considered configuration for optimization. Consideration for maximum plasma volume, minimum magnetic material, and maximum extraction area yield the same plasma structures. In a typical ion source, the goal is to maximize the extraction area.

Configuration	Plasma Volume (m^3)	Extraction Area (m^2)	% of Baseline Volume	% of Baseline Ext. Area
Baseline	1.44×10^{-5}	4.60×10^{-4}	100%	100%
Strong	1.14×10^{-5}	3.23×10^{-4}	79%	70%
Min. Anode	1.13×10^{-5}	2.86×10^{-4}	78%	62%
Max Plasma	2.06×10^{-5}	7.21×10^{-4}	143%	157%
Min. Magnet	2.05×10^{-5}	7.22×10^{-4}	142%	157%
Max Ext.	2.05×10^{-5}	7.22×10^{-4}	142%	157%

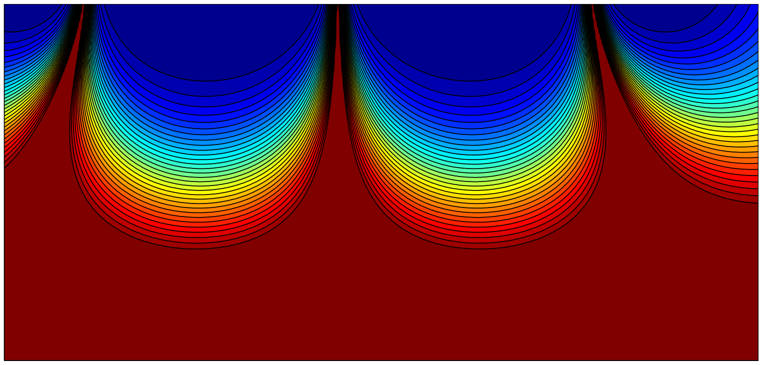

Baseline

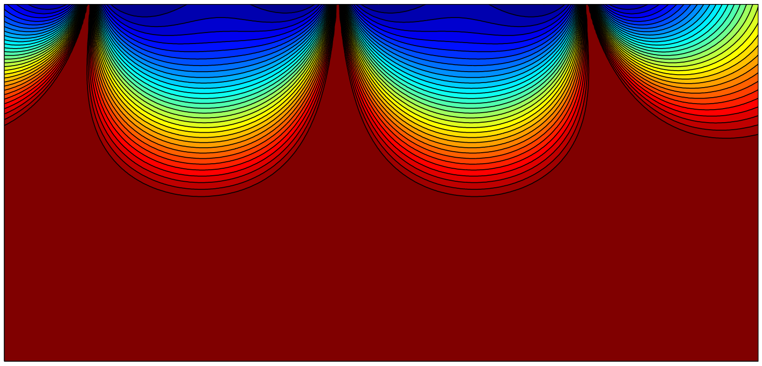

Maximum Extraction Area

Figure 6.12: Comparison of the baseline plasma structure to the extraction area optimized structure.

of the operating conditions. The theory has been developed around ring-cusp discharges with a diameter of ~ 3 cm. The design procedure is as follows:

1. Determine the chamber geometry.
2. Choose an initial magnet configuration. Note that the procedure is only applicable to axisymmetric geometries.
3. Calculate the magnetic field using Equations (4.9) & (4.10).
4. Numerically solve for the stream function contours using the procedure given in Section 4.5.
5. Using the stream function, calculate the weighting functions using Equation (5.2). Integrate the scalar field to obtain, A_a & V_e.
6. Using nominal values for the electron temperature, reaction rate coefficients[57, 58], and Spitzer slowing times[59], calculate the sheath modifier using Equation (6.11). Note that the optimal value of $f(\phi)$ is unity.

The procedure can be automated in an efficient manner to iterate on various parameters. In Section 6.2, the procedure iterates to properly size the magnets. While the procedure is built around obtaining a favorable plasma potential, the transfer function can also be used to find the magnetic field configuration to deliver the maximum plasma density to the extraction plane. Typically this would be done by weakening the magnet adjacent to the extraction plane. While detailed design tools exist with DC-ION, the current method offers a way of quickly evaluating a high number of configurations.

CHAPTER 7

Conclusions and Future Work

A miniature ring cusp discharge is an attractive ion source for a wide array of propulsion applications. To investigate the internal plasma behavior and structure of such a device, a simplified miniature discharge was built using a generalized ring-cusp configuration with access slots for a Langmuir probe. The probe data yielded spatially resolved measurements for plasma density, electron temperature, and plasma potential. These data represent the first such measurements of a miniature ion thruster discharge and conclusively demonstrated the plasma confinement capabilities of a 3 cm discharge on par with plasma densities found in larger devices.

The device was used to investigate the effects of magnetic field strength and to test the possibilities of a discharge instability[21, 29]. It was shown experimentally that the baseline magnetic field, in comparison to a stronger magnetic field configuration, exhibited better volume utilization and more favorable discharge loss. The plasma potential measurements for the strong magnetic field showed the effects of a negative bulk plasma potential relative to the anode, and the likely onset of plasma instability. Ultimately, all three measured properties showed a clear dependence on the magnetic field configuration and were relatively invariant to the operating discharge power.

To further investigate the magnetic field's effect, a framework for magnetic field analysis was developed. Stream function and velocity potential constructs were borrowed from fluid mechanics and applied to the axisymmetric magnetic field[39, 47]. These constructs were used to develop a flux aligned coordinate system by which to investigate ring-cusp plasma structure and behavior. Although not used in the current effort, differential operators and elements were derived for analysis of the plasma two-fluid equations. Further, the analytical formulae were given for block and ring magnets along with an analysis on the effects of altering magnet dimensions. This was used to develop intuition for magnetic field design.

The experimental data was plotted in the flux aligned coordinate system. It was shown that the normalized density had a coherent relationship with the stream function values. A curve-fit was developed and used to estimate the plasma loss areas as well as the volume of the plasma. It was shown that the estimated loss area was on order of the hybrid loss width[3]. Currently, there is no equivalent technique to truncate the plasma volume based on the field configuration. This technique is primarily applicable to small devices where the plasma volume is commonly much smaller than the volume of the chamber.

A method for quickly evaluating the discharge performance for a large design space of magnetic field configurations does not currently exist for miniature ring-cusp discharges. A particle balance on the plasma electrons was used to estimate the electron content of the discharge. This control volume approach was applied to the experimental data and showed that the plasma electrons should be lost to the plasma electron thermal gyroradii. Such a technique had been successful in other studies; however, the extreme prominence of the magnetic field in miniature discharges places a caveat on the simple control volume bulk analysis that can be used for conventional plasma discharges[31]. The treatment of the boundary condition as the plasma potential changes bias with respect to the anode voltage is an unresolved issue. An assumption was made on the loss area transition that utilized the calculated anode loss area. This was used to examine optimized designs for the discharge experiment's magnetic field and ultimately yielded a first-order design methodology for miniature discharges. The design methodology predicts an increase of 57% in extraction area which directly correlates with an increase in maximum thrust.

This optimization effort gave significant insight into the plasma behavior in miniature ring-cusp discharges and several questions were raised about the operation of these devices. Future measurements should attempt to resolve the boundary of the plasma at the anode wall and are currently being investigated[28]. These measurements may give additional insight into the sheath structure and under what conditions it will exhibit an electron sheath as described by Hershkowitz[2]. Emissive probe measurements are suggested to obtain better values for the plasma potential. An investigation of the 3-D effect of large magnets should also be conducted to better understand the original MiXI magnetic field configuration[21].

The primary electron content should also be explored to verify the nature of the negative plasma potential. As stated by Wirz, the primary electrons are almost exclusively responsible for the ionization within miniature discharges. An investigation, given in Appendix A, on the primary electron behavior has already begun using a theoretical derivation for the primary behavior along a single magnetic field line. Additionally, an effort to benchmark a new particle tracking technique for the primaries is shown in Appendix B. Along with current experimental efforts, these will shed light on the true nature of primaries in miniature discharges[28].

The experimental results can be used as a validation and development of computational models such as DC-ION, for miniature discharges[21]. Additionally, the flux coordinate system can be used to investigate and improve the diffusion behavior for the model.

APPENDIX A

Single Field Line Analysis of Charged Particles

Electron bombardment plasma devices depend on the confinement of high-energy electrons, also known as primary electrons, to produce plasma through collisions. This is achieved using the alternating polarity of a series of magnets to create concentrated regions of magnetic field strength. Devices such as ring-cusp ion thrusters and multipole discharges utilize the magnetic mirroring phenomena to extend the confinement time and hence the path length of the primary electrons[60, 26, 27, 61]. This increases the probability of the primary electron ionizing the background neutral gas. While in larger devices a non-negligible amount of ionization can also occur from plasma electrons, in miniature discharges ($\leq$ 5 cm), primary electrons dictate the ionization. Therefore, determining the primary electron density throughout the chamber volume becomes especially important for efficient miniature discharge design[21].

A typical primary electron life cycle begins with an electron born at a thermionic emitter and accelerated through the plasma potential. The electron then travels through the bulk discharge where the electron undergoes inelastic and elastic collisions or terminates at a wall. In an inelastic collision, the primary electron imparts its kinetic energy to a neutral particle. The neutral particle either ionizes and releases an electron creating a plasma electron and a positive ion[57], or excites an electron in the outer shell producing an electronically excited neutral[58]. The post-collision electron is quickly thermalized to the plasma electron population through subsequent lower energy collisions with existing particles[59] . In the event of an elastic collision, the neutral deflects the primary electron and both continue to travel through the discharge chamber[62]. As the electron approaches a magnetized boundary of the domain, it will be reflected by the converging cusp field or be lost if it is within the so-called loss cone.

Because of their discontinuous nature across field lines, primary electrons are often treated with a particle tracking scheme[63, 64, 65, 66, 67]. Particle tracking allows the effects of the magnetic mirror to be clearly implemented within the simulation. While these methods produce realistic particle trajectories and locations, they require an inordinate amount of particles in order to accurately predict the ensemble primary electron behavior. Inherent to these methods is the statistical noise that stem from an insufficient number of particles used. Additionally, these methods often have prohibitively lengthy simulation times. These limitations support the current effort's development of a method which eliminates the need to follow discrete particles while still explicitly preserving the magnetic mirror phenomena.

A technique will be developed to determine the continuous, quasi one-dimensional primary electron density along a single magnetic field line. The primary electron population collisions with neutrals tend to induce a "leak" from the magnetic mirror as particles enter the loss cone through velocity space diffusion. After transient collision processes, the normalized density profile will be shown to converge to a single profile. Further, the reduction factor, or the fraction of particles lost between collision events, becomes constant due to the invariance of the normalized density. In ion thrusters and other low-β devices, the collisional mixing is facilitated by the elastic scattering of the primary electrons with the background neutrals, the fastest collision timescale[62]. Since the primaries travel through a quasi-neutral plasma, Coulomb effects are assumed to be negligible. This assumption is also supported by the primaries' relatively large kinetic energy compared to the plasma potential variation throughout the domain [68].

A.1 Methodology

Consider the magnetic field, shown in Figure (A.1), between two aligned dipoles spaced a distance $2L$ apart given by Equation (A.1):

$$B(x) = \frac{\mu_0 m}{2\pi}\left(\frac{1}{|x+L|^3} + \frac{1}{|x-L|^3}\right) \tag{A.1}$$

where m is the magnetic dipole moment. The boundaries, or loss surfaces, are a distance D from either side of the center as seen in Figure A.1. If undisturbed, a single electron within this field oscillates between the poles assuming its velocity vector is exterior to the loss cone. Assuming that the invariance of the magnetic moment is applicable, the angle of the loss cone is calculated from the initial conditions and is given by Equation (A.2), where ξ is the initial position of the charged particle[25, 45]. As a point of clarification, the variable ξ is used to distinguish the insertion points, but it occupies the same spatial dimension as x. If instead of a single particle, an isotropic distribution of monoenergetic particles were initialized at a given position, marked as the "Insertion Point", (ξ) in Figure A.2, the particles within the loss cone would be lost within one transit across the field line. The mirror configuration traps the remaining particles of the distribution. The velocity space volume confined along the the field lines can be calculated yielding the line density profile such as that shown in Figure A.2.

$$sin^2(\theta_L(\xi)) = \frac{B(\xi)}{B_{max}} \tag{A.2}$$

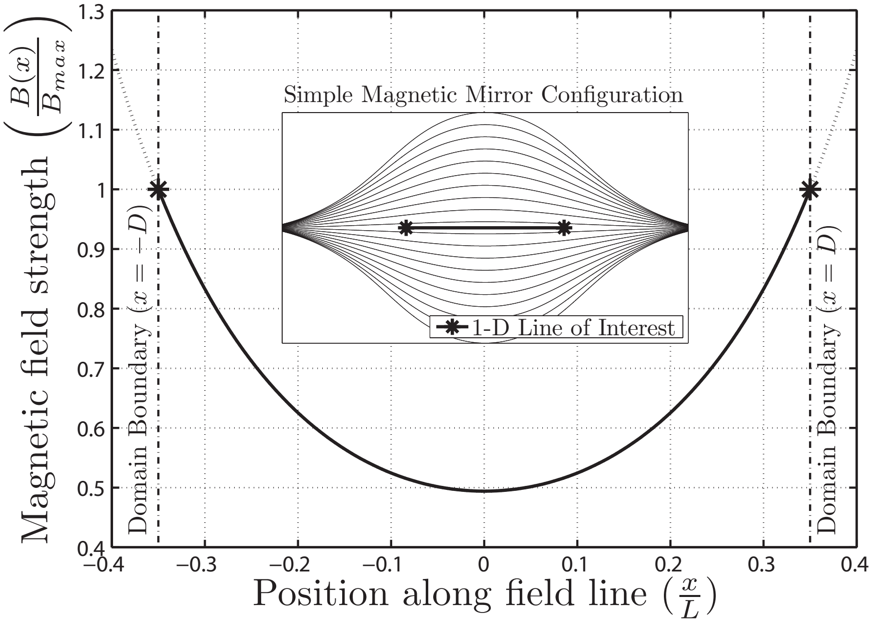

Figure A.1: 1-D test field for quasi-equilibrium analysis. Note that the distance between dipoles is $2L$ while the domain under consideration is $2D$.

Equation (A.3) calculates the fraction of particles retained from the initial distribution through magnetic confinement. This confinement factor, $f_c(\xi)$, is a function of the insertion location and is calculated from the velocity space volume exterior to the loss cone. Note that the distribution of particle speeds does not effect $f_c(\xi)$. As the particles travel toward the regions of higher magnetic field strength, labeled "exterior" in Figure A.2, the population becomes depleted as particles are reflected. In contrast, the entire trapped velocity space exists within the "interior" region. Accounting for this depletion yields the density profile along the field line. These conditions are graphically shown in Figure A.2 for an arbitrary insertion point, ξ.

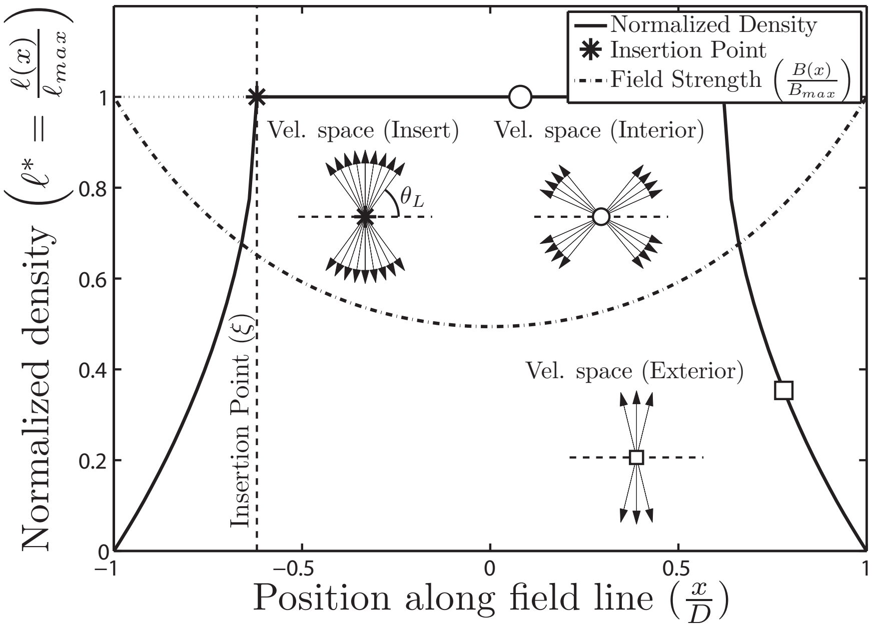

Figure A.2: Density profile that results from an isotropic distribution of particles injected at position ξ. The velocity space overlays show the behavior of particles along various points of the magnetic field line.

$$\begin{aligned} f_c(\xi) &= \frac{2\int_0^{2\pi}\int_{\theta_L(\xi)}^{\pi/2}\int_0^{\infty} f(v)v^2 sin(\theta)\mathrm{d}v\mathrm{d}\theta\mathrm{d}\phi}{4\pi\int_0^{\infty} f(v)v^2\mathrm{d}v} \\ &= cos\left(\theta_L(\xi)\right) \\ &= \sqrt{1-\frac{B(\xi)}{B_{max}}} \end{aligned} \tag{A.3}$$

In typical electron bombardment discharge conditions, the highest frequency collision is the elastic collision with the background neutrals by two orders of magnitude. Therefore, this is the main mixing mechanism for the primaries trapped within the field line. For this particular exercise, assume that the adjacent field lines have a similar density, thus allowing the assumption that the elastic collisions can be modeled as a redistribution of particles. This mixing process is

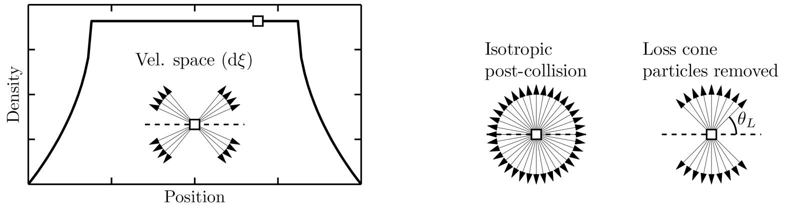

(**1**) Particles in a differential element (dξ)

(**2**) Vel. space diffusion & loss

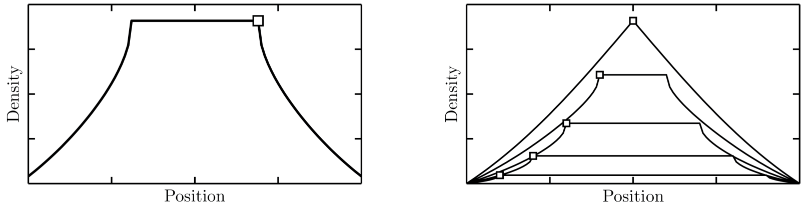

(**3**) Redistribution of (dξ) along field line

(**4**) Integration over all (dξ)'s

Figure A.3: Graphic series depicting the thermalization process. (**1**) Particles within a differential element are isolated. (**2**) Differential population undergoes velocity space diffusion. Particles that enter the loss cone are lost to the domain boundaries. (**3**) Remaining particles are redistributed along the field line based on the original position of the differential element. (**4**) Differential profiles are integrated to find the post-collision profile. Profiles in (**4**) are not normalized.

summarized in Figure A.3. The differential length in Figure A.3 represent a population of primary electrons to be redistributed after a collision timescale. The now isotropic differential population loses particles through the loss cone while trapped particles traverse the field line producing a truncated density profile similar to that shown in Figure A.2. Each element is summed together to yield the post-collision profile. Note that the loss of particles from the redistribution is the primary challenge for magnetic mirror confinement.

Since density profiles for a given ξ are geometrically similar, normalized truncated profiles can be developed for all possible insertion positions. The initial profile in Figure A.2, for example, can be expressed as $\ell_0(x) = \widetilde{\ell}_0 \ell_0^*(x)$, where the scalar $\widetilde{\ell}$ is the scale factor or maximum density value of a given profile, and the starred function, $\ell_0^*(x)$ is the normalized density profile such that $\{\ell^*(x) \epsilon [0, 1]\}$. An important normalized profile is the "insertion shape function" which yields

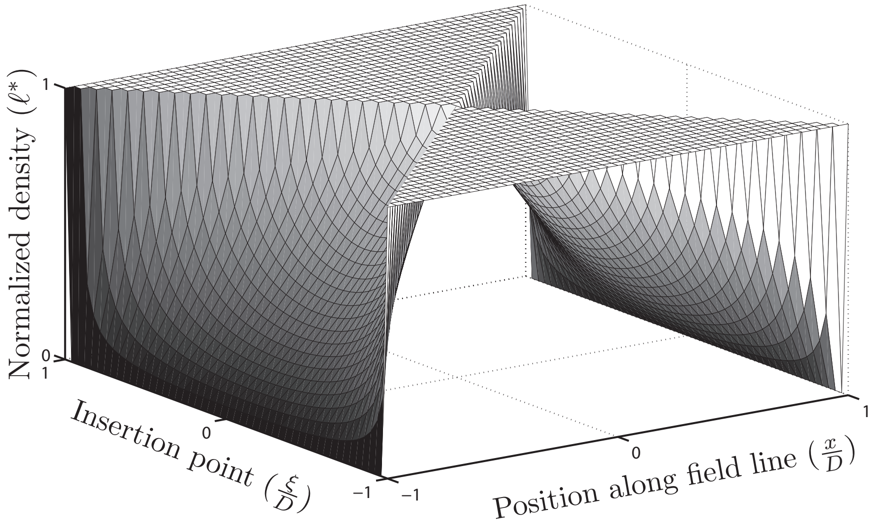

Figure A.4: Insertion shape functions, $\ell^*(x,\xi)$, calculated from Equation (A.1) yield the normalized distribution along x given an insertion point ξ.

the density along x for an insertion point, ξ. For a magnetic field strength profile with a single local minimum, such as the one currently considered, the insertion shape function, $\ell^*(x,\xi)$, is given by Equation (A.4). Using this expression, the magnetic field considered in Figure (A.1) generates the surface shown in Figure A.4. Equation (A.4) must be modified if the magnetic field strength has a local maximum that occurs in the interior region. In such case, particles would undergo an exclusion process allowing certain velocity vectors to pass through the local maximum based on the insertion point.

$$\ell^*(x,\xi) = \begin{cases} 1 & \text{if } B(\xi) \geq B(x) \\ 1 - \sqrt{\frac{B(x)-B(\xi)}{B(x)\left(1-\frac{B(\xi)}{B_{max}}\right)}} & \text{if } B(\xi) < B(x) \end{cases} \tag{A.4}$$

Using Equations (A.4) & (A.3) along with the initial electron density, the resulting profile after a single thermalization event can be calculated using the process outlined in Figure A.3. To begin, the differential element, dξ, at location

$x = \xi$ is taken from the previous density profile. The number of particles within this differential element is re-released at ξ with an isotropic distribution. Of these particles, the remaining particles trapped from $\mathrm{d}\xi$ is:

$$N_{\mathrm{d}\xi}(\xi) = \ell_0(\xi) f_c(\xi) \mathrm{d}\xi \tag{A.5}$$

This population also has an insertion shape function governed by Equation (A.4). To find the scale factor of the shape function, the differential profile is integrated and set equal to Equation (A.5). Because this scale factor, $\widetilde{\ell}_{\mathrm{d}\xi}(\xi)$, is constant with respect to the position, x, it can be easily solved for as seen in Equation (A.6).

$$\begin{aligned} N_{\mathrm{d}\xi}(\xi) &= \widetilde{\ell}_{\mathrm{d}\xi}(\xi) \int \ell^*(x,\xi)\mathrm{d}x \\ \widetilde{\ell}_{\mathrm{d}\xi}(\xi) &= \frac{N_{\mathrm{d}\xi}(\xi)}{\int \ell^*(x,\xi)\mathrm{d}x} = \frac{\ell_0(\xi) f_c(\xi)\mathrm{d}\xi}{\int \ell^*(x,\xi)\mathrm{d}x} \end{aligned} \tag{A.6}$$

Note that the differential scale factors, $\widetilde{\ell}_{\mathrm{d}\xi}(\xi)$, contain the history from the previous profile, $\ell_0(x)$. These differential maximum values can then be used in conjunction with the shape function given of Equation (A.4) to determine each differential element's contribution to the post-collision profile (Figure A.3 (4)). The curves are integrated using Equation (A.7) which gives the complete post-collision profile. This is for a given magnetic field and pre-collision profile. Here, the equations are generalized using $m-1$ and m. The bracketed quantity in the integrand is simply the differential scale factor, $\widetilde{\ell}_{\mathrm{d}\xi}(\xi)$, calculated in Equation (A.6)

$$\ell_m(x) = \int \left\{ \frac{\ell_{(m-1)}(\xi) f_c(\xi)}{\int \ell^*(x,\xi)\mathrm{d}x} \right\} \ell^*(x,\xi)\mathrm{d}\xi \tag{A.7}$$

A.2 Results

Equation (A.7) does not have an analytical solution and must be solved numerically. The results presented here use a simple trapezoid scheme executed in MATLAB. By recursively solving Equation (A.7), the dynamic behavior of successive collision steps can be seen. These give the density profiles as the magnetic mirror loses particles. Interestingly, the normalized profiles begin to coincide to a single function as shown in Figure A.5. This convergence of the normalized profile to a single curve is unexpected, yet is physically representative of the expected profile shape. That is, the maximum confinement is sustained in the region of weakest magnetic field. Figure A.5 shows that the transient profiles are damped within a few collision time steps. The final profile is independent of the initial profile.

As a consequence of the normalized profile's congruence, Equation (A.8) shows that the decay in the maximum plasma density value also becomes constant. Here the "m-1" and "m" profiles are expressed as the product of a scale factor and the normalized profile. Because the normalized profile converge to a solution, both normalized profiles are replaced by the converged profile denoted by, $\ell^*_\infty(x)$. By integrating both profiles along the field line, the reduction fraction between thermalization timescales is found to be independent of time. By extension, the reduction rate of total particles in the mirror trap is also independent of time as seen in Equation (A.8). Figure A.6 shows that the reduction fraction for successive collision timescales does indeed become constant. Similar to the normalized profile, the quasi-equilibrium reduction fraction undergoes a brief transient behavior and is then independent of the initial condition.

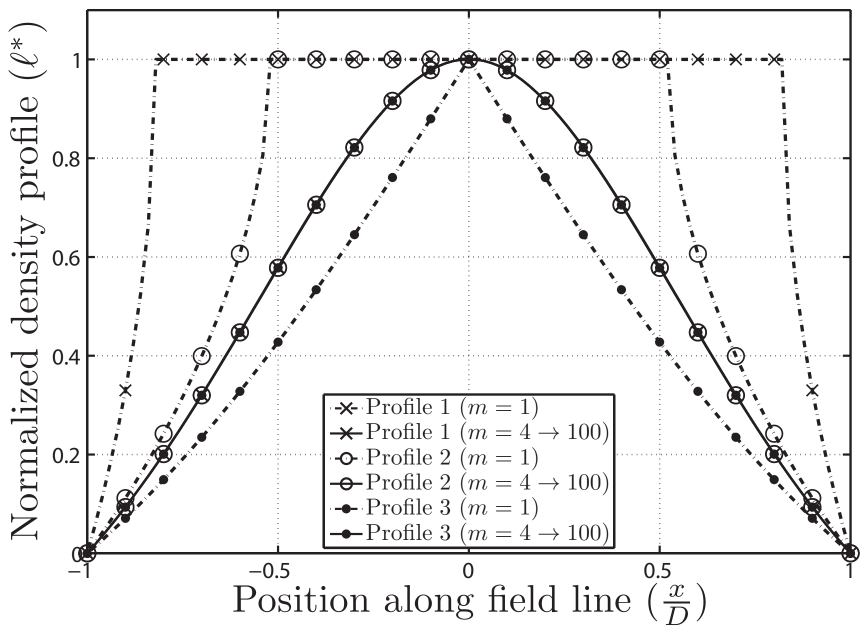

Figure A.5: Normalized density profile evolution for three separate initial condition profiles. The profiles converges after a few thermalization cycles regardless of the initial profile. The converged curve shows the invariance through 100 recursions. Markers are used for distinction and do not reflect the resolution.

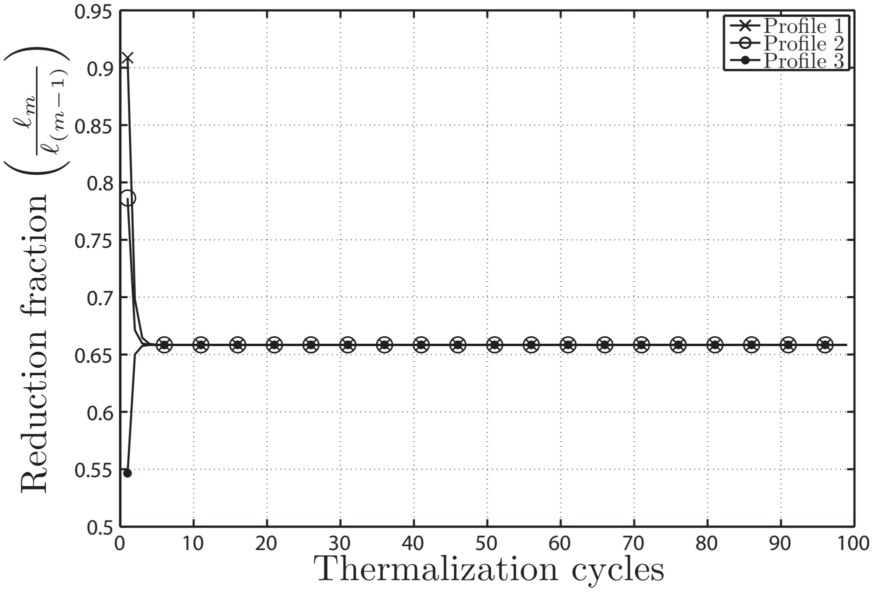

Figure A.6: Reduction fraction between successive thermalization cycles. As seen in Equation (A.8), the convergence of the normalized density profiles lead to a constant reduction fraction.

$$\begin{aligned}
\widetilde{\ell}_m \ell^*_\infty(x) &= \int \left(\frac{\widetilde{\ell}_{(m-1)} \ell^*_\infty(\xi) f_c(\xi)}{\int \ell^*(x,\xi)\mathrm{d}x} \right) \ell^*(x,\xi)\mathrm{d}\xi \\
\frac{\widetilde{\ell}_m}{\widetilde{\ell}_{(m-1)}} &= \frac{\int \left(\int \left(\frac{\ell^*_\infty(\xi) f_c(\xi)}{\int \ell^*(x,\xi)\mathrm{d}x} \right) \ell^*(x,\xi)\mathrm{d}\xi \right) \mathrm{d}x}{\int \ell^*_\infty(x)\mathrm{d}x} \\
&= \frac{\widetilde{\ell}_m \int \ell^*_\infty(x)\mathrm{d}x}{\widetilde{\ell}_{(m-1)} \int \ell^*_\infty(x)\mathrm{d}x} = \frac{N_m}{N_{(m-1)}} \neq f(m) \qquad \text{(A.8)}
\end{aligned}$$

Commonly in these devices, the primary electrons are continuously injected into the discharge chamber from an emitter. In such a case, this technique can be employed by using an injection profile to supplement Equation (A.7). This profile depends on the emitter's current as well as the injection location(s). Some particles from the emitter will be lost immediately, thus the injection profile is calculated using Equations (A.3) & (A.4). The injection profile is then simply added to Equation (A.7) before integration. The equilibrium profile will look similar to Figure A.5, but will depend on the injection location(s). The quantity of particles lost at equilibrium will then of course match the input current from the primary electron source.

APPENDIX B

Comparison of Charged Particle Tracking Methods

Five particle tracking methods are compared for their ability to accurately predict particle trajectories and conserve energy. The trajectory integrators include: the Boris particle tracking method (a widely used method for charged particles), the classical fourth-order Runge-Kutta (a ubiquitous high-order integrator), Störmer-Verlet as a partitioned Runge-Kutta (a second-order symplectic integrator), fourth-order Gauss Runge-Kutta (a fourth-order symplectic integrator), and Wirz's modified Boris method (a new particle tracker constructed to handle large magnetic gradients). The present study will distinguish the features of symplectic methods with popular classical methods, as well as introduce and benchmark Wirz's algorithm against well-established methods. The symplectic methods are known for their energy conservation properties while these classical "Newtonian" methods are typically more easily implemented due to their explicit nature. Wirz's modified Boris method is shown to strike the balance between the two classes with explicit implementation and total energy conservation.

B.1 Introduction

Particle simulations are in theory the most accurate form of simulation, but are notoriously resource intensive. Their utility, however, lies in their extension to developing simpler models and understanding detailed behavior and because of these qualities, particle simulations are used in a wide array of disciplines. For example, individual particle tracking can provide direct trajectory information as is done in space plasmas[69, 70]. Through particle-in-cell/Monte Carlo (PIC/MC) techniques, full plasma simulations can be developed[67, 71]. Full PIC/MC simulations a provide an illustration of statistical behavior that can be used to benchmark simpler theories and models such as is commonly done in plasma sheath studies, where the physics is less well understood[72, 73, 74]. Particle simulations can also act as an input to continuum fluid simulations such as is done in ion propulsion modeling[21], plasma processing simulations[75].

At the heart of every good particle simulation is an efficient particle tracking algorithm. Conserving particle energy is imperative in determining the particle's interaction with its environment, be it boundaries in the case of sputtering or the background gas in the case of ionization. Additionally, because of the sheer number of particles necessary to obtain a statistical significant sample, particle tracking methods are required to be computationally efficient.

The current effort will compare several particle tracking method's performance in different magnetic field configurations. The methods compared will fall into two categories: Newtonian or Hamiltonian.

The Newtonian methods chosen are all explicit and operate on the Newtonian equations of motion, in this particular case the Lorentz force. These methods are the common (or classical) fourth-order Runge-Kutta integrator, the Boris integrator[76, 77], and a modified Boris integrator developed by Wirz[21]. Wirz's method has not been previously benchmarked against other more established methods, but has been successfully implemented in ion thruster models[78]. This method was observed to be less prone to particle loss than the Boris tracker and will be used to investigate miniature plasma sources in future studies.

The Hamiltonian methods, also known as symplectic integrators, have the property of controlling errors in energy and thus have gained recent popularity in various fields [70]. These methods integrate the Hamiltonian equations of motion and are typically implicit. The two methods chosen for this study are the Störmer-Verlet as a partitioned Runge-Kutta[79] and the fourth-order Gauss method[79, 70, 80]. Both the Newtonian and Hamiltonian methods will be evaluated on their ability to control errors in energy as well as their ability to adequately predict particle trajectories.

Each integration method will be put through the same series of tests evaluating their ability to predict different features of charged particle motion in magnetic fields. The first test will be a simple cyclotron motion of an electron in a uniform magnetic field. The second test will calculate a proton's trajectory through Earth's dipole. This test was performed by MacKay and Yugo to compare the common fourth-order Runge-Kutta and the symplectic fourth-order Gauss method[70, 80]. The final experiment will evaluate that integrators ability to conserve energy and track a particle in a highly non-uniform magnetic mirror configuration.

B.2 Integration Methods

The integration methods considered for this study are outlined below. The Newtonian integrators considered here are all explicit and demonstrate the necessary stability and accuracy to track particle trajectories in a magnetic field. These three methods are computationally efficient, but will gradually deviate from it's original energy level. The symplectic integrators are constructed to preserve the symplectic structure of phase space in Hamiltonian systems[81]. The two symplectic methods presented below are both Runge-Kutta methods. Runge-Kutta methods must be implicit in order to maintain their symplectic structure, thus implementing a symplectic integrator comes at the cost of computation time[82]. Particle trajectories calculated with this method will still have errors in energy, however, the error will be bounded. One should note that although, the tests neglect electric fields, they are still included in the formulations shown below for posterity.

B.2.1 Newtonian Integrators

$$\begin{aligned} \frac{d\mathbf{v}}{dt} &= \frac{q}{m}\left(\mathbf{E} + \mathbf{v} \times \mathbf{B}\right) \\ \frac{d\mathbf{x}}{dt} &= \mathbf{v} \end{aligned} \tag{B.1}$$

The three Newtonian integrators, the classical fourth-order Runge-Kutta, Boris particle tracking method, and Wirz's modified Boris integrator, all operate on the Newtonian equations of motion given in Equation (B.1). The time step, Δt, is calculated at each position location to be some percentage, ε, of the cyclotron period, $1/\omega_c$. This is shown in Equation (B.2).

$$\Delta t = \frac{\varepsilon}{\omega_c} = \varepsilon \frac{m}{|q||\mathbf{B}|} \tag{B.2}$$

B.2.1.1 Classical Fourth Order Runge-Kutta

Runge-Kutta methods are described by the Butcher tableau shown in Table B.1. These coefficients are used with Equation (B.3) to calculate the next step. The common fourth-order Runge-Kutta is shown in Table B.2. This is an explicit method that requires four function evaluations per time step. This method is a general ODE integrator and was not been developed for charged particle trajectory calculations.

$$\begin{aligned} k_i &= f\left(t_n + c_i\Delta t, y_n + \Delta t \sum_{j=1}^{s} a_{ij}k_j\right) \\ y_{n+1} &= y_n + \Delta t \sum_{i=1}^{s} b_i k_i \end{aligned} \tag{B.3}$$

B.2.1.2 Boris Particle Tracking Method

The Boris particle tracker[76, 77] takes the velocity and displaces the calculation by $\Delta t/2$ to solve the position and velocity equations on a staggered grid as shown in Figure B.1. This effectively applies a position averaged impulse and advances

Table B.1: Runge-Kutta Butcher tableau

c_1	a_{11}	a_{12}	$\dots$	a_{1s}
c_2	a_{21}	a_{22}	$\dots$	a_{2s}
$\vdots$	$\vdots$	$\vdots$	$\ddots$	$\vdots$
c_s	a_{s1}	a_{s2}	$\dots$	a_{ss}
	b_1	b_2	$\dots$	b_s

Table B.2: Common fourth-order RK

1	0	0	0	0
$^1/_2$	$^1/_2$	0	0	0
$^1/_2$	0	$^1/_2$	0	0
1	0	0	1	0
	$^1/_6$	$^1/_3$	$^1/_3$	$^1/_6$

the particle in time. The change in velocity is applied by first applying half of the electric field impulse, going through the gyromotion from the magnetic field, then applying the other half of the electric field impulse. This process is shown in Equation (B.4).

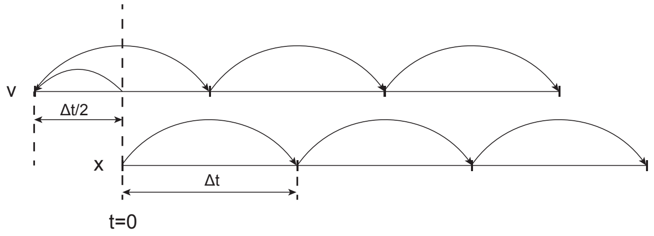

Figure B.1: Schematic of staggered spatial and velocity grid used in the Boris particle pushing method.

The methodology used in Boris decouples the magnetic field contribution from the electric field effect. Further, from the cross velocity term seen in the magnetic field portion of Equation (B.4), additional accuracy is obtained by using the average velocity for the magnetic impulse. Although, this step seems implicit, $\mathbf{v}_+$ can be solved for analytically to render the Boris integrator an explicit method. This method is second-order, however, it has been specifically developed for charged particles and adds additional accuracy to the magnetic gyration term, the term most likely to produce error.

$$\begin{aligned} \mathbf{v}_- &= \mathbf{v}_{n-{}^{\Delta t}/_2} + \left(\frac{q\Delta t}{2m}\right)\mathbf{E} \\ \frac{\mathbf{v}_+ - \mathbf{v}_-}{\Delta t} &= \left(\frac{q}{m}\right)\left(\frac{\mathbf{v}_+ + \mathbf{v}_-}{2} \times \mathbf{B}\right) \\ \mathbf{v}_{n+{}^{\Delta t}/_2} &= \mathbf{v}_+ + \left(\frac{q\Delta t}{2m}\right)\mathbf{E} \end{aligned} \tag{B.4}$$

$$\frac{\mathbf{x}_{n+1} - \mathbf{x}_n}{\Delta t} = \mathbf{v}_{n+{}^{\Delta t}/_2} \tag{B.5}$$

B.2.1.3 Wirz's Modified Boris Method

Wirz's method removes the staggered-grid features from Boris and carries out the position and velocity solution on an aligned temporal grid[21]. The method is based on obtaining better estimations for the magnetic field at each time step. This is accomplished by using a corrected magnetic field values at the midpoint. The schematic for this process is shown in Figure B.2. Wirz's method use the same partitioning of the electric field as Boris, but uses a predictor/corrector scheme in place of the averaged velocity used in Equation (B.4).

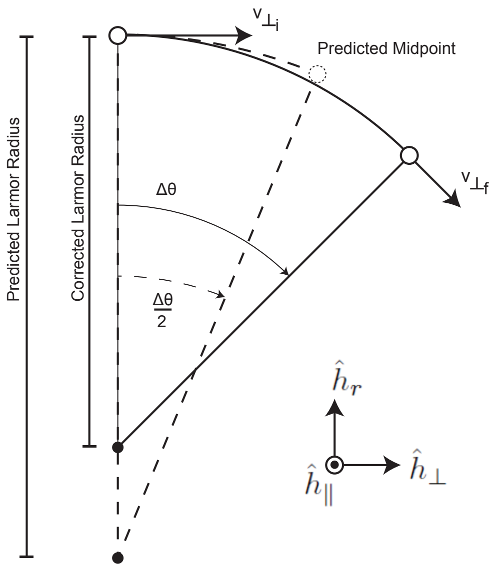

Figure B.2: Illustration of Wirz's predictor/corrector method. The magnetic field value calculated at the midpoint is used to execute the corrected gyromotion.

In practice, this is achieved by establishing a coordinate system per Equation (B.6). The radial unit vector, $\hat{h}_r$, is multiplied by the particle sign to automatically prescribe the gryomotion's direction. Changes in position are calculated with Equation (B.7), where the change in angle and Larmor radius, $\Delta\theta$ and r_L, are modified for both the predictor and corrector step.

$$\hat{h}_{\parallel} = \frac{\mathbf{B}}{|\mathbf{B}|};\ \hat{h}_{\perp} = \frac{\mathbf{v} - (\mathbf{v} \cdot \hat{h}_{\parallel})\hat{h}_{\parallel}}{|\mathbf{v} - (\mathbf{v} \cdot \hat{h}_{\parallel})\hat{h}_{\parallel}|};\ \hat{h}_r = \frac{q}{|q|}(\hat{h}_{\parallel} \times \hat{h}_{\perp}) \tag{B.6}$$

$$\Delta x_{\parallel} = \Delta t(\mathbf{v} \cdot \hat{h}_{\parallel})\hat{h}_{\parallel} \quad ; \quad \Delta x_{\perp} = r_L sin(\Delta\theta)\hat{h}_{\perp} \quad ; \quad \Delta x_r = -r_L[1 - cos(\Delta\theta)]\hat{h}_r \tag{B.7}$$

where:

$$r_L = \frac{m\mathbf{v}_{\perp}}{|q||\mathbf{B}|} \quad ; \quad \Delta\theta = \omega_c$$

The initial velocity, $\mathbf{v}_n$, is used to calculate the first intermediate velocity, $\mathbf{v}_-$, by applying the first electric half impulse (Equation (B.8)). $\mathbf{v}_-$ is then used to calculate a predicted midpoint (Equation (B.7)). By using $\Delta\theta/2$, a spatially averaged magnetic field value can be predicted. The predicted B-field value is then used to calculate a corrected coordinate system and $\Delta\theta$ which is used to update the velocity using Equation (B.9). The final velocity is calculated by applying the remaining half of the electric impulse. The position vector is updated by applying Equation (B.7) with a full time step ($\Delta\theta$), the spatially averaged magnetic field ($\mathbf{B}_{corr}$), and the updated velocity ($\mathbf{v}_{n+1}$).

$$\mathbf{v}_- = \mathbf{v}_n + \left(\frac{q\Delta t}{2m}\right)\mathbf{E} \tag{B.8}$$

$$\mathbf{v}_+ = (\mathbf{v}_-)_{\parallel} + |(\mathbf{v}_-)_{\perp}|\left(cos(\Delta\theta)\hat{h}_{\perp} - sin(\Delta\theta)\hat{h}_r\right) \tag{B.9}$$

$$\mathbf{v}_{n+1} = \mathbf{v}_{+} + \left(\frac{q\Delta t}{2m}\right)\mathbf{E} \tag{B.10}$$

B.2.2 Symplectic Integrators

Symplectic integrators are used on Hamiltonian systems to preserve the geometric properties of the system[79]. Numerically, this is manifested in the phase space variables canonical momentum and the generalized coordinate, $\mathbf{p}$ and $\mathbf{q}$ respectively. These state variables evolve such that the total energy or the Hamiltonian, $\mathscr{H}$, is conserved. The Hamiltonian and its equations of motion are given in Equation (B.11) and Equation (B.12) respectively. Generally speaking, symplectic integrators are implicit requiring an iterative solution at each time step. For this study, all implicit equations are solved using fixed point iteration. Using a non-symplectic integrator on Equation (B.12), such as those given in Section B.2.1, will lead to large errors in total energy[81]. It should be noted that the electromagnetic field values act on the Hamiltonian system through their potential counterparts, the electric potential (V) and the magnetic vector potential ($\mathbf{A}$). Additionally, time steps for these methods are calculated using Equation (B.2).

$$\begin{aligned} &\mathscr{H} = \mathbf{p}\cdot\mathbf{v} - \frac{1}{2}m\left(\mathbf{v}\right)^2 + qV - q\left(\mathbf{v}\cdot\mathbf{A}\right) \\ &\text{where:} \\ &\mathbf{v} = \frac{\mathbf{p} - q\mathbf{A}}{m} \end{aligned} \tag{B.11}$$

$$
\begin{aligned}
\frac{d\mathbf{p}}{dt} &= -\frac{\partial \mathscr{H}}{\partial \mathbf{q}} = -q\frac{\partial V}{\partial \mathbf{q}} + \frac{q}{m}\left[\frac{\partial \mathbf{A}}{\partial \mathbf{q}}\right]\cdot(\mathbf{p}-q\mathbf{A}) \\
\frac{d\mathbf{q}}{dt} &= \frac{\partial \mathscr{H}}{\partial \mathbf{p}} = \frac{\mathbf{p}-q\mathbf{A}}{m}
\end{aligned}
\tag{B.12}
$$

B.2.2.1 Störmer-Verlet as a Partitioned Runge-Kutta Method

The symplectic Störmer-Verlet method takes the form of a partitioned Runge-Kutta for an autonomous system. In a partitioned Runge-Kutta method, each equation of motion in the Hamiltonian system is solved with a separate Runge-Kutta method. The two methods are combined in the calculation of the Runge-Kutta coefficients, k_i and l_i. The general form of the partitioned Runge-Kutta is given in Equation (B.13) and Equation (B.14).

$$
\frac{d\mathbf{y}}{dt} = f(\mathbf{y},\mathbf{z}) \quad ; \quad \frac{d\mathbf{z}}{dt} = g(\mathbf{y},\mathbf{z}) \tag{B.13}
$$

$$
\begin{aligned}
k_i &= f\left(\mathbf{y}_n + \Delta t\sum_{j=1}^{s} a_{ij}k_j \ , \ \mathbf{z}_n + \Delta t\sum_{j=1}^{s} \hat{a}_{ij}l_j\right) \\
l_i &= g\left(\mathbf{y}_n + \Delta t\sum_{j=1}^{s} a_{ij}k_j \ , \ \mathbf{z}_n + \Delta t\sum_{j=1}^{s} \hat{a}_{ij}l_j\right) \\
\mathbf{y}_{n+1} &= \mathbf{y}_n + \Delta t\sum_{j=1}^{s} b_i k_i \quad ; \quad \mathbf{z}_{n+1} = \mathbf{z}_n + \Delta t\sum_{j=1}^{s} \hat{b}_i l_i
\end{aligned}
\tag{B.14}
$$

The Butcher tableau for the two equations of motion are given in Table B.3 and Table B.4. This method is second-order and in practice is quasi-implicit. That is, iteration is only required on a single equation rather than the whole system. Upon completion of the first iteration, the two Runge-Kutta methods can be manipulated to explicitly solve for the remaining Runge-Kutta coefficients.

Table B.3: Momentum RK ($\hat{a}_{ij}, \hat{b}_i$)

$$\begin{array}{c|cc} 0 & 0 & 0 \\ 1 & {}^1/_2 & {}^1/_2 \\ \hline & {}^1/_2 & {}^1/_2 \end{array}$$

Table B.4: Position RK (a_{ij}, b_i)

$$\begin{array}{c|cc} {}^1/_2 & {}^1/_2 & 0 \\ {}^1/_2 & {}^1/_2 & 0 \\ \hline & {}^1/_2 & {}^1/_2 \end{array}$$

B.2.2.2 Fourth Order Gauss Method

The fourth-order Runge-Kutta Gauss method's Butcher Tableau is given in Table B.5. This method was used by MacKay and Yugo to demonstrate the benefits of symplectic methods over generic methods, namely the classical Runge-Kutta[70, 80]. This method is fourth-order and is fully implicit. In fact, it can be shown that any Runge-Kutta Gauss method maintains the symplectic structure [82].

B.3 Results and Discussion

To compare the five numerical methods, three test cases will be performed highlighting different features of a magnetic field: a uniform field, a dipole field, and a magnetic mirror at the centimeter scale. The uniform magnetic field gives a simple test bed to compare the methods' basic ability to execute a gyromotion. The dipole field uses a proton in Earth's magnetic field for the simulation. Two experiments will be conducted. The first of these experiments is a proton that

Table B.5: Fourth-order Gauss Runge-Kutta method

$$\begin{array}{c|cc} \frac{1}{2} - \frac{\sqrt{3}}{6} & \frac{1}{4} & \frac{1}{4} - \frac{\sqrt{3}}{6} \\ \frac{1}{2} + \frac{\sqrt{3}}{6} & \frac{1}{4} + \frac{\sqrt{3}}{6} & \frac{1}{4} \\ \hline & \frac{1}{2} & \frac{1}{2} \end{array}$$

will have an initial velocity along the equator. The second experiment is a particle with a velocity angled toward the pole. This introduces a third dimension into the motion. The final experiment will take two magnetic dipoles spaced 3 cm apart. This simulates a high-gradient magnetic field that will be of interest in future studies of small scale plasma sources.

For a given test case, each method was given the same ε time step parameter irrespective of the methods order. ε was chosen sufficiently small such that all methods displayed qualitatively similar solutions. Additionally, care was taken not to allow the particle to reach high gradient regions. Particles entering this region would often experience different total times due to large changes in magnetic field and consequently cyclotron frequency, ω_c.

B.3.1 Uniform Magnetic Field

The uniform magnetic field provided a preliminary comparison for the five methods. The particles were subjected to a 1 T magnetic field and given an initial velocity of 1 m/s. Trajectories produced by all methods showed the same qualitative behavior (Figure B.3(a)) and had an approximate error in Larmor radius of 0.01%. Figure B.3(b) shows the relative error in conserving energy of the five methods. The Störmer-Verlet shows the most stable upper bound in error, but also the highest error while the other methods monotonically increase.

Because of the uniform magnetic field, the benefit of the spatially averaged magnetic field in Wirz's method is negated, thus Wirz's method reduces essentially into a first-order method. The fourth-order methods, the Gauss Runge-Kutta and the classical Runge-Kutta in Figure B.3(b) exhibit the best energy conservation properties.

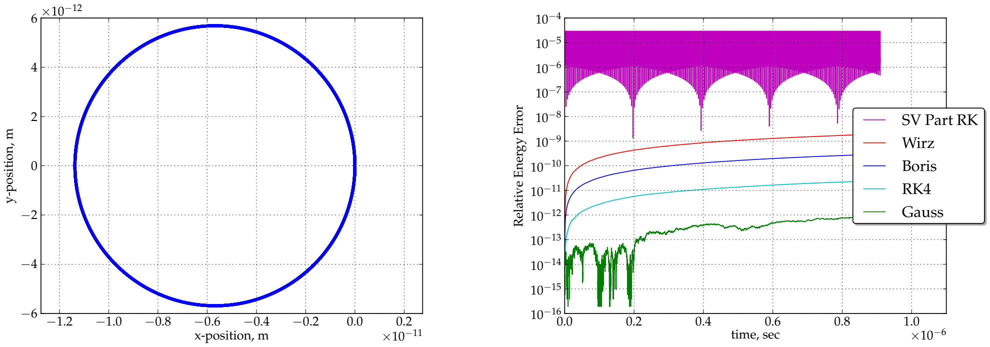

(a) Particle Trajectory (b) Method Energy Error

Figure B.3: B.3(a) An electron with an initial velocity of 1 m/s in a 1 T magnetic field pointing out of the page. All methods display the same qualitative behavior and roughly a 0.01% error in Larmor radius. B.3(b) Relative error in energy for the five different methods shown in a semi-log plot. The methods with the best performance in conserving energy are the two fourth-order methods.

B.3.2 Earth's Magnetic Dipole

As mentioned previously, the experiment of a proton in Earth's magnetic dipole field has been performed with the classical Runge-Kutta and the fourth-order Gauss methods[70, 80]. The current study uses the same baseline parameters as MacKay[70] and is extended to all five methods for two separate cases: equatorial and pitched initial velocity. The equatorial velocity test will demonstrate the gyroperiod as well as the magnetic gradient induced curvature drift, while the pitched test will introduce a magnetic mirroring effect at the poles.

B.3.2.1 Planar Motion (Equatorial Initial Velocity)

The particles simulated in Figure B.4 have an initial position of five Earth radii with respect to the dipole center, however the coordinate system shown in Figure B.4(a) has the particles initial position as the origin. The initial energy of each particle is 10 MeV along the equator. The expected trajectory is a cyclotron motion superimposed on an azimuthal drift due to the gradient in magnetic field. The appropriate equatorial procession is achieved by all methods.

The percent error in energy is shown in Figure B.4(b). The nature of each of the methods begins to materialize in the non-uniform field of the dipole field. The Gauss and the Störmer-Verlet methods begin to show an equilibrium bound on the energy error. Naturally, the fourth-order Gauss method shows better conservation than the second-order S-V method. The Boris method and the classical fourth-order Runge-Kutta both show monotonic growth in energy error; however, the Boris method, which is of lower order than the classical RK method, displays better performance. This is expected since the Boris method is specifically developed for charged particles in magnetic fields. Finally, the Wirz method shows the best performance among the other five methods. While not strictly symplectic, the non-uniform field allows the Wirz method to control the conservation of energy by using the spatially averaged magnetic fields.

B.3.2.2 Mirroring Motion (Pitched Initial Velocity)

The second experiment simulates a 27 keV proton that has a 60^o pitch with respect to Earth's equator. The additional energy towards the pole causes three-dimensional motion. In addition to the motions seen in Section B.3.2.1, there is a mirroring motion from the particle reflection at the poles. The resultant motion is a gyromotion superimposed on both a magnetic mirroring oscillation and a curvature drift along the equator. This is seen in Figure B.5(a).

The relative error shown in Figure B.5(b) reveals that the symplectic methods maintain their relative error bound while the classical Runge-Kutta and the Boris method continue to monotonically increases. Thus, it can be concluded

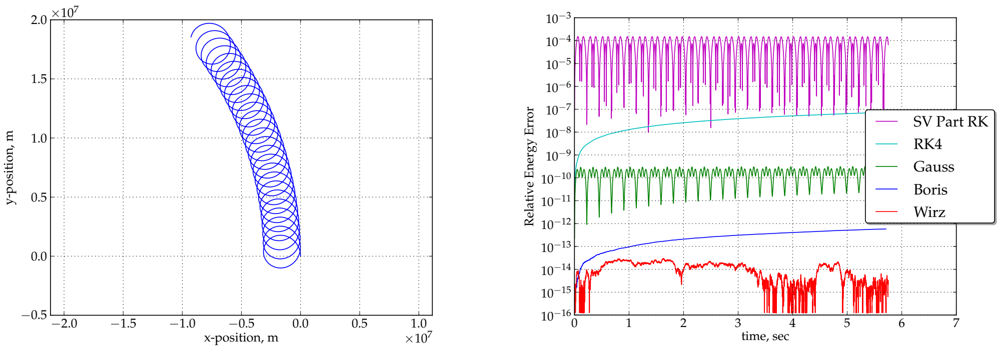

(a) Particle Trajectory

(b) Method Energy Error

Figure B.4: Equatorial proton simulation run for 10,000 time steps (≈ 6 sec simulation time). B.4(a) A 10 MeV proton with an equatorial trajectory. Again, each method showed qualitative similarities. B.4(b) Relative error in energy for the five different methods shown in a semi-log plot. The symplectic structure of the Gauss and the Störmer-Verlet are seen in the upper bound of their energy error. The Boris and classical Runge-Kutta non-symplectic methods show the same trend as in the uniform magnetic field case, while the Wirz methods shows superior performance to all methods due to its spatial averaging.

that symplectic integrators are useful in long time-scale scenarios. Just as in Section B.3.2.1, the Wirz method benefits from the non-uniformity of the magnetic field with its spatial averaging technique.

For this test case, computation times were also compared. Table B.6 shows the absolute time to run the 10^7 time steps in the mirroring experiment as well as the relative time when compared to the Boris method. Both the classical RK4 method and the Wirz method have a similar number of function evaluations and are fully explicit. The implicit methods require iteration and thus take significant more computational time. As mentioned previously, solutions for implicit equations were made using a fixed point iteration method; therefore, the computational time could be reduced greatly by implementing more efficient techniques.

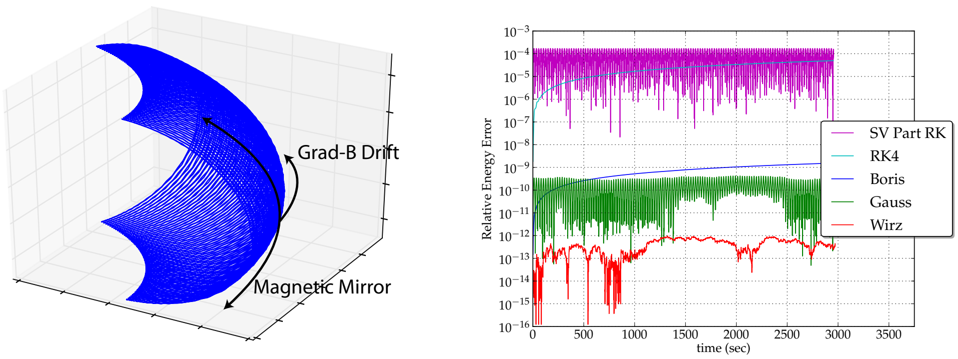

(a) Particle Trajectory

(b) Method Energy Error

Figure B.5: Equatorial proton simulation run for 10,000,000 time steps ($\approx 3,000$ sec simulation time). B.5(a) A 27 keV proton with a pitch angle of 60° with respect to the equator is shown. The trajectory has three fundamental features: gyromotion, magnetic mirroring, and equatorial precision along the equator. Again, each method showed qualitative similarities. B.5(b) The symplectic methods (Gauss and SV) have bounds on the energy error, thus when the simulation is run for long timescales, the symplectic methods show better conservation of energy. The Wirz method, however, is still superior to the other four methods in conserving energy. Additionally, the Wirz method peak error appears to be bound below 10^{-12}.

B.3.3 Magnetic Mirroring on a Miniature Plasma Source Scale.

The final test case is a magnetic mirroring configuration. Two dipoles are placed a distance of 3 cm apart with a dipole strength of 0.238 Am^2. This simulates two 250 mm^3 samarium cobalt magnets. The trajectory for a 20 eV electron is tracked in the confinement region of the magnetic mirror structure. For this experiment, only the Boris method, Gauss integrator, and the Wirz method are considered since the previous test cases showed that the Störmer-Verlet and the classical RK4 prove to have the poorest energy conservation and the longest run times among their respective groups. A sample particle trajectory is shown in Figure B.6(a). Here the particle trajectory is projected onto a two dimensional schematic of the field lines. Just as in the previous cases, Wirz's method continues to display the

Table B.6: Computation time for *Mirroring Motion* experiment (10^7 time steps). All implicit equations solved with fixed point iteration.

Computational Method	Calculation Time	Normalized to Boris
Boris Method	2.36 sec	1.0
Classical RK4	4.82 sec	2.0
Wirz Method	3.98 sec	1.7
Gauss Symplectic	27.82 sec	11.8
Störmer-Verlet	43.24 sec	18.3

best energy conservation performance. Wirz's method will continue to be applied in future work to high gradient magnetic fields.

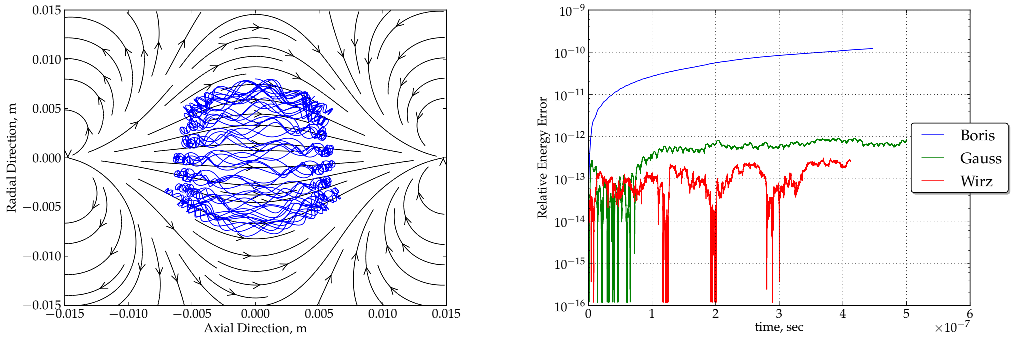

(a) Particle Trajectory

(b) Method Energy Error

Figure B.6: B.6(a) A 20 eV electron trajectory projected onto a schematic of the magnetic mirror configuration. B.6(b) Among these three methods, the Gauss and Wirz method display the best energy conservation. Due to the explicit nature of Wirz's modified Boris method, it is the clear favorite for this scale of magnetic field configuration.

B.4 Conclusion

The five particle integration methods currently examined have all demonstrated the ability to capture the qualitative features of a particle in a magnetic field; however, when conservation of energy is critical, such as in a small scale plasma device, some methods perform better in a given situation. Generally speaking, two classes of integrators have been examined: symplectic (Gauss and Störmer-Verlet) and non-symplectic (Classical Runge-Kutta and Boris integration). For the purposes of this discussion, Wirz's modified Boris method will be mentioned separately. In general, symplectic integrators are constructed using geometric formalism to conserve the Hamiltonian or total energy. This makes them optimal for controlling the error in energy, especially for extended simulations. However, because symplectic integrators are implicit by nature, the computational cost can by much greater to implement these techniques. Non-symplectic integrators, or "Newtonian integrators", can be explicit, thus greatly reducing computational time. Additionally, the accumulation of artificial energy tends to be relatively slow; therefore, for short timescale problems, explicit integrators are generally more efficient to implement.

The new integration method created by Wirz[21] has been benchmarked against the four classical methods mentioned above. The Wirz integrator is constructed to handle high gradients in magnetic cusps by using a predictor/corrector algorithm to determine a spatially averaged field strength. Although the procedure is not constructed in the same geometric formalism as the symplectic integrators, the test cases shown in this study demonstrate that the Wirz integrator is not subject to the monotonic growth in energy error of other non-symplectic methods. In fact, in non-uniform magnetic fields, it often exhibits the best performance among all integration methods. Therefore, Wirz's modified Boris method may be a suitable for high-gradient magnetic fields where conserving energy over the duration of the particle flight is essential. This is the case in any application where the impact energy must be known, such as plasma ionization and ion bombardment. Future studies will work to conserve the magnetic moment, something that is handled relatively poorly by most methods.

References

[1] D. M. Goebel and I. Katz, *Fundamentals of electric propulsion: ion and Hall thrusters.* JPL Space Science and Technology Series, 2008.

[2] N. Hershkowitz, “Sheaths: More complicated than you think,” *Phys. Plasmas*, vol. 12, no. 5, p. 055502, 2005.

[3] N. Hershkowitz, K.-N. Leung, and T. Romesser, “Plasma Leakage Through a Low-β Cusp,” *Phys. Rev. Lett.*, vol. 35, no. 5, pp. 277–180, 1975.

[4] J. Beattie, “XIPS keeps satellites on track,” *The Industrial Physicist*, vol. 6, no. June, pp. 24–26, 1998.

[5] R. Wirz, J. Polk, C. Marrese, J. Mueller, J. Escobedo, and Patrick Sheehan, “Development and Testing of a 3cm Electron Bombardment Micro-Ion Thruster,” in *27th International Electric Propulsion Conference*, (Pasadena, CA), IEPC-01-343, 2001.

[6] R. Wirz and M. Gale, “Miniature Ion Thrusters for Precision Formation Flying,” in *40th AIAA Joint Propulsion Conference*, (Fort Lauderdale, FL), AIAA Paper 2004-4115, July 2004.

[7] R. Wirz and I. Katz, “A Preliminary 2-D Computational Model of an Ion Thruster Discharge Chamber,” in *39th AIAA Joint Propulsion Conference*, (Huntsville, AL), AIAA Paper 2003-5163, July 2003.

[8] J. Mueller, R. Hofer, M. Parker, and J. Ziemer, “Survey of Propulsion Options for Cubesats,” in *57th JANNAF Propulsion Meeting*, pp. 1–56, JANNAF-1425, 2010.

[9] T. A. Trudel, M. M. Micci, U. Student, and E. Design, “Design and Performance Testing of a 1-cm Miniature Radio-,” in *31st International Electric Propulsion Conference*, (Ann Arbor, Michigan), IEPC-09-167, 2009.

[10] P. Reader, “Scale Effects on Ion Rocket Performance,” *Am Rocket Soc. J.*, vol. 32, 1962.

[11] G. Sohl, V. Fosnight, S. Goldner, and R. Speiser, “Cesium electron bombardment ion microthrustors,” in *AIAA, Aerospace Sciences Meeting*, (New York, New York), p. 7, AIAA Paper 67-81, 1967.

[12] A. L. R. C. Weigand, “5-cm Diameter Ion Thruster Development Program Summary,” Tech. Rep. NASA TM X-68110, NASA, 1972.

[13] J. Hyman, “Performance Optimized, Small Structurally Integrated Ion Thruster System,” tech. rep., NASA, 1973.

[14] S. Nakanishi and R. Finke, “9700-Hour Durability Test of a Five Centimeter Diameter Ion Thruster,” *J. Spacecraft Rockets*, vol. 11, p. 560, 1974.

[15] H. R. Kaufman, “Technology of Electron-Bombardment Ion Thrusters,” vol. 36 of *Advances in Electronics and Electron Physics*, pp. 265–373, Academic Press, 1975.

[16] J. Mueller, C. Marrese, J. Wang, and J. Polk, “Design and fabrication of a micro-ion engine,” in *36th AIAA Joint Propulsion Conference*, (Huntsville, AL), AIAA Paper 2000-3264, July 2000.

[17] G. J. Yashko, G. B. Giffin, and D. Hastings, “Design Considerations for Ion Microthrusters,” in *25th International Electric Propulsion Conference*, (Cleveland, OH), IEPC-97-072, 1997.

[18] R. Wirz, “Computational modeling of a miniature ion thruster discharge,” in *41st AIAA Joint Propulsion Conference*, (Tuscon, AZ), AIAA Paper 2005-3887, July 2005.

[19] S. Martin, D. Scharf, R. Wirz, and O. Lay, “Design study for a planet-finding space interferometer,” in *IEEE Aerosp. Conf. Proc.*, pp. 1–19, Ieee, Mar. 2008.

[20] R. W. Conversano and R. E. Wirz, “CubeSat Lunar Mission Using a Miniature Ion Thruster,” in *47th AIAA Joint Propulsion Conference*, (San Diego, CA), AIAA Paper 2011-6083, July 2011.

[21] R. Wirz, *Discharge plasma processes of ring-cusp ion thrusters.* Doctor of philosophy, California Institute of Technology, 2005.

[22] D. A. Herman, *The use of electrostatic probes to characterize the discharge plasma structure and identify discharge cathode erosion mechanisms in ring-cusp ion thrusters.* Doctor of philosophy, The University of Michigan, 2005.

[23] A. Sengupta, D. M. Goebel, and A. G. Owens, “Langmuir Probe Studies of Magnetic Confinement in an Ion Thruster Discharge Plasma,” *J. Propul. Power*, vol. 25, pp. 387–396, Mar. 2009.

[24] R. Wirz and I. Katz, “Plasma Processes of DC Ion Thruster Discharge Chambers,” in *41st AIAA Joint Propulsion Conference*, (Tuscon, AZ), AIAA Paper 2005-3690, July 2005.

[25] F. F. Chen, *Introduction to plasma physics and controlled fusion. Volume 1, Plasma physics.* Springer, 1984.

[26] R. Limpaecher and K. MacKenzie, "Magnetic multipole containment of large uniform collisionless quiescent plasmas," *Rev. Sci. Instrum.*, vol. 44, no. 6, pp. 726–731, 1973.

[27] R. Bosch and R. Merlino, "Confinement properties of a low-beta discharge in a spindle cusp magnetic field," *Phys. Fluids*, vol. 29, pp. 1998–2006, 1986.

[28] R. Wirz, S. Araki, and B. Dankongkakul, "Near-Surface Cusp Confinement for Weakly Ionized Plasma," in *48th AIAA Joint Propulsion Conference*, Joint Propulsion Conferences, (Atlant, GA), AIAA Paper 2012-3948, July 2012.

[29] D. M. Goebel, "Ion source discharge performance and stability," *Phys. Fluids*, vol. 25, no. 6, pp. 1093–1102, 1982.

[30] J. P. Sheehan and N. Hershkowitz, "Negative plasma potential in a multidipole chamber with a dielectric coated plasma boundary," *J. Vac. Sci. Technol. A*, vol. 30, no. 3, p. 031302, 2012.

[31] L. Oksuz and N. Hershkowitz, "Negative plasma potential in unmagnetized DC electropositive plasma with conducting walls," *Phys. Lett. A*, vol. 375, pp. 2162–2165, May 2011.

[32] R. Franklin, "The plasma sheath boundary region," *J. Phys. D*, vol. 309, 2003.

[33] G. Medicus, "Theory of electron collection of spherical probes," *J. Appl. Phys.*, vol. 32, no. 12, pp. 2512–2520, 1961.

[34] J. Brophy, "Simulated ion thruster operation without beam extraction," in *21st International Electric Propulsion Conference*, (Orlando, FL), AIAA Paper 1990-2655, 1990.

[35] J. Foster and M. Patterson, "Enhanced Discharge Performance in a Ring Cusp Plasma Source," in *26th International Electric Propulsion Conference*, IEPC-99-159, 1999.

[36] D. M. Goebel, J. E. Polk, and I. G. Mikellides, "Ion Thruster Performance Impacts due to Cathode Wear," *J. Propul. Power*, vol. 27, pp. 768–776, July 2011.

[37] S. Babic and C. Akyel, “Improvement in the analytical calculation of the magnetic field produced by permanent magnet rings,” *Prog. Electromagn. Res.*, vol. 5, pp. 71–82, 2008.

[38] R. Ravaud, G. Lemarquand, V. Lemarquand, and C. Depollier, “Analytical Calculation of the Magnetic Field Created by Permanent-Magnet Rings,” *IEEE T. Magn.*, vol. 44, pp. 1982–1989, Aug. 2008.

[39] J. Happel and H. Brenner, *Low Reynolds Number Hydrodynamics: with special applications to particulate media (Mechanics of Fluids and Transport Processes)*. Springer, 1983.

[40] A. T. Forrester, D. M. Goebel, and J. T. Crow, “IBIS: A hollow-cathode multipole boundary ion source,” *Appl. Phys. Lett.*, vol. 33, no. 1, p. 11, 1978.

[41] R. Wirz, R. Sullivan, J. Przybylowski, and M. Silva, “Hollow Cathode and Low-Thrust Extraction Grid Analysis for a Miniature Ion Thruster,” in *Int. J. Plasma Sci. Eng.*, vol. 2008, Article ID 699825, 2008.

[42] J. R. Beattie and J. N. Matossian, “Inert-gas ion thruster technology,” *NASA CR191093, March*, 1993.

[43] R. Wirz and D. Goebel, “Effects of magnetic field topography on ion thruster discharge performance,” *Plasma Sources Sci. T.*, vol. 17, Aug. 2008.

[44] R. L. Panton, *Incompressible Flow*. Wiley, 2005.

[45] R. D. Hazeltine and F. L. Waelbroeck, *The Framework Of Plasma Physics (Frontiers in Physics)*. Westview Press, 2004.

[46] C. Koch and G. Matthieussent, “Collisional diffusion of a plasma in multipolar and picket fence devices,” in *Phys. Fluids*, vol. 26, p. 545, 1983.

[47] W. D. D’haeseleer, W. N. G. Hitchon, J. D. Callen, and J. L. Shohet, *Flux Coordinates and Magnetic Field Structure: A Guide to a Fundamental Tool of Plasma Theory (Scientific Computation)*. Springer, 2012.

[48] K. Riley, M. Hobson, and S. Bence, *Mathematical methods in physics and engineering*. 1988.

[49] R. Comfort, “The magnetic mirror force in plasma fluid models,” *Modeling magnetospheric plasma*, pp. 51–53, 1988.

[50] R. Engel-Herbert and T. Hesjedal, “Calculation of the magnetic stray field of a uniaxial magnetic domain,” *J. Appl. Phys.*, vol. 97, no. 7, p. 074504, 2005.

[51] A. Forrester, “Magnetic Fields for Surface Containment of Plasmas,” *J. Appl. Phys.*, vol. 47, no. No. 6, pp. 3935–3941, 1975.

[52] D. E. Gray, *American Institute of Physics handbook*. McGraw-Hill handbooks, McGraw-Hill, 1957.

[53] Dexter Magnet Technologies, “Reference & Design Manual,” 2001.

[54] G. Farnebäck, J. Rydell, T. Ebbers, M. Andersson, H. Knutsson, G. Farneb, M. Informatics, and B. Engineering, “Efficient Computation of the Inverse Gradient on Irregular Domains,” Dec. 2009.

[55] W. H. Press, S. A. Teukolsky, W. T. Vetterling, and B. P. Flannery, *Numerical Recipes 3rd Edition: The Art of Scientific Computing*. Cambridge University Press, 2007.

[56] M. Martinez-Sánchez and E. Ahedo, “Magnetic mirror effects on a collisionless plasma in a convergent geometry,” *Phys. Plasmas*, vol. 18, p. 033509, 2011.

[57] D. Rapp and P. Englander-Golden, “Total cross sections for ionization and attachment in gases by electron impact. I. Positive ionization,” *J. Chem. Phys.*, vol. 43, pp. 1464–1479, 1965.

[58] M. Hayashi, “Determination of electron-xenon total excitation cross-sections, from threshold to 100 eV, from experimental values of Townsend’s α,” *J. Phys. D*, vol. 16, pp. 581–589, Apr. 1983.

[59] L. Spitzer, *Physics of Fully Ionized Gases*. John Wiley & Sons Inc, 1962.

[60] J. N. Matossian, “Characteristics of ring-cusp discharge chambers,” *J. Propul. Power*, vol. 7, pp. 968–974, Nov. 1991.

[61] A. Lang and N. Hershkowitz, “Multidipole plasma density,” *J. Appl. Phys.*, vol. 49, pp. 4707–4710, 1978.

[62] R. McEachran and A. Stauffer, “Elastic scattering of electrons from krypton and xenon,” *J. Phys. B*, vol. 17, pp. 2507–2518, 1984.

[63] I. Boyd, “Numerical modeling of spacecraft electric propulsion thrusters,” *Prog. Aerosp. Sci.*, vol. 41, pp. 669–687, Nov. 2005.

[64] S. Mahalingam and J. A. Menart, “Particle-Based Plasma Simulations for an Ion Engine Discharge Chamber,” *J. Propul. Power*, vol. 26, pp. 673–688, July 2010.

[65] Y. Arakawa and K. Ishihara, “A numerical code for cusped ion thrusters,” in *22nd International Electric Propulsion Conference*, (Viareggio, Italy), IEPC-91-118, 1991.

[66] M. Hirakawa and Y. Arakawa, “Plasma Particle Simulation in Cusped Ion Thrusters,” in *23rd International Electric Propulsion Conference*, (Seattle, WA), IEPC-93-242, 1993.

[67] H. Takekida and K. Nanbu, “Particle modelling of plasma confinement by a multipolar magnetic field,” *J. Phys. D*, vol. 37, pp. 1800–1808, July 2004.

[68] H.-S. Mao and R. E. Wirz, “Plasma Structure of Miniature Ring-Cusp Ion Thruster Discharges,” in *48th AIAA Joint Propulsion Conference*, (Atlanta, GA), AIAA Paper 2012-4021, July 2012.

[69] Z. Lin, J. W. Bieber, and P. Evenson, “Electron trajectories in a model magnetosphere: Simulation and observation under active conditions,” *J. Geophys. Res.*, vol. 100, no. A12, pp. 23543–23549, 1995.

[70] F. Mackay, R. Marchand, and K. Kabin, “Divergence-free magnetic field interpolation and charged particle trajectory integration,” *J. Geophys. Res.*, vol. 111, pp. 1–8, June 2006.

[71] A. Bergmann, “Two-dimensional particle simulation of Langmuir probe sheaths with oblique magnetic field,” *Phys. Plasmas*, vol. 1, no. 11, pp. 3598–3606, 1994.

[72] D. Tskhakaya, S. Kuhn, V. Petrzilka, R. Khanal, and V. Petrzilka, “Effects of energetic electrons on magnetized electrostatic plasma sheaths,” *Phys. Plasmas*, vol. 9, no. 6, p. 2486, 2002.

[73] T. Daube, K.-U. K. Riemann, and H. Schmitz, “Particle simulation of a magnetized plasma contacting the wall,” *Phys. Plasmas*, vol. 5, no. 1, pp. 117–126, 1998.

[74] T. Daube and K.-U. Riemann, “Kinetic analysis of the plasma boundary layer in an oblique magnetic field,” *Phys. Plasmas*, vol. 6, no. 6, pp. 2409–2417, 1999.

[75] S. Ido, K. Nakamura, M. Takahashi, and M. Kashiwagi, "Computational Studies of Plasma Generation and Control in a Magnetron Sputtering System," in *Jpn. J. Appl. Phys.*, vol. 38, pp. 2302–2305, The Japan Society of Applied Physics, Oct. 1996.

[76] J. P. Boris, "Relativistic Plasma Simulation - Optimization of a Hybrid Code," in *4th Conference on the Numerical Simulation of Plasma*, (Washington, DC), pp. 3–67, Naval Research Laboratory, 1970.

[77] C. K. Birdsall and A. B. Langdon, *Plasma Physics via Computer Simulation (Series in Plasma Physics).* Taylor & Francis, 2004.

[78] R. Wirz and I. Katz, "2-D Discharge Chamber Model for Ion Thrusters," in *40th AIAA Joint Propulsion Conference*, (Fort Lauderdale, FL), AIAA Paper 2004-4107, July 2004.

[79] E. Hairer, C. Lubich, and M. Roche, *The Numerical Solution of Differential-Algebraic Systems by Runge-Kutta Methods (Lecture Notes in Mathematics).* Springer, 1989.

[80] H. Yugo and T. Iyemori, "Symplectic integration: A new approach to tracing charged particle motion in the geomagnetic field," *J. Geophys. Res.*, vol. 106, no. A11, pp. 26075–26079, 2001.

[81] J. M. Sanz-Serna and M. P. Calvo, *Numerical Hamiltonian Problems (Applied Mathematics).* Chapman and Hall/CRC, 1994.

[82] J. M. Sanz-Serna, "Runge-kutta schemes for Hamiltonian systems," *BIT*, vol. 28, pp. 877–883, Dec. 1988.